Title

Longitudinal Field of Radially Polarized Microwaves in Focal Region of Parabolic Reflector and some Applications (vacuum acceleration and quasi Bessel beam)

Permalink

https://escholarship.org/uc/item/1bg5674j

Author

Kang, Bong Soo

Publication Date

2016

Peer reviewed|Thesis/dissertation

UNIVERSITY OF CALIFORNIA, MERCED

Longitudinal Field of Radially Polarized Microwaves in Focal Region of Parabolic Reflector and some Applications (vacuum acceleration and quasi Bessel beam)

A dissertation submitted in partial fulfillment of the requirements
for the degree Doctor of Philosophy

in

Physics

by

Bong Soo Kang

Committee in charge:

Professor Roland Winston, Chair

Professor Arnold Kim

Professor Kevin Mitchel

Professor Michael Scheibner

Professor Raymond Chiao, Dissertation Adviser

2016

The Dissertation of Bong Soo Kang is approved, and it is acceptable
in quality and form for publication on microfilm and electronically:

_____

Roland Winston, Chair   Date

_____

Arnold Kim   Date

_____

Kevin Mitchel   Date

_____

Michael Scheibner   Date

_____

Raymond Chiao, Dissertation Adviser   Date

University of California, Merced

2016

This dissertation is dedicated to my wife, Sang Soon, for all of her love and support

Contents

List of Figures

List of Tables

Acknowledgements

Foremost, I would like to express my deepest gratitude to my advisor, Professor Raymond Chiao and his wife Florence Chiao for their love and encouragement. I am forever indebted to him for his enormous help and advice which cannot be expressed with words.

I would like to express my sincere gratitude to committee members Professor Roland Winston, Professor Kevin Mitchell, Professor Michael Scheibner and Professor Arnold Kim for their kind understanding, encouragement and continuous support. I am especially grateful to Professor Roland Winston for his helpful comments and constructive guidance that significantly improved this dissertation.

I wish to thank other Physics faculty members at the University of California, Merced, especially Professor Lin Tian and Professor Linda Hirst for their kind teaching and encouragement.

I also would like to express my appreciation to Professor Steve Kang for his valuable advice and encouragement.

I thank my fellow student researchers, especially Luis Martinez, for his help in the lab. I also thank Jane Hyo Jin Lee for her great help in using softwares.

Finally and most importantly, I want to thank my family : my beloved wife, an everlasting true partner and friend of life from almost half-a-century long marriage, Sang Soon, for her support, patience and unwavering love, and daughter, Yoon Na, and son, Young Jae, for their continuous support and encouragement.

Vita

<div align="center">

Education

</div>

Doctor of Philosophy in Physics   Expected 2016
University of California, Merced
Field of Study: microwave optics, particle accelerator
Advisor: Professor Raymond Chiao

Master of Law   1968
Seoul National University, Korea (South)
Field of Study: Company under Establishment
Advisor: Professor Hee Chul Chung

Bachelor of Law   1965
Seoul National University, Korea (South)
Field of Study: Commercial Law

<div align="center">

Teaching Experience

</div>

Teaching Assistant, University of California, Merced   2014
Field of Teaching: Physics

<div align="center">

Publication

</div>

R.Y. Chiao, R. Haun, N.Inan, B.S. Kang, L.A. Martinez, S.J. Minter, G. Munoz, and D. Singleton, A gravitational Aharonov-Bohm Effect, and its connection to parametric oscillators and gravitational radiation,Quantum Theory: A Two-Time Success Story (Yakir Aharonov Festschrift), p. 213,   2014

Longitudinal Field of Radially Polarized Microwaves in Focal Region of Parabolic Reflector and some Applications (vacuum acceleration and quasi Bessel beam)

by

Bong Soo Kang

Doctor of Philosophy in Physics

University of California, Merced, 2016

Chair: Professor Roland Winston

Abstract

The longitudinal component of radially polarized electric field in the focal region has attracted particular attention in the laser optics due to its several special characteristics, namely, the directional characteristic on propagation axis, strong intensity and small focal size when tightly focused with high-numerical-aperture optical system, which find applications such as particle acceleration, molecule microscopy, material processing, and particle trapping. It has been proposed and experimentally demonstrated that paraboloidal reflector creates smaller focal size compared with lens.

Comparatively little attention has been paid to its microwave version since, in microwave regime, the directional property in focal region has not been the main interest. Only very recently, after the introduction of planar slot antenna which can generate microwaves with focusing for near field scanning, the longitudinal component of radially polarized microwave with the slot antenna has been experimentally investigated. However, the focusing of radially polarized microwave with paraboloidal reflector is much more versatile in applications as in the optical regime.

The experimental observation of this longitudinal component is newly performed in this work with a configuration of two-paraboloidal-mirror system. This longitudinal field of microwave and the two-mirror system can also be exploited in some applications such as microwave scanning, microwave acceleration in free space, and creating Bessel-like beam which can be used in high resolution tomography, micro-manipulation in optical regime and long range communication in microwave regime. Two applications, microwave particle acceleration and quasi Bessel beam, are investigated in this work.

A new method of ultratight focusing acceleration is proposed and a more precise analysis of quasi Bessel beam with variable cone angles is demonstrated.

Part I

Longitudinal field of radially polarized microwave in focal region of parabolic reflector

Chapter 1

Introduction

1) In optical regime, the properties of the radially polarized beam in focal region have attracted attentions for a long time. When the radially polarized beam is focused, the longitudinal electric fields arise in the focal area due to the vector nature of the focused beam. It is quite different from the linearly polarized beam case where there is no longitudinal components in the focal area.

These longitudinal components contribute to reduce the focal spot size [1]. These two properties i.e., longitudinal components near focal area and the small focal size of the radially polarized beams can be used for various applications, e.g., electron acceleration[2] [3], molecule microscopy[4], high density optical data storage [5], material processing[6], and particle trapping[7]

2) In microwave range, focusing is also desired for many applications such as wireless power transmission, remote sensing and medical therapy of microwave hyperthermia by heating. In general, the usual conventional methods to get focusing are dielectric lenses, parabolic reflectors, phased-arrays antennas in waveguide or microstrip. However, polarization of the waves and the directional components in the focal region have not been regarded as important since the main interest has been mostly in the energy concentration and transfer. With the recently introduced leaky-wave lens antenna[8], the radial polarization of microwave and the longitudinal component in the focal region attracted attention and several observations using annularly slotted leaky-wave lens antennas have been reported [9], [10], [11].

3) Brief history of studies on longitudinal components

We review briefly the studies on longitudinal field in chronological order. The first experiments on the intensity and the phase of focused microwaves were carried out in 1956-1958 [12, 13, 14, 15] and the first measurement of the longitudinal and transverse electric fields in focal area was done with linearly polarized microwaves using a double convex polystyrene lens in 1961[16]. The strong transverse component and zero longitudinal component in the focal area on propagation axis were observed, and the strong longitudinal component in certain regions in the neighborhood of the focus was also observed.

After the advent of laser, it was suggested that the longitudinal field in the focal region of the radially polarized laser beam may be used for particle acceleration[17].

Later it was shown theoretically [1] and experimentally [18] that the smaller spot size and a

strong longitudinal component are achieved by focusing an annular shaped radially polarized light beam with a high aperture lens. It was also demonstrated theoretically [4][19] and experimentally [20] that by using parabolic reflector instead of lens the smaller spot sizes, and strong and well localized longitudinal components of electric field can be produced, which might be applied in near-field scanning and optical microscopy.

Recently it is experimentally shown that the longitudinal field of a radially polarized terahertz beam has a smaller spot size as compared with the transverse field of a linearly polarized beam that is focused under the same conditions [21].

As for the microwave regime, the interest in the fields in the focal region has recently arisen for microwave imaging, sensing, and heating. The measurements of the longitudinal and the transverse components have been reported in 2012 and 2014 showing longitudinal component for radially polarized microwave[11], [9], [10]. However, They are the results of measurements using planar-slot antennas, not parabolic reflector. To the best of my knowledge, there have been no reports on the measurement of longitudinal component of radially polarized microwave in the focal region of parabolic mirror comparable to the optical counterpart in the literature.

4) Goal of this research

The objectives of this work are the measurement of longitudinal component of radially polarized microwave in the focal region of parabolic mirror of high NA and investigation on its applications to particle acceleration and generation of quasi Bessel beam.

4) Contents

Chapter two contains the theoretical investigation on the field in focal region. Most of the researches done in this direction are about the optical regime (laser beam). Since light and microwaves are all electromagnetic waves and their difference resides only in the different frequency ranges, there are no fundamental differences in theoretical description between them. Therefore, all the theoretical considerations for the laser beam near the focal region will be applied here. In chapter three, the experimental observations of longitudinal components are reported. Chapters thereafter describe the applications. Chapter four shows the vacuum particle acceleration through longitudinal field of microwaves and parabolic mirror system. A new method of ultratight focusing acceleration with parabolic mirror system is proposed. Chapter five contains the new analysis on quasi Bessel beam with the same experimental set-up adopted in this work.

Chapter 2

Theoretical description

2.1 Introduction

The focusing can be realized with waves illuminated in the form of a beam. Accordingly, all the theoretical descriptions of the fields in focal region start with the analysis of this propagating beam which has a paraxial shape. There are three main methods to describe the fields in the focal region mathematically. 1) The integral representation method which was introduced by Richards and Wolf[22] is based on the angular spectrum representation of plane wave in the diffraction theory. This method is applied in the image optics by Quabis et al. [1], Youngworth and Brown [23], [4]and Kozawa and Sato [24] . 2) The other one is the vector potential approach which was introduced by Lax, Louisell and McKnight.[25] and simplified by Davis[26] based on non-paraxial correction of the paraxial solution. It has been adopted by Agrawal and Pattanayak [27], Salamin [28], Varin, Piche and Porras. [29]. 3) The third one is the complex source-point model where a wave source is assumed to be located at an imaginary distance along the propagation axis. It was introduced by Deschamps[30] and applied to non-paraxial beam by Couture and Belanger [31], April [32].

The first one has a merit in its vector treatment and geometrical easiness to handle, but also a demerit because the integrals have to be solved numerically. The second one has a merit in its complete compliance with Maxwell's equations, but has a demerit due to its infinite series which has to be analytically truncated to some degree of accuracy[32]. The third one has a merit in its closed form, but a demerit due to its scalar treatment. The first one (method of angular spectrum representation) is convenient for the optical investigation of focal region due to its appropriateness to the geometric structure of the optical system, while the second and the third approaches are suitable when the beam is used for the particle acceleration in the paraxial limit.

In this work, we apply the first method since the primary goal is the observation of fields in focal region.

Theories on fields in focal region has been developed with wave optics. In wave optics, focusing is one of the diffraction phenomena of electromagnetic waves. Sommerfeld defined the term diffraction as "any deviation of light rays from rectilinear paths which cannot be interpreted as reflection or refraction."[33, p179]

Diffraction in the sense of the deviation from rectlinear propagation (ray optics) was first discovered by Grimaldi and theoretical development based on wave theory was done by Huygens in seventeenth century.

2.2 Spherical wave representation

According to Huygens' principle, every point on a wavefront gives rise to a secondary spherical wavelets and the wavefront at any later instant is the envelope of these secondary wavelets. Later in nineteenth century Fresnel supplemented Huygens' construction with mutual interference of secondary wavelets based on Young's interference theory. This is called Huygens-Fresnel principle. Early works on imaging in focal plane were done by Airy, Lommel, Struve and Schwartzschild in 19th century. All these works were based on Huygens-Fresnel principle, i.e., spherical wave representations of the focused field [34].

According to the Huygens-Fresnel principle, the light disturbance at observation point P is the superposition (integration) of the combination of first and secondary wavelets as follows [35];

$$U(P) = \frac{Ae^{ikr_0}}{r_0} \int \int_S \frac{e^{iks}}{s} K(\varphi) dS \qquad (2.1)$$

where r_0 is radius of first wavefront, s is the distance from a certain point of disturbance on the first wavefront to point P, A is the amplitude at unit distance from the source, $K(\varphi)$ is an inclination (obliquity) factor which describes the variation with direction of the amplitude of the secondary waves, and φ is a diffraction angle between normal at first wavelet and the direction to P, all as shown in Fig. 2.1.
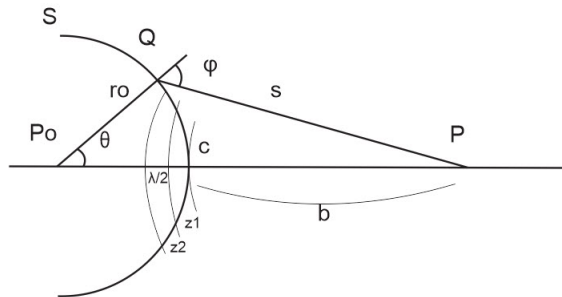
Figure 2.1: Huygens-Fresnel principle

2.3 Angular spectrum representation

2.3.1 Debye integral (superposition of plane waves)

Debye [36] introduced an integral formula using the approximation about the distances of sources which results in the superposition of the plane waves[35, pp. 485]. Debye integral expresses the field in the focal region as a superposition of plane waves of different directions of propagation inside the cone formed by the focal point and the edge of the aperture (Debye approximation).
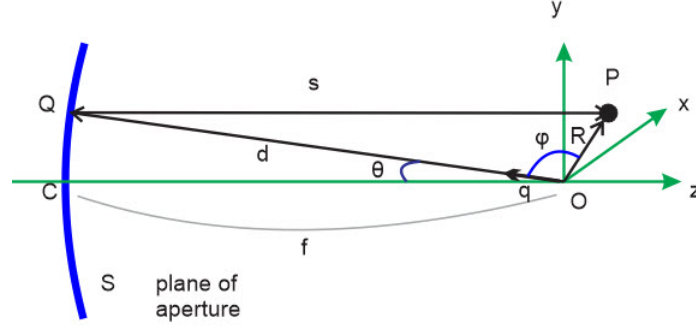
Figure 2.2: Debye approximation

Referring to Fig.2.2, we assume the angle θ is very small and hence we can rewrite Equation (2.1) neglecting obliquity factor as follows,

$$
\begin{aligned}
U(P) &= -\frac{i}{\lambda}\frac{Ae^{-ikf}}{f}\int\int_S \frac{e^{iks}}{s}dS \\
&= -\frac{i}{\lambda}\int\int_S \frac{Ae^{-ikf}}{f}\frac{e^{iks}}{s}dS \\
&= -\frac{i}{\lambda}\int\int_S \frac{Ae^{ik(s-f)}}{sf}dS
\end{aligned}
\tag{2.2}
$$

To find the value of $s-f$ in Equation (2.2), we apply the cosine rule with approximation $R << d$ and $d \sim f$,

$$
\begin{aligned}
s &= (d^2 + R^2 - 2dR\cos(\varphi))^{1/2} \\
&= d(1 + \frac{R^2}{d^2} - \frac{2R}{d}\cos(\varphi))^{1/2} \\
&\sim d(1 + \frac{1}{2}\frac{R^2}{d^2} - \frac{1}{2}\frac{2R}{d}\cos(\varphi)) \\
&\sim d(1 - \frac{R}{d}\cos(\varphi)) \\
&= d - R\cos(\varphi)
\end{aligned}
\tag{2.3}
$$

or

$$
s - f = -R\cos(\varphi) = -\mathbf{q}\cdot\mathbf{R}
\tag{2.4}
$$

By substituting Equation (2.4) to the numerator, the approximation $d \sim f$ to the denominator and the solid angle expression $f^2 d\Omega$ to the element dS of Equation (2.2), we get,

$$
U(p) = -\frac{i}{\lambda}A\int\int_\Omega e^{-ik\mathbf{q}\cdot\mathbf{R}}d\Omega
\tag{2.5}
$$

where $\mathbf{q}$ is a unit vector of d and $\mathbf{R}$ is the vector expression of R. This is the Debye integral which expresses the field as a superposition of plane waves of different directions of propagation.

2.3.2 Angular spectrum representation

Born and Wolf generalized it using angular spectrum method in the form [37, p.639],

$$\int f(\alpha) \exp(ik \cdot r) d\alpha \tag{2.6}$$

where $exp(ik \cdot r)$ is the kernel of the integral denoting plane wave and $f(\alpha)$ is spectrum of directional spatial angle of wave vector k which might be closely linked with arbitrary function by means of Fourier integral and hence the whole expression is the angular spectrum of plane wave. In this case, the superposition of plane waves is expressed in Fourier transform which is called angular spectrum representation.

For a monochromatic plane wave traveling in the arbitrary direction k which is expressed as $A \exp(ik \cdot r - i\omega t)$, time-independent part $F(r) \equiv F(x, y, z)$ may be represented in the Fourier integral representation with respect to the variables x and y,

$$F(r) = \iint\limits_{-\infty}^{\infty} f(k_x, k_y, z) \exp[i(k_x x + k_y y)] dk_x dk_y \tag{2.7}$$

The angular representation part is the Fourier transform.

$$f(k_x, k_y, z) = \iint\limits_{-\infty}^{\infty} F(x, y, z) \exp[-i(k_x x + k_y y)] dx dy \tag{2.8}$$

The angular representation also satisfies the Helmholtz equation and can be solved.
The merit of using Fourier integral expression is that we can solve the wave propagation problem exploiting this relation.
Assume that we know the incident field $F(x, y, 0)$ on the plane transverse to the propagation z-direction at $z = 0$, and our goal is to find the field $F(x, y, z)$ on the plane at location z.
First we construct angular spectrum with respect to x and y as in Equation (2.8). Then assuming that f satisfies the Helmholtz equation as F does, we find the solution,

$$\frac{d^2}{dz^2} f(k_x, k_y, z) + k_z^2 f(k_x, k_y, z) = 0 \tag{2.9}$$

$$f(k_x, k_y, z) = f(k_x, k_y, 0) \exp(ik_z z) \tag{2.10}$$

Then we get

$$F(x, y, z) = \iint\limits_{-\infty}^{\infty} f(k_x, k_y, z) \exp[i(k_x x + k_y y)] dk_x dk_y$$
$$= \iint\limits_{-\infty}^{\infty} f(k_x, k_y, 0) \exp(ik_z z) \exp[i(k_x x + k_y y)] dk_x dk_y \tag{2.11}$$

To make the angular spectrum part physically more distinct, the concepts of spatial frequency and direction cosines may be introduced. We assume that the $\vec{k}$ vector of a plane wave has magnitude $2\pi/\lambda$ and direction cosines (α, β, γ).

$$\vec{k} = \frac{2\pi}{\lambda}(\alpha\hat{x} + \beta\hat{y} + \gamma\hat{z}) \tag{2.12}$$

Such a plane wave has a complex representation of the form,

$$p(x, y, z) = \exp(i\vec{k} \cdot \vec{r}) = \exp(i\frac{2\pi}{\lambda}(\alpha x + \beta y + \gamma z)) \tag{2.13}$$

where $\vec{r} = x\hat{x} + y\hat{y} + z\hat{z}$.

The relation between direction cosines is $\alpha^2 + \beta^2 + \gamma^2 = 1$. We define spatial frequency as $f_x = \alpha/\lambda$, $f_y = \beta/\lambda$ and $f_z = \gamma/\lambda$. Then the angular spectrum at $z = 0$ becomes,

$$f(f_x, f_y, 0) = \iint\limits_{-\infty}^{\infty} F(x, y, 0) exp[i2\pi(f_x x + f_y y)] \, dx \, dy \tag{2.14}$$

In 1959, Wolf [38] derived the time independent component of wave in the form

$$e(P) = -\frac{ik}{2\pi} \int\int_{\Omega} A(s)e^{ik\mathbf{s}\cdot\mathbf{r}}d\Omega \tag{2.15}$$

where $A(s)$ is angular spectrum.

2.4 Angular spectrum representation in focal region

2.4.1 focal region of lens

Richards and Wolf analyzed linearly polarized beams in focal area of objective lens using angular spectrum method [22, Appendix]

Leutenegger et al. introduced the method of fast calculation of focal field of objective lens using Debye diffraction integral [39]. Youngworth and Brown described [1] the electric fields of radially polarized beam together with azimuthal polarized beam near focal region of aplanatic lens [23].

They started with Equation (2.15) and tried to find the field amplitude factor A and scalar product $\mathbf{s} \cdot \mathbf{r}$ as follows (we adopted similar diagram and notations).

The electric field at point P near focus in focal region is,

$$e(P) = -\frac{ik}{2\pi} \int\int_{\Omega} A_1 e^{ik\mathbf{s}\cdot\mathbf{r}}d\Omega \tag{2.16}$$

which has been rewritten from Equation (2.15) with different subscript for convenience.

As is shown in Fig.2.3, the collimated, incident field is assumed to have a planar phase front at plane 0 (entrance pupil) and is converged as a spherical wave at focal sphere

---

[1]The different derivation based on Complex Source Point method was done by A. April [40]

by aplanatic lens. The unit vector $\mathbf{g}_0$ oriented perpendicular to the optical axis may be expressed by Cartesian components in cylindrical coordinates;

$$\mathbf{g}_0 = cos\phi\hat{\mathbf{i}} + sin\phi\hat{\mathbf{j}} \tag{2.17}$$

where ϕ denotes the azimuthal angle with respect to the x-axis.
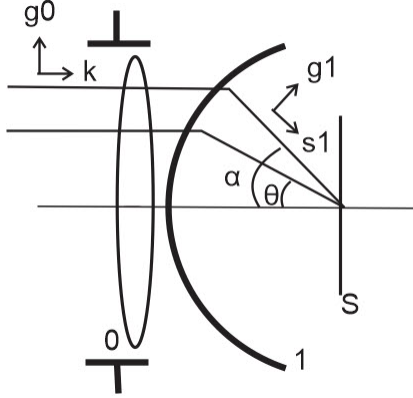
Figure 2.3: geometry of focusing

The electric field in region 0 may be expressed with its radial and azimuthal components;

$$\mathbf{e}_0 = I_0[e_r^{(0)}\mathbf{g}_0 + e_\phi^{(0)}(\mathbf{g}_0 \times \hat{\mathbf{k}})] \tag{2.18}$$

where I_0 denotes the relative amplitude of the field, which is assumed to vary radially but keeps cylindrical symmetry.

From Fig. 2.3, we can see that the vector field amplitude in image field A_1 may be related to the object space electric field $I_0(\theta)$ through apodization factor $cos^{1/2}(\theta)$ as follows,

$$A_1 = f_1 cos^{1/2}(\theta)I_0(\theta)[e_r^0\mathbf{g}_1 + e_\phi^0(\mathbf{g}_1 \times \mathbf{s}_1)] \tag{2.19}$$

where $\mathbf{g}_1$ is radial unit vector after refraction perpendicular to $\hat{\mathbf{s}}_1$, the direction of ray propagation.

Using polar angle θ, we can express $\mathbf{g}_1$ as,

$$\mathbf{g}_1 = cos\theta(cos\phi\hat{\mathbf{i}} + sin\phi\hat{\mathbf{j}}) + sin\theta\hat{\mathbf{k}} \tag{2.20}$$

As for the scalar product in equation (2.15), the spatial vector in image space can be expressed in cylindrical coordinates as $\mathbf{r} = (\rho_s, \phi_s, z_s)$, while the unit vector of ray propagation in image space $\hat{\mathbf{s}}_1 = (sin\theta, \phi_s, cos\theta)$.

Accordingly, the dot product part is,

$$
\begin{aligned}
\hat{\mathbf{s}}_1 \cdot \mathbf{r} &= (\sin\theta, \phi_s, \cos\theta) \cdot (\rho_p, \phi_p, z_p) \\
&= \sin\theta\rho_p + \phi_s\phi_p + z_p\cos\theta \\
&= \sin\theta\rho_p + \rho_s\phi_s\rho_p\phi_p\cos(\phi_s - \phi_p) + \cos\theta z_s \\
&= z_p\cos\theta + \rho_p\sin\theta\cos(\phi_s - \phi_p)
\end{aligned}
\tag{2.21}
$$

where all parameters with subscription p are parameters of observation point P.
For radially polarized illumination, azimuthal component e_ϕ^0 is zero in Equation (2.18),(2.19)
Putting all the things into Equation (2.16), we get,

$$
\begin{aligned}
e(P) &= -\frac{ik}{2\pi}\int\int_\Omega A_1 e^{ik\mathbf{s}\cdot\mathbf{r}}d\Omega \\
&= -\frac{ik}{2\pi}\int\int_\Omega f_1\cos^{1/2}(\theta)I_0(\theta)e_r^0(z_p\cos\theta + \rho_p sin\theta\cos(\phi_s - \phi_p))d\Omega
\end{aligned}
\tag{2.22}
$$

We can rewrite in Cartesian components as follows,

$$
\mathbf{e}^p = \begin{bmatrix} e_x^p \\ e_y^p \\ e_z^p \end{bmatrix} = \frac{-iA}{\pi}\int_0^\alpha\int_0^{2\pi}\sin\theta\cos^{1/2}\theta I_0(\theta)exp(ik(z_p\cos\theta + \rho_p\sin\theta\cos(\phi - \phi_p)))\begin{bmatrix} \cos\theta\cos\phi \\ \cos\theta\sin\phi \\ \sin\theta \end{bmatrix}d\phi d\theta
\tag{2.23}
$$

From Equation (2.23), it is clear that the longitudinal component along propagating z-axis is;

$$
e_z^p = \frac{-iA}{\pi}\int_0^\alpha\int_0^{2\pi}\sin^2\theta\cos^{1/2}\theta I_0(\theta)exp(ik(z_p\cos\theta + \rho_p\sin\theta\cos(\phi - \phi_p))d\phi d\theta
\tag{2.24}
$$

To construct the azimuthal and radial components, we use the Cartesian-to-cylindrical-coordinate transformations;

$$
\begin{aligned}
e_\phi^p &= e_y^p\cos\phi_p - e_x^p\sin\phi_p \\
e_\rho^p &= e_x^p\cos\phi_p + e_y^p\sin\phi_p
\end{aligned}
\tag{2.25}
\tag{2.26}
$$

For radially polarized waves, the azimuthal component is zero everywhere in image space. We get the radial component by putting (2.23) into (2.26);

$$
e_\rho^p = \frac{-iA}{\pi} \int_0^\alpha \int_0^{2\pi} \sin\theta \cos^{1/2}\theta I_0(\theta) \exp(ik(z_p\cos\theta + \rho_p\sin\theta\cos(\phi-\phi_p)))
$$
$$
\times (\cos\theta\cos\phi\cos\phi_p - \cos\theta\sin\phi\sin\phi_p)d\phi d\theta
$$
$$
= \frac{-iA}{\pi} \int_0^\alpha \int_0^{2\pi} \sin\theta \cos^{1/2}\theta I_0(\theta) \exp(ik(z_p\cos\theta + \rho_p\sin\theta\cos(\phi-\phi_p)))
$$
$$
\times \cos\theta(\cos\phi\cos\phi_p - \sin\phi\sin\phi_p)d\phi d\theta
$$
$$
= \frac{-iA}{\pi} \int_0^\alpha \int_0^{2\pi} \sin\theta \cos^{1/2}\theta I_0(\theta) exp(ik(z_p\cos\theta + \rho_p\sin\theta\cos(\phi-\phi_p)))
$$
$$
\times \cos\theta\cos(\phi-\phi_p)d\phi d\theta \quad (2.27)
$$

By using Bessel identity;

$$
\int_0^{2\pi} \cos(n\phi)exp(ik\rho_p\sin\theta\cos\phi)d\phi = 2\pi i^n J_n(\rho_p\sin\theta) \quad (2.28)
$$

where $J_n(\rho_p\sin\theta)$ denotes a Bessel function of the first kind of order n, we get;

$$
e_z^p = 2iA \int_0^\alpha \sin^2\theta \cos^{1/2}\theta I_0(\theta) J_0(k\rho_p\sin\theta) exp(ikz_p\cos\theta)d\theta \quad (2.29)
$$

$$
e_\rho^p = A \int_0^\alpha \sin(2\theta) \cos^{1/2}\theta I_0(\theta) J_1(k\rho_p\sin\theta) exp(ikz_p\cos\theta)d\theta \quad (2.30)
$$

2.4.2 Focal region of parabolic mirror

The early work on the focusing of parabolic mirrors was published by Ignatovsky in 1920. The focusing of a parabolic mirror has been extensively studied in microwaves mostly with a partially truncated mirror[41],[42]. and later with arbitrary openings [43],[44]. The work of numerical calculations for fields in the focal area has also been done [45],[46],[47].

However, all investigations concerned the linearly polarized waves. The complete derivation for radially polarized beam focused by parabolic mirror has been done by Lieb and Meixner [4].

We follow Lieb and Meixner in deriving the fields in focal area of parabolic mirror. There are three main differences between objective lens and parabolic mirror for radially polarized beams i.e., apodization factor, phase jump and direction change of propagation.

1) apodization

Due to the energy conservation principle, which implies that energy flowing through differential surface perpendicular to ray must be constant on its path to focus, for parabolic mirror, the power density of incident field increases towards the focal region depending on the ratio of distance from surface of mirror to focus (r) to focal length (f) and this ratio (r/f) may be expressed after some mathematical work

$$
\frac{2}{1 + \cos\alpha} \quad (2.31)
$$

while, for objective lens, it is

$$\cos^{1/2}\alpha \tag{2.32}$$

2) positive sign of e_x, e_y

x-component and y-component (equivalent to e_ρ) experience the phase jump (inverted direction of rotation in the XY plane) on the mirror surface which leads to sign change. The z component has no phase jump since z component arises from the reflection of components parallel to the plane of incidence (p-polarized) only.

3) inverted direction of propagation

The beam reflects on the mirror surface and hence the direction on propagation is inverted. Thus, the exponential has negative sign (negative z direction).

Applying these three points to equation (2.29), (2.30), we get;

$$E_z = -ikfI_{0,r} \tag{2.33a}$$

$$E_a = 0 \tag{2.33b}$$

$$E_r = kfI_{1,r} \tag{2.33c}$$

where E_z, E_a, and E_r are longitudinal, azimuthal, and radial components respectively, and

$$I_{o,r} = \int_{\alpha_0}^{\alpha_1} I_0(\theta)\frac{2sin^2\theta}{1+cos\theta}J_0(kr_p\sin\theta\sin\theta_p)exp(-ikr_p\cos\theta\cos\theta_p)\,d\theta \tag{2.34a}$$

$$I_{1,r} = \int_{\alpha_0}^{\alpha_1} I_0(\theta)\frac{\sin 2\theta}{1+cos\theta}J_1(kr_p\sin\theta\sin\theta_p)exp(-ikr_p\cos\theta\cos\theta_p)\,d\theta \tag{2.34b}$$

$I_0(\theta)$ is incident field to the paraboloidal mirror. In general the incident beam is assumed as a Bessel-Gauss beam with the field distribution as;

$$I_0(\theta) = Nexp(\frac{-r^2(\theta)}{\omega_0^2})J_1(\frac{2r(\theta)}{\omega_0}) \tag{2.35}$$

The comparison of longitudinal components with different parameters are described in [48], [49].

2.5 Measurement of fields in focal region

2.5.1 Measurement of laser fields

In the literature, there are several reports of the measurement of longitudinal component of laser using different methods. However, the measurement of the longitudinal electric field of radially polarized laser beam is not easy because of its non-propagating property. For example, it cannot be observed by any photodetector, because the magnetic field vanishes near the beam axis. Therefore, experimental observation and measurement of the longitudinal component is confined to indirect methods such as the use of knife-edge scanning method through photodiode detection (lens) (2001) [50], (2003)[18], the use of photoluminescence

molecules where the fluorescence of single molecules with fixed absorption dipole orientation are used as probes for the local field distribution (lens) (2001) [51] , the use of metal tips, the use of optical Kerr shutter method (lens) (2004) [52], the use of scanning near-field optical microscope (NSOM) with the aluminum coated fiber-tip as a probe (lens)(2005) [53], the use of nano-particle scattering where a subresolution point scatterer is placed in the focal region and through this the form of the field scattered back through the objective lens is examined (lens) (2003) [54], and the use of the quantum-well heterostructure photodetector where the amount of the electric field energy densities of the longitudinal and radial components are separately determined by using a semiconductor nanostructure. [55] . All these reports used the near field techniques to get the indirect observations and all their results show the strong longitudinal field component.

Recently, the observation of the longitudinal component of polarization was done by using conventional photoresist to record the intensity shape of the focal spot of radially polarized light (lens) (2007). [56].

As for the focusing of parabolic reflector, The measurement of longitudinal component of radially polarized beam in the focal region of parabolic mirror was reported by using gold tip at the focus as a probe (parabolic mirror) (2003) [57] , and recently by using photoluminescence molecules (2008)[20]

2.5.2 Measurement of microwave

As for the microwave regime, recently the measurements of the fields radially polarized waves in the focal area were reported using slot antennas which generate microwaves and focuses at the same time [11], [9], [10]. However, the slot antennas are equivalent to the lenses in optical devices. Here, we are interested in the fields in the focal region of the parabolic mirror.

2.6 Radially polarized waves

The radially polarized wave has the electric field in the radial direction with respect to propagation axis while magnetic field is aligned in an azimuthal orientation. It can be well described in cylindrical coordinates and its snapshot on the transverse plane has a doughnut-shape. The paraxial expression may be Bessel-Gaussian beam. The radially polarized beam in the free space is the analog of the TM_{01} mode with the circular wave guide. It has a special character on a propagation axis (z-axis). When focused, the on-axis electric field has only the longitudinal component without the radial and azimuthal components, and there is no magnetic field on axis[58]. Magnetic field is azimuthally polarized around the axis. It is convenient to apply the vectorial method for proper description of the electric fields [28].

2.7 Properties of longitudinal field in focal region

2.7.1 Properties of focusing

Our understanding on focusing of electromagnetic waves is basically the superposition of plane waves at the focus where the transverse components of the electric field constructively

interfere. The radially polarized waves thus create a longitudinal field along the propagation axis, while the linearly polarized waves create only transverse field.

In general, the electromagnetic plane waves have two main forces, i.e., 1) the electric force in the transverse direction (energy density) which does not propagate, and 2) radiation pressure force (Poynting vector) in the propagating direction (power density) which does propagate. In the focal region, both undergo the vectorial superposition resulting in gradient force for the former and absorption/scattering forces for the latter.

2.7.2 Properties of longitudinal field in focal region

Since the longitudinal electric component in focal region is the result of the superposition of the vectorial electric field of the plane waves [59], it has the following properties.

2.7.2.1 longitudinal field is oscillating, but non-propagating field

The longitudinal component of electric field in the focal region is purely the result of the vectorial properties of the static field and hence it is generally accepted that the longitudinal fields in the focal region do not propagate (i.e., static). They just form a reservoir of electric energy density. Thus, similar to a standing wave, there is no net momentum associated with the photons in the focus of a longitudinal mode [51].

As for the case of two-mirror system with transmitting and receiving antennas which will be described in Chapter 3, from the view point of the reciprocal principle of antenna, field in focal region is the reappearance of what happened at the transmitting antenna. At the transmitting antenna, we can assume that the radiation point source (current) oscillates along the element of the monopole antenna. This point reappears at the focal area as the focal point and this point oscillates along the same distance as the length of the element of monopole antenna with its own field distribution in the focal area.

As we will see later in Chapter 5 (quasi Bessel beam), the plane waves passing an axicon generate line focus instead of point focus. These successive focusing are referred to as propagation of Bessel beam and this propagation has superluminal velocity due to the geometric structure.

Also in the usual case of a point focus, the region near the focus is filled with the superposition of the transverse component of plane waves passing nearby with different magnitudes depending on the distance from the k vector. This phenomena occur successively according to the propagation of waves and hence this successive superposition may be called propagation. However, when we restrict our observation to the point focus, the field at the focus does not propagate.

2.7.2.2 Zero Poynting vector on focal axis

Right on the beam axis, there is no magnetic field and hence the Poynting vector is zero [60], [61], [7], and [62].

The intensity of Poynting vector is the time averaged one;

$$< S >_z = Re[(\frac{1}{\mu_0}\overline{E} \times \overline{B}^*)_z]/2 = Re[E_r B_\varphi^*]/2\mu_0 \tag{2.36}$$

Since $\mathbf{B}_\varphi = \frac{1}{c}(\hat{\mathbf{k}}_z \times \mathbf{E}_r)$,

$$
\begin{aligned}
< S >_z &= Re[E_r B_\varphi^*]/2\mu_0 \\
&= Re[|E_r|^2]/2c\mu_0 \\
&= \frac{1}{2}\sqrt{\frac{\varepsilon_0}{\mu_0}} Re[kf \int_{\alpha_0}^{\alpha_1} I_0(\theta) \frac{\sin(2\theta)}{1+\cos(\theta)} J_1(kr_p \sin\theta \sin\theta_p) e^{-ikr_p \cos\theta \cos\theta_p} d\theta]
\end{aligned}
\tag{2.37}
$$

We applied Equation (2.33c) and (2.34b) in the last line of Equation (2.37).

The Poynting vector near the focus for a radially polarized beam focused by the parabolic mirror is simulated in Fig. 2.4, which shows the Poynting vector is zero on the beam axis. It is peculiar phenomena when compared with linear or circular polarized waves.
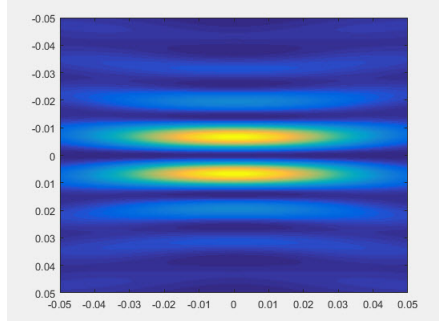
Figure 2.4: Poynting vector in the focal region of radially polarized beam

2.7.2.3   gradient force

Since the electric field intensity distribution in the focal area is inhomogeneous, the distribution creates the gradient force. This force generates the ponderomotive force which will be discussed in detail in Chapter 4. This force can also be exploited for the particle acceleration and the trapping of spherical particle [63].

2.8   Numerical simulations

The assumed initial Bessel-Gaussian beam based on Equation (2.35) is simulated compared with Gaussian beam in Fig. (2.5)
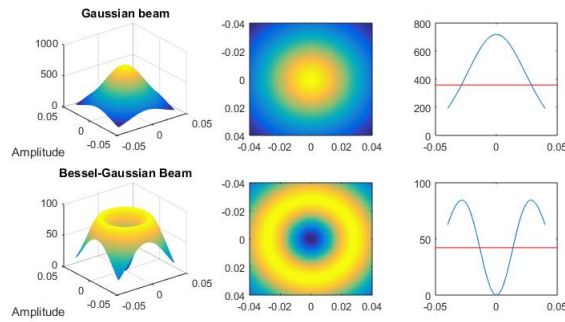
Figure 2.5: Gaussian beam and Bessel-Gaussian beam

The longitudinal and radial components in the focal region are simulated based on Equation (2.33) on focal plane (XY plane) by setting $\theta_p = \pi/2$ in Fig. (2.6).
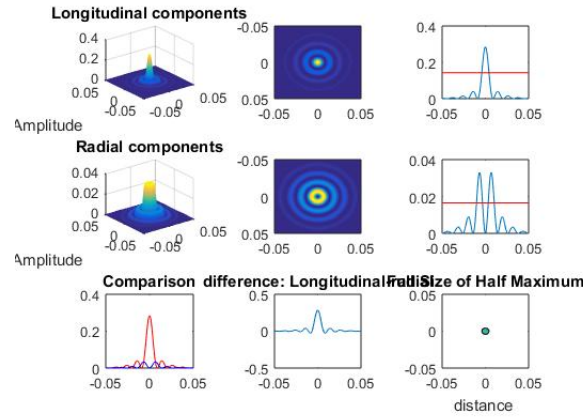
Figure 2.6: simulation on XY plane

The simulation on XZ plane by setting $\theta_p = 0$ is shown in Fig. (2.7).
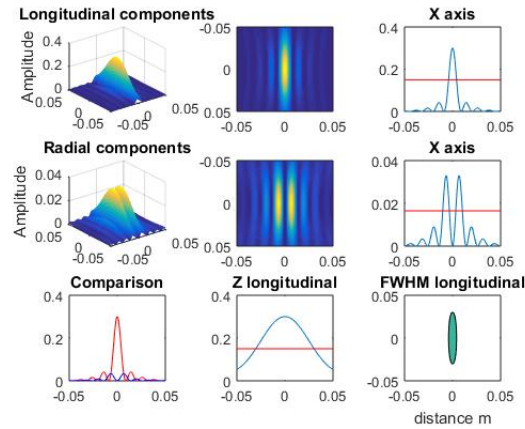
Figure 2.7: simulation on XZ plane

Chapter 3

Experiment

3.1 Experimental set-up

The goal of the experiment is the observation of the longitudinal component of the electric fields of the radially polarized microwaves in a focal region of parabolic reflector with high numerical aperture(NA). As already mentioned, for the optical regime, direct observation of longitudinal electric field of radially polarized beam in focal region is not easy due to its peculiar property that longitudinal fields do not propagate but oscillate along the optical axis while magnetic field vanishes in the region. The experimental observation of its spatial distribution was first reported in the literature in 2004 using a Kerr medium [64]. However, for the observation of longitudinal field of radially polarized microwave, it is enough simply to use a monopole antenna which is positioned in the direction of electric field.

3.1.1 Generating radially polarized microwaves

The first step to carry out the measurement is to create the radially polarized microwaves. There might be several ways to create radially polarized waves, e.g., using monopole antenna with wave guide of conical horn or cylinder. Here we chose the method of using transmitting monopole antenna with or without a circular ground plane positioned at focus of parabolic reflector along the optical axis.

 The diagrams and photographs of the experimental set-up are shown in Fig.3.1 and Fig. 3.2.

(a) system without ground plane   (b) system with ground plane
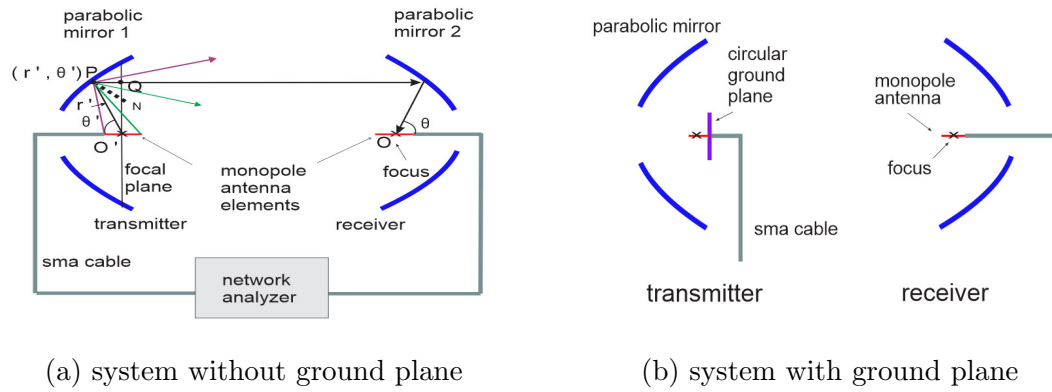
Figure 3.1: Diagram of experimental set-up

(a) photograph of mirrors   (b) whole system
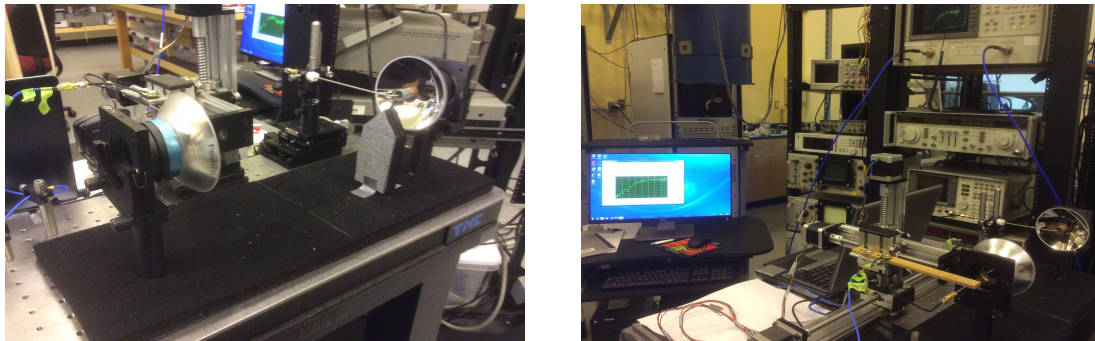
Figure 3.2: photographs of experimental set-up

The element (wire) of monopole antenna is the inner conductor of the coaxial feed line with length 4 mm (diameter 0.5 mm) protruded from the feed line (diameter of outer conductor 2.1 mm) (Fig. 3.3(a)). Diameter of circular disk (ground plane) is 25.4 mm (Fig. 3.3(b)). The radiation from the monopole antenna without ground plane is half wavelength wave and that from monopole antenna at the center of circular plane is quarter wavelength wave.
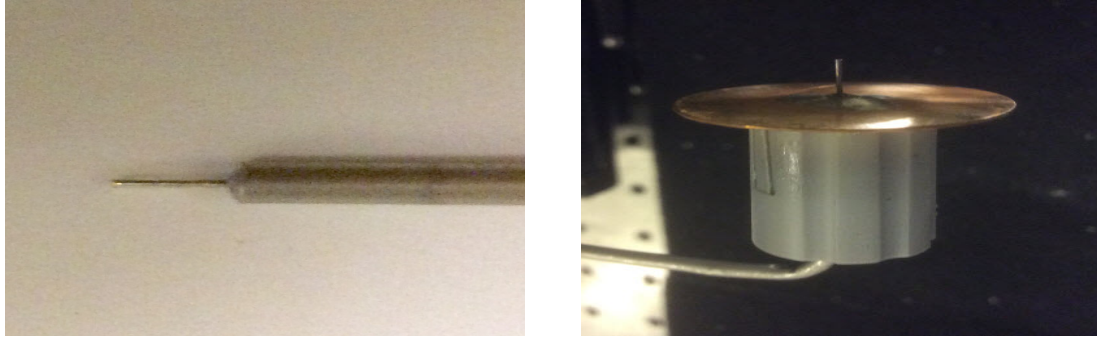
(a) monopole without ground plane   (b) monopole with ground plane

Figure 3.3: monopole wire and ground plane

The time-averaged radiated power density $(s(\theta))$ of the azimuthal symmetric monopole antenna without plane is given by [65, equation (3.2.14)],

$$s(\theta) = |E_\theta|^2/(2\eta) = (\eta/2)|H_\phi|^2 = \frac{\eta|I(0)|^2 f(\theta)}{32\pi^2 r^2 \sin^2(kh)} \tag{3.1}$$

where

$$f(\theta) \equiv \frac{[\cos(kh\cos\theta) - \cos(kh)]^2 + [\sin(kh\cos\theta) - \cos\theta\sin(kh)]^2}{\sin^2\theta} \tag{3.2}$$

The radiation pattern plotted with Equation (3.1) for frequency 19 GHz, wire length 4 mm, assuming $I(0)$ to be unity, is shown in Fig. 3.4(a). As for the monopole antenna at the center of circular ground plane, we adopt the simulation of Zivkovic et al.[66] for the case where the radius of plane equals to wavelength as shown in Fig. 3.4(b).

Radiation pattern of monopole
at the center of circular plane,
radius of plane (a)=wavelength(λ)
Zivkovic (2012)
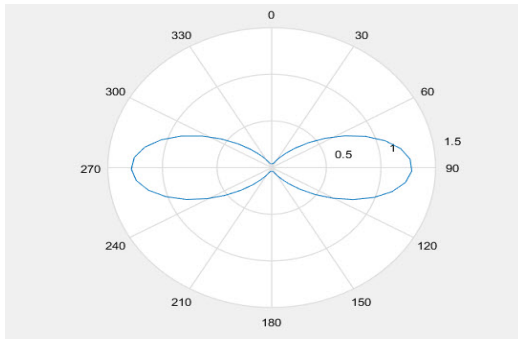
(a) Radiation pattern of monopole without plane   (b) Radiation pattern of monopole with plane
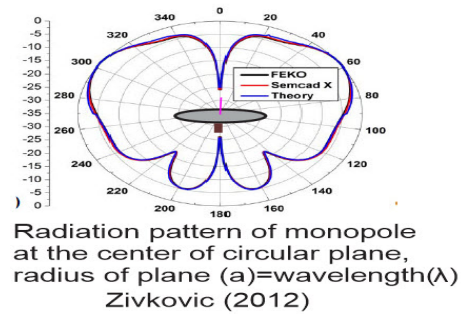
Figure 3.4: radiation pattern of monopole antenna

The waves generated by the monopole antenna are reflected by the parabolic mirror (diameter 100 mm, focal length 19 mm) with a hole (diameter 30 mm) at the center (Fig . 3.5). The numerical aperture is $NA = n\sin(\pi/2) = 1$.
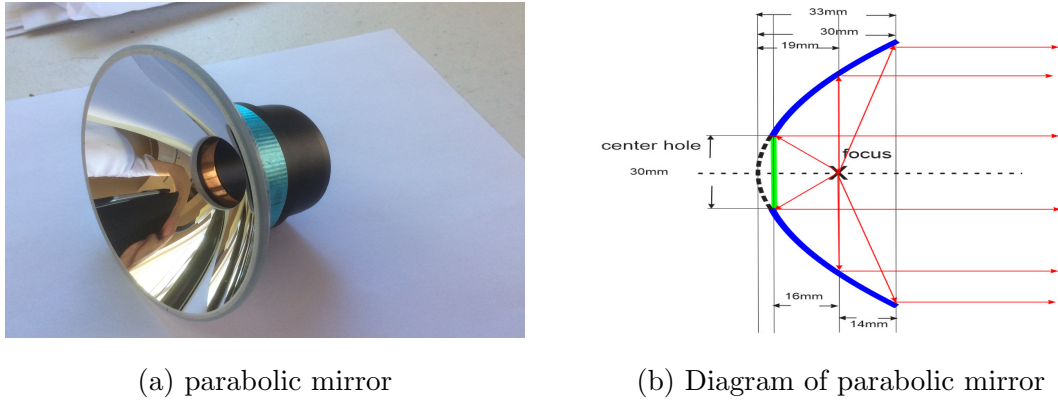
(a) parabolic mirror   (b) Diagram of parabolic mirror

Figure 3.5: Parabolic reflector

The monopole antenna is positioned at the focus of the mirror along the optic axis. The reflected waves form the radially polarized microwaves in the direction of z axis of the antenna as shown in Fig. 3.6(a). These waves have a shape of doughnut with amplitude distribution corresponding to the radiation gain of the antenna. This doughnut shape is confirmed by the measurement of the field in the radial direction along the diameter of the vertical plane in front of the reflection mirror as shown in Fig.3.6(b).
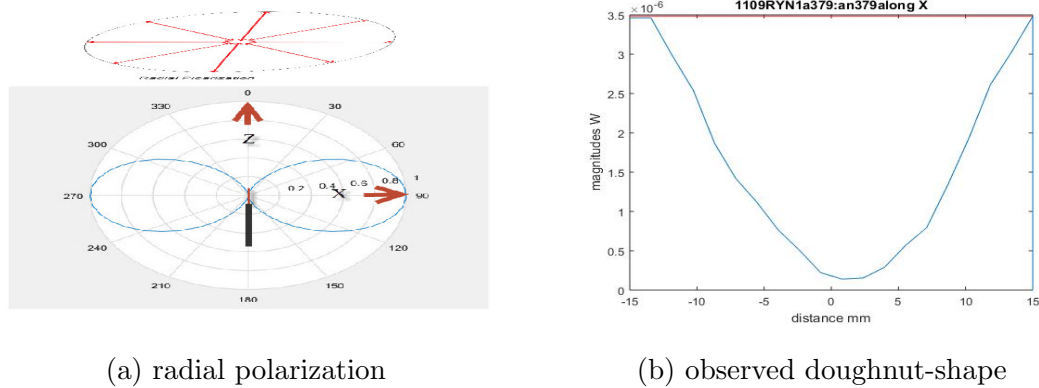
(a) radial polarization   (b) observed doughnut-shape

Figure 3.6: radial polarization

Three-dimensional geometry of a paraboloidal reflector system is shown in Fig. (5.8).
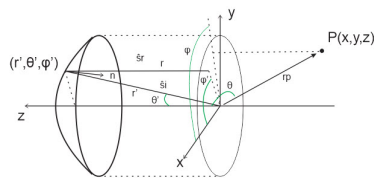
Figure 3.7: geometry of parabolic mirror

There are two most commonly used methods in analyzing radiation characteristics of the reflectors, i.e., current distribution method in which the current density is integrated

over the surface of the reflector, and aperture distribution method in which field reflected from the paraboloid is first found and then integrated over the surface of the aperture plane perpendicular to z-axis assuming equivalent sources are formed over the aperture plane [67]. We apply the aperture distribution method here. On the focal plane, electric field of illuminating beam is,

$$\boldsymbol{E} = C\sqrt{\boldsymbol{G}_f(\theta', \phi')}\frac{\exp(-jkr'(1+\cos\theta'))}{\boldsymbol{r}'}\hat{\mathbf{e}}_{\mathbf{r}} \tag{3.3}$$

where C is $\sqrt{\frac{\eta P_t}{2\pi}}$, η is impedance of free space 376.7Ω, P_t is total power and $\boldsymbol{G}_f(\theta', \phi')$ is a gain function.

If we assume the gain function as Bessel-Gaussian function, then electric field on focal plane is given by,

$$\boldsymbol{E} = C_1\sqrt{\exp(\frac{-r^2}{w_0^2})\mathrm{J}_1(\frac{2r}{w_0})}\frac{\exp(-jkr'(1+\cos\theta'))}{\boldsymbol{r}'}\hat{\mathbf{e}}_{\mathbf{r}} \tag{3.4}$$

For the system of monopole antenna without ground plane and reflection mirror, the gain function G in the form of the directivity ($d(\theta)$) in the far field is[65],

$$d(\theta) = \frac{f(\theta)}{Cin(2kh) - \sin^2(kh)} \tag{3.5}$$

where h is the length of the monopole wire, θ is polar angle in spherical coordinates, $f(\theta)$ is found by Equation (3.2), and

$$C_{in}(z) = \int_0^2 (1-\cos t)dt/t \tag{3.6}$$

The system is assumed to be azimuthal symmetric.

For electrically short monopole wires ($kh << 1$), the directive gain is reduced to[65, equation (3.2.20)]

$$d(\theta) = \frac{3}{2}\sin^2(\theta) \tag{3.7}$$

Applying Equation (3.7), the electric field on the aperture plane becomes

$$\boldsymbol{E} = \sqrt{\frac{\eta P_t}{2\pi}\frac{3}{2}\sin^2(\theta))}\frac{\exp(-jkr'(1+\cos\theta'))}{\boldsymbol{r}'}\hat{\mathbf{e}}_{\mathbf{r}} \tag{3.8}$$

3.1.2 Data taking

In the receiver side, another parabolic reflector is used which is aligned on the optical axis of the transmitting mirror at the distance of 0.3 m. The probe monopole antenna without plane is set at the focus in the axial direction.

The data is taken through the vector network analyzer HP8720C which sweeps the frequency range 50MHz to 20GHz with maximum power 20 dBm (0.1 watt). The probe antenna sweeps the finite range of approximately 20x20mm by automatic translation stations with stepper motors which were assembled in the laboratory with three linear translation stations for 3D direction (XYZ). The probe antenna moves a preset distance (1 mm) for

5 seconds and stay still for 1 second and at this moment the network analyzer takes data automatically controlled by the Labview program in the computer.
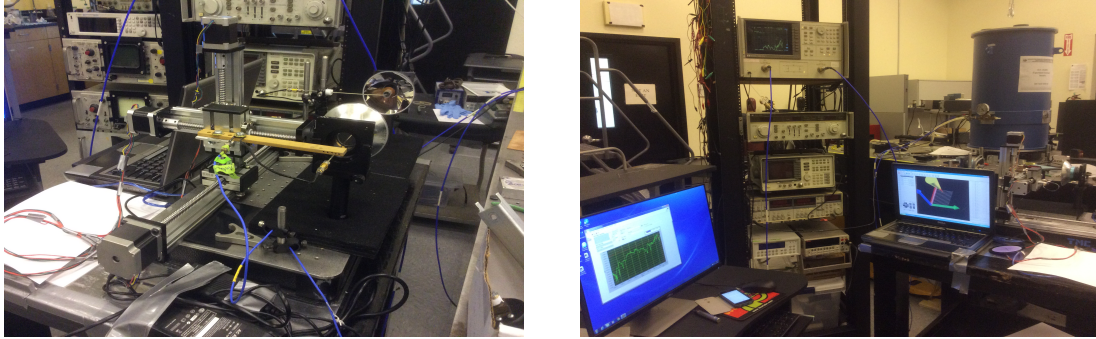
(a) auto translation station

(b) whole system of automatic data taking

Figure 3.8: automatic data taking system

3.2 Results

The results of observations are as follows;
The magnitudes of the intensity are not to scale. There are almost no differences between the observations with monopole antenna without plane and monopole antenna with circular plane except for the magnitudes of the measurements which are ignored here because magnitudes vary in every measurement. This unstable figure is considered as the result of the settings (e.g., alignment), efficiency of reflection of mirrors and environmental situations which are not exactly the same each time.

3.2.1 Longitudinal component

3.2.1.1 On focal plane (XY plane)

The longitudinal component on the focal plane (XY plane) is shown in Fig.3.9.

(a) contour

(b) surf

(c) X-line including maximum point

(d) Y-line including maximum point

(e) spot size (above half maximum)
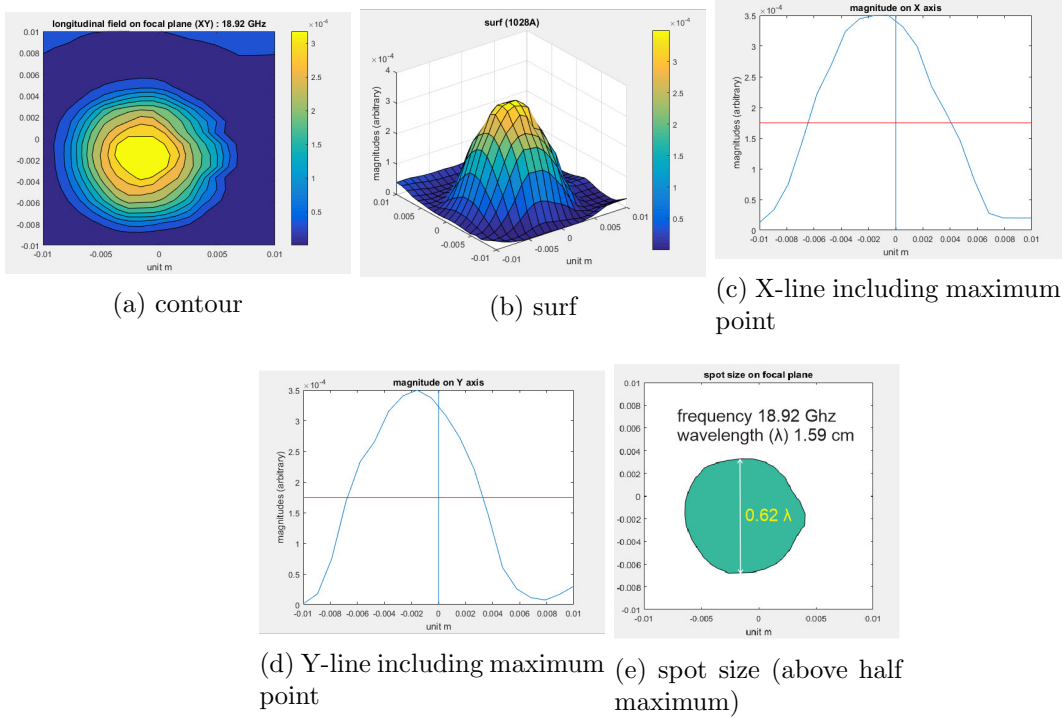
Figure 3.9: longitudinal component on XY plane

Fig. 3.9(a) is contour plot of the power intensity of longitudinal field component on the focal plane and (b) is its surf plot. They illustrate that the longitudinal component is the strongest at the center of the focal plane. (c) is 2D plot of intensity along the line in x direction passing the point of the maximum value. Half maximum is shown by red line. (d) is 2D plot of intensity along the line passing the point of the maximum value in y direction. (e) shows the spot size (area covering all points with the magnitude above half maximum. The diameter of the spot size is approximately two thirds of wavelength. It is two times larger than the theoretical prediction. The difference arises from the physical setup problems e.g., actual alignment of the system. The center of the spot size also does not coincide with the center of graph coordinates due to the alignment problem between two mirrors.

3.2.1.2   On YZ plane

The longitudinal field on the plane made by the propagation z axis and y axis is shown in Fig. 3.10.

The horizontal length along z axis of the half maximum is approximately one wavelength. The vertical length is approximately a half wavelength. The difference of the heights of the half maximum areas between the results of XY plane and XZ plane may be attributed to the difference of alignment.

(a) contour

(b) surf

(c) Z-line including maximum point

(d) Y-line including maximum point

(e) spot size (above half maximum)
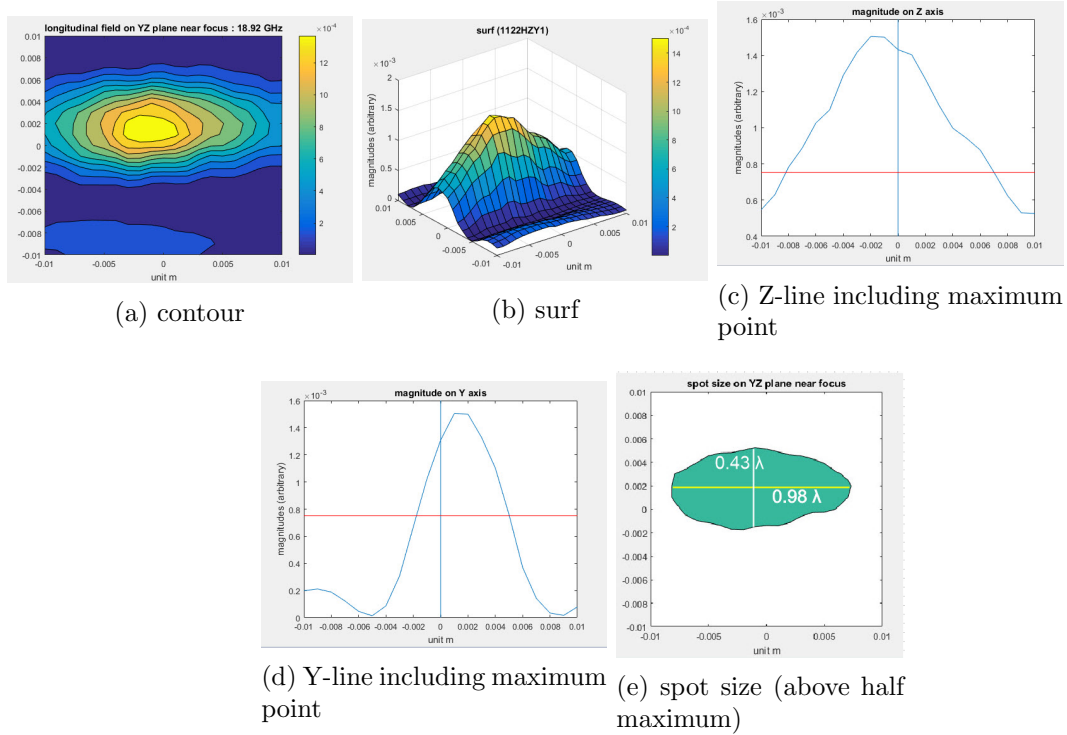
Figure 3.10: longitudinal component on YZ plane

3.2.2 Radial component

It is not easy to measure the radial component since the direction of the probe antenna should be radially oriented. The measurement was done by scanning the focal plane with the probe antenna fixed in the direction of x axis. Fig. (3.11) shows its results. The fact that there are two bright regions in symmetric locations implies that they are two diagonal points of a ring with the center at z axis. Bright areas nearby are created by the x-directional components of radial fields on the spots in those areas. We can assume that there is a ring of radial component which agrees with the simulation.

(a) radial field on X axis contour

(b) radial field on X axis surf

(c) radial field on X axis (half maximum)
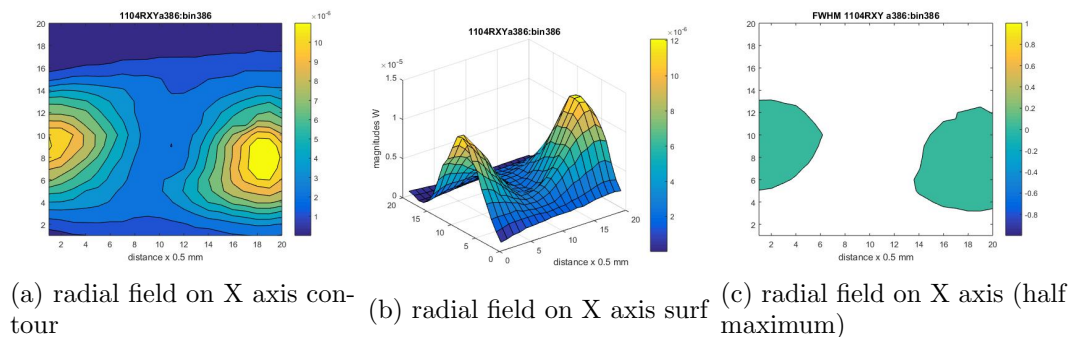
Figure 3.11: radial component on X axis

3.2.3 Comparison

The comparison of relative magnitude between longitudinal and radial fields is shown in Fig. 3.12.

Fig. 3.12(a) illustrates the comparison of relative magnitudes between longitudinal component and radial component for the sweeping range of frequency is 0.4GHz to 20GHz with the probe antenna positioned at the focus along the z axis for the longitudinal component and along x axis for the radial component. Fig. 3.12(b) shows the comparison of the magnitudes between longitudinal component and radial component along x axis. They show that the longitudinal component has the magnitude more than ten times higher than that of radial component.
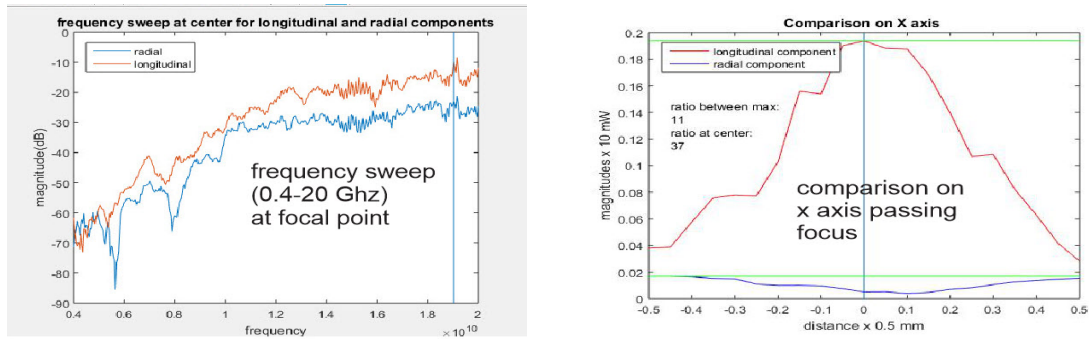
(a) comparison on monitor graph   (b) comparison of magnitude

Figure 3.12: comparison of magnitude

3.2.4 Conclusion

We summarize the results of observation as follows,

- The longitudinal components of electric field of radially polarized microwave (around 19 GHz) are measured at focal area of high NA parabolic mirror

- The observed components approximately agree with theoretical predictions

- Intensities of longitudinal components are more than ten times stronger than those of radial components

- The spot size is about a half wavelength wide and one wavelength long

Part II

Applications

Chapter 4

Particle acceleration

4.1 Introduction

The particle acceleration through laser beams has been investigated for decades. Shimoda [68] first suggested to use optical maser for accelerator in 1962 and Scully[69] investigated the possible application of the longitudinal component of laser beam for laser linac in 1990. Most conventional accelerators employing microwaves with cavities requires enormous amount of cost and size, and have been confronted with the restrictions in energy level due to the breakdown (in order of 10 to 50 MV/m)[70],[71],[72]. After the advent of laser, the acceleration through laser beams has attracted great interests due to their capabilities to realize high power density. The power of the laser pulses with femtoseconds duration time reaches terawatts even though input energy is only several millijoules. It has been achieved to generate maximum intensity $10^{22}W/cm^2$ by focusing a terawatts level laser beam to a focal spot size of $0.8\mu m$ with an f/0.6 off-axis paraboloid in the free space [73], [74]. However, the progress has not been straightforward due to the difficulties arising from Lawson-Woodward theorem (phase matching), collimation, and also the near-by material breakdown. Lots of proposals have been made theoretically and demonstrated experimentally.

Among them, direct acceleration of electrons in vacuum by focusing ultra-intense radi- ally polarized laser beam has received particular attention because[75] ,
1) since this scheme operates in the infinite vacuum, there is no breakdown problems and hence no limit on the laser field intensity that may be used,
2) this scheme can take advantage of the strong longitudinal electric field component at the beam center,
3) the off-axis radial electric and azimuthal magnetic field components help confine electrons to the vicinity of the beam axis[76],
4)the acceleration is linear and hence radiative energy losses will be low [29].

The usual acceleration pattern with the longitudinal field is the acceleration by pondero- motive force. However, if the accelerating field in the focal region has ultra-relativistic laser intensities, i.e., the normalization factor $a_0 > 1$, the particles are accelerated by sub-cycle pattern to get energy gain in the level of GeV [29].

Meanwhile, little attention has been given to the microwave acceleration in free space because of its incapability in providing high power intensity compared with laser. However, the big physical scale of microwave due to the low frequency may provide special features.

Here, we are interested in free space microwave acceleration through the strong longitudinal electric field created by radially polarized microwave which is tightly focused by parabolic mirror.

4.2 Lawson-Woodward theorem

4.2.1 Lawson-Woodward theorem

In conceiving the accelerator of particle through electromagnetic field, it is necessary to pay a special attention to the Lawson-Woodward theorem. The theorem states that the net energy gain of an electron interacting with an electromagnetic field in vacuum is zero under conditions as follows;

(1) the laser field is in vacuum with no walls or boundaries present,

(2) the electron is highly relativistic ($v \cong c$) along the acceleration path, which implies that the particle is moving in straight line with constant velocity,

(3) no static electric or magnetic fields are present,

(4) the region of interaction is infinite,

(5) ponderomotive effects (nonlinear forces, e.g., the $v \times B$ force) are neglected [77],[78],[79],[80],[81].

We follow the reference [77] in deducing the theorem.

The plane wave with x polarization propagating in the z direction in free space is,

$$\mathbf{E} = E_0 \cos(\omega t - \frac{\omega}{c}z + \phi)\hat{x}$$
$$\mathbf{B} = \frac{1}{c}E_0 \cos(\omega t - \frac{\omega}{c}z + \phi)\hat{y} \tag{4.1}$$

The Helmholtz equation for wave in vacuum is,

$$\nabla^2 E + (\frac{\omega}{c})^2 E = 0 \tag{4.2}$$

Fourier expression of z-component of electric field is given by,

$$\mathbf{E}(z) = \frac{1}{2\pi} \int dk_x \int dk_y \tilde{E}_z(k_x, k_y) exp[i(k_x x + k_y y + k_z z - \omega t)] \tag{4.3}$$

where $\tilde{E}_z(k_x, k_y)$ is Fourier amplitude and $k_z^2 = (\frac{\omega^2}{c^2} - k_x^2 - k_y^2)$ vacuum dispersion relation.

Since electromagnetic fields in vacuum satisfy

$$\nabla \cdot \mathbf{E} = 0 \tag{4.4}$$

Fourier amplitude $\tilde{E}_z$ is

$$\tilde{E}_z = -(k_x \tilde{E}_x + k_y \tilde{E}_y)/k_z \tag{4.5}$$

and $\tilde{E}_y$ can be assumed to be zero resulting in $\tilde{E}_z = -(k_x/k_z)\tilde{E}_x$.

The total energy gain is

$$\mathcal{E} = \int_{-\infty}^{\infty} dz E_z \qquad (4.6)$$

By putting Equation (4.3) into Equation (4.6), we get

$$\mathcal{E} = \int_{-\infty}^{\infty} dz \frac{1}{2\pi} \int dk_x \int dk_y \tilde{E}_z(k_x, k_y) exp[i(k_x x + k_y y + k_z z - \omega t)] \qquad (4.7)$$

For a highly relativistic electron ($v \cong c$, $t = z/c$) moving along the z axis, $x = y = 0$,

$$\begin{aligned} k_x x + k_y y + k_z z - \omega t &= k_z z - \omega z/c \\ &= z(k_z - \omega/c) \end{aligned} \qquad (4.8)$$

and by using integral table for exponential over infinity,

$$\delta(x - y) = \frac{1}{2\pi} \int_{-\infty}^{\infty} dk \exp ik(x - y) \qquad (4.9)$$

we get,

$$\begin{aligned} \int_{-\infty}^{\infty} dz E_z &= \int_{-\infty}^{\infty} dz \frac{1}{2\pi} \int dk_x \int dk_y \tilde{E}_z(k_x, k_y) exp[i(k_x x + k_y y + k_z z - \omega t)] \\ &= \int dk_x \int dk_y \tilde{E}_z(k_x, k_y) \frac{1}{2\pi} \int_{-\infty}^{\infty} dz \exp[iz(k_z z - \omega/c)] \\ &= \int dk_x \int dk_y \tilde{E}_z(k_x, k_y) \delta(k_z - \omega/c) \end{aligned} \qquad (4.10)$$

To make the equation clearer, we introduce a change of variables; $k_x = k_\perp \cos \phi$ and $k_y = k_\perp \sin \phi$, where $\int dk_x \int dk_y = \int d\phi \int dk_\perp k_\perp$ and $\delta(k_z - \omega/c) = (k_z/k_\perp)\delta(k_\perp)$ and we get,

$$\int_{-\infty}^{\infty} dz E_z = -\int d\phi \int dk_\perp (k_\perp \cos \phi) \tilde{E}_x(k_\perp \cos \phi, k_\perp \sin \phi) \delta(k_\perp) \qquad (4.11)$$

When we assume $k_\perp \to 0$ to get the non-zero delta function, $k_\perp \tilde{E}_x \to 0$ and the result of Equation (4.11) is zero, which means there is no energy gain.

4.2.2   Schemes evading Lawson-Woodward theorem

A major difficulty in using laser fields in vacuum to accelerate particles is the discrepancy of the phase velocities between particle and the accelerating beam. Furthermore, if the beam is focused, the phase velocity of the longitudinal field is superluminal due to the geometrical feature. For example, a certain calculation in paraxial limit is given by [82],

$$V_{phase} = c \left[1 - \frac{(\lambda_0/\rho_0)^2}{\pi^2(1 + z^2/z_R^2)} \right]^{-1} \qquad (4.12)$$

where z_R is Rayleigh length.

Therefore, the particle can not catch up the velocity of the beam and slips behind.

If the particle interacts over an infinite region (condition four) i.e., a distance much large compared to the slippage distance, the accelerating and decelerating regions cancel, resulting in zero net energy gain. This is the main point of the Lawson-Woodward theorem.

To evade the application of the Lawson-Woodward theorem, a lot of attempts have been made to conceive the situations which do not satisfy at least one of the above five conditions.

One way is adding medium in the path of the beam to reduce the beam velocity and hence the slippage such as inverse Cherenkov acceleration [83],[84]. Plasma wakefield acceleration [85], [86] is also based on the use of medium. However, these methods invoke another problems such as material breakdown or wave-breaking regime limitations[87]. Therefore, direct acceleration in vacuum is preferable.

The other way to evade the critical cancellation is a method using gradient electric field where gradual energy gain is possible as the remaining effect of cancelation. Another way may be a method reducing the interaction region such that the electron can get out of the interaction region after gaining energy from the accelerating phase before the decelerating phase begins. The former is ponderomotive acceleration and the latter includes sub-cycle acceleration and one-kick acceleration as illustrated in Fig.4.1.
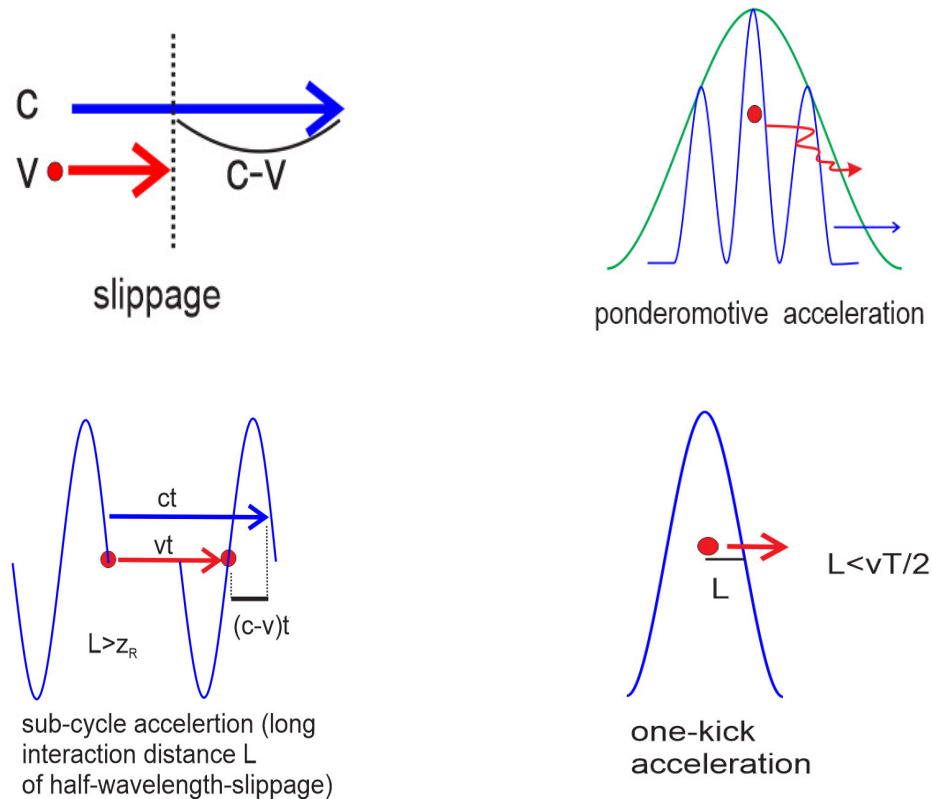
Figure 4.1: different models of vacuum acceleration

4.3   Ponderomotive acceleration

4.3.1   Non-relativistic ponderomotive force

The ponderomotive force occurs in spatially varying high frequency electric fields. The longitudinal field of focused radially polarized electromagnetic waves is gradient in magnitude and hence provides the acceleration of particle based on ponderomotive force.

Consider a charged particle in a high frequency electric field with an amplitude that varies smoothly in space, $E(x,t) = E_0(x)\cos(\omega t)$. The particle will oscillate sinusoidally. If field is stronger to the right and weaker to the left, then there appears a difference in magnitudes between forward push by the strong field and backward push by the weaker field, which produces a net result of displacement to the weaker field. This displacement continues in succeeding cycles as an acceleration away from the region of strong field. The average force over time is called ponderomotive force.

We first consider the case where the particle moves non-relativistically.

Referring to Fig.(4.2), a particle with initial velocity v_0 starts to interact with the accelerating phase of the wave at an arbitrary position a and becomes accelerated by gaining energy $E1$ while moving over the distance $\ell1$. The phase changes into deceleration when the particle arrives at the point b where the slope of the gradient of the longitudinal field is S. Now, the particle experiences the decelerating phase which is getting weaker due to the sharp slope while still moving in the same direction or backward over $\ell2$ until the phase changes into acceleration again after the full cycle of oscillation losing the energy $E2$. The net energy gain will be the difference between the values of two energy exchanges $E_{gain} = E1 - E2$. This can happen at any position if the slope S of the gradient of the field where the particles meets phase change is negative with respect to the motion direction. This will repeat until the particle escape from the range of longitudinal field completely. This is the basic mechanism of the non-relativistic ponderomotive acceleration.
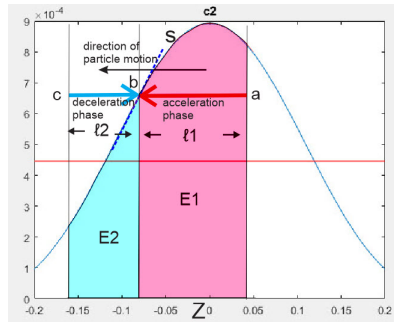
Figure 4.2: mechanism of energy gain

Mathematical expression of ponderomeotive force is

$$F_p = -\frac{q^2}{4m\omega^2}\frac{d}{dx}(E_0^2) \tag{4.13}$$

We can derive it starting from the force equation [88],[89, section 30],[90],

$$F = m\ddot{x} = qE = qE_0(x)\cos\omega t \tag{4.14}$$

To make the situation clearer, we decompose x into two components i.e., a slowly varying component (net result of displacement toward the weaker field) x_0 which is the spatial time average over short time $2\pi/\omega$ so $x_0 = \bar{x}$ and called the oscillation center, and a rapidly oscillating component x_1. Therefore, $x = x_0 + x_1$. The time average of x_1 is zero since the oscillating values are cancelled in time averaging.

Assuming $E_0(x)$ is infinitely differentiable, we make a Taylor expansion of $E_0(x)$ about the oscillation center x_0 to the first order term,

$$
\begin{aligned}
E_0(x) =& E_0(x_0) + \frac{dE_0}{dx}(x - x_0) \\
=& E_0 + \frac{dE_0}{dx}x_1
\end{aligned}
\tag{4.15}
$$

where we exploited $E_0(x_0) = E_0$ and $x = x_0 + x_1$, and $\frac{dE_0}{dx}$ is to be evaluated at x_0. The force equation becomes,

$$
m(\ddot{x}_0 + \ddot{x}_1) = q\left(E_0 + x_1\frac{dE_0}{dx}\right)\cos\omega t
\tag{4.16}
$$

By averaging Equation (4.16) over time, we get ponderomotive force,

$$
m\ddot{x}_0 = q\frac{dE_0}{dx}\Big|_{x_0}\overline{x_1\cos\omega t}
\tag{4.17}
$$

From Equation (4.16) and by using approximation noting $\ddot{x}_1 \gg \ddot{x}_0$ due to high frequency of $\ddot{x}_1$ and $E_0 \gg (dE_0/dx)x_1$ as seen from the order of Taylor expansion, we get,

$$
m\ddot{x}_1 = qE_0\cos\omega t
\tag{4.18}
$$

By solving Equation (4.18) through integrating, we get,

$$
x_1 = -\frac{qE_0}{m\omega^2}\cos\omega t
\tag{4.19}
$$

Inserting this solution in Equation (4.17) and performing time average, we get,

$$
\ddot{x}_0 = -\frac{q^2E_0}{2m^2\omega^2}\frac{dE_0}{dx}
\tag{4.20}
$$

Finally, we get the ponderomotive force $F_p = m\ddot{x}_0$ by using Equation (4.20) and by exploiting $\frac{d}{dx}(E_0^2) = \frac{E_0}{2}\frac{dE_0}{dx}$,

$$
F_p = m\ddot{x}_0 = -\frac{q^2}{4m^2\omega^2}\frac{d}{dx}(E_0^2)
\tag{4.21}
$$

Equation (4.21) shows that the ponderomotive force is directly proportional to gradient of electric field intensity and inversely proportional to square of frequency. It is of interest to note that q^2 in Equation (4.21) implies that there is no difference between positive and negative charges.

The drawback of the ponderomotive acceleration is in its weak magnitude. The value of $\frac{q^2}{4m\omega^2}$ for frequency 10 GHz is 1.7795×10^{-30}.

The ponderomotive energy including oscillation energy is given by

$$
\mathcal{E}_p = \frac{q^2}{4m^2\omega^2}(E_0^2)
\tag{4.22}
$$

4.3.2 Non-relativistic dynamics

For the particle with slow initial velocity v_0, the non-relativistic velocity v_z of the particle when it arrives at z is

$$v_z^2 = v_0^2 + 2 \int_0^\ell a(z)dz \tag{4.23}$$

where ℓ is the distance the particle moves in the accelerating field $a(z)$.

The time elapsed during the whole passage is

$$\triangle t = \int_0^z \frac{dz}{v(z)} \tag{4.24}$$

If the particle reaches the weaker part of the field before the phase of the longitudinal field changes into the deceleration i.e., the time $\triangle t$ is equal to or shorter than half the period of the field, the accelerated particle will escape from region of strong field with the velocity v_f,

$$\triangle t \leq \frac{T}{2} = \frac{1}{2f} \tag{4.25}$$

$$f \leq \frac{1}{2\triangle t} \tag{4.26}$$

where f is the frequency and T the period of the field.

Then, upper-limit frequency will be

$$
\begin{aligned}
f &= \frac{1}{2\triangle t} = \frac{1}{2\int_0^\ell \frac{dz}{v(z)}} \\
&= \frac{1}{2\int_0^\ell \frac{dz}{\sqrt{v_0^2 + 2\int_0^\ell \frac{q}{m}\frac{1}{2}E(z)dz}}} \\
&= \frac{1}{2\int_0^\ell \frac{dz}{\sqrt{v_0^2 + \frac{qE\ell}{m}}}} \\
&= \frac{\sqrt{v_0^2 + \frac{qE\ell}{m}}}{2\ell}
\end{aligned} \tag{4.27}
$$

or

$$\ell = \frac{qE}{4mf^2} \tag{4.28}$$

The ratio g of interaction length ℓ to wavelength of incident wave is given by

$$g = \frac{\ell}{\lambda} = \frac{qE}{4m\lambda f^2} = \frac{qE}{4mcf} \tag{4.29}$$

Equation (4.29) shows g is dependent on inverse of frequency which suggests the difference between microwave-driven acceleration and laser-driven acceleration. Assuming the electric field is the same for both cases, g is greater for microwave acceleration than for laser acceleration in several orders of magnitude.

4.3.3 Relativistic laser ponderomotive force

Conventionally, a normalized amplitude of the electric field of the laser a_0, which is also called dimensionless field amplitude parameter [91]) and introduced in [92], is used to make a distinction between relativistic and nonrelativistic regimes, where

$$a_0 = \frac{qE}{mc\omega} \tag{4.30}$$

The nonrelativistic regime corresponds to the case $a \ll 1$ and the relativistic regime to $a_0 \geq 1$.

a_0 is almost the same quantity as g. However, g is derived here from the comparison between the time interval of moving particle and the period of the phase where wavelength is only the reference value, while a_0 is derived from the ratio of velocity of particle to that of the wave. Therefore, the main point for g is the spatial size of the longitudinal electric field and its gradient instead of the velocity of the wave.

The relativistic ponderomotive force has been derived by some authors[93], [94],[95] as[96] in a little different forms. One of them is [94],

$$\frac{d\overline{\mathbf{p}}}{dt} = -\frac{q^2}{\gamma mc^2}\nabla|\hat{\mathbf{A}}\perp|^2 \tag{4.31}$$

where the overbar denotes the slowly varying quantity in time and

$$\overline{\gamma} = \sqrt{1 + \frac{1}{m^2c^2}\left[\overline{|\mathbf{P}|^2} + 2\left|\frac{q}{c}\hat{\mathbf{A}}\perp\right|^2\right]} \tag{4.32}$$

where the term involving vector potential represents the contribution of the jitter motion of the electron to the transverse momentum.

4.3.4 Microwave-driven free space acceleration

The particle accelerators create the beams of accelerated particles. Therefore, particle-acceleration and beam-collimation are the basic function of accelerators. For vacuum laser acceleration (direct laser acceleration), two difficulties should be overcome i.e., the velocity mismatch between particles and laser beam which causes zero net energy gain as mentioned above, and particle scattering due to transverse electric fields which obstructs to form a beam.

When longitudinal field of tightly focused radially polarized laser beam is used, radial component and longitudinal component are separated spatially and radial component provides the ponderomotive force in the transverse direction causing the particles trapped near the z axis, and hence difficulties coming from transverse scattering may be avoided. In this case, only the velocity mismatch becomes the main issue. The phase velocity of laser beam along the beam path in the focal area is superluminal. If we consider that the electron gains energy from the wave while moving in the same direction of the wave propagation, we should admit that the electron can not catch up with this speed and hence slips experiencing acceleration and deceleration phases of the laser beam, which results in no energy gain. Most of the previous efforts to accelerate particles with lasers in free space concentrated in

solving this phase-match problem e.g., by way of limiting the length of interaction between laser and particle as mentioned in subsection 4.2.2.

4.3.4.1   Models of accelerator using two-mirror system

Two-mirror system of this work with a monopole antenna on one side and longitudinal electric field on the other side can be used for particle accelerator in different configurations as shown in Fig. 4.3.

(model 1)   (model 2)

(model 3)   (model 4)
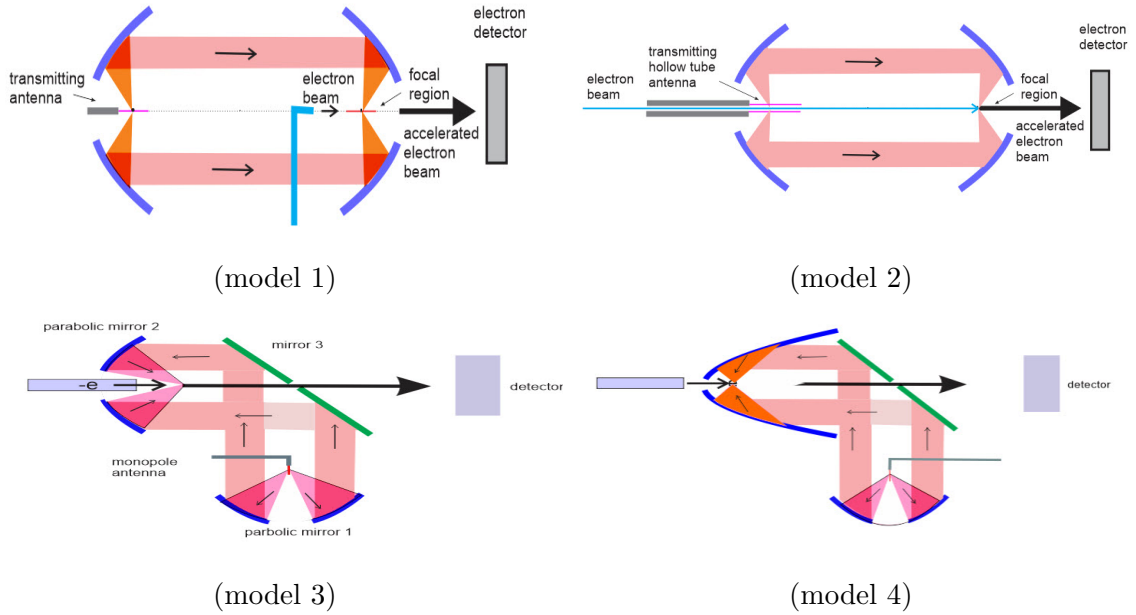
Figure 4.3: different models of two-mirror system accelerator

Since the oscillation of longitudinal field is symmetric along the z axis, there is no preferred or fixed direction between forward and backward on the z axis for the particle acceleration. However, if the particle has initial velocity, then resulting acceleration has the same direction as the initial one.

Referring to the Fig. 4.3, in model (1), particles are led through a tube and injected towards the hole of the receiving mirror for acceleration by the longitudinal field. Model (2) shows that particles are injected through the tunnel inside the leading tube and monopole antenna. The diameter (d) of the tunnel is much smaller than the wavelength ($d << \lambda$). Particles propagate through the center hole of the receiving mirror after being accelerated by the longitudinal field in the focal area of the receiving mirror. In model (3), incident field comes from the side of the system and is reflected by the plane mirror towards the focusing mirror. Particles are injected through the center hole of the focusing mirror and propagate through the center hole of the plane after being accelerated. Model (4) shows ultratight focusing acceleration where illuminating beam angle is greater than $\pi/2$. Model (4) presents an interesting phenomena and hence will be investigated in detail in section 4.6.

4.3.4.2   Comparison of ponderomotive forces

For the comparison of magnitudes of the ponderomotive forces between those of microwave and laser beam, we assume that the total input energy is the same for both cases, say 1 joule. By assuming pulse duration time as 1 femtosecond for laser and 1 nanosecond for microwave which are presently achievable (interestingly they are proportional to period (T) of the waves), frequencies (f) 1 GHz for microwave and 1 PHz for laser, and the lengths of spatial power distribution (gradient) the wavelength (λ) respectively as shown in Fig. 3.10, we get the ponderomotive force from Equation (4.21)

$$
\begin{aligned}
F_p &= \frac{q^2}{4m^2\omega^2}\nabla(E_0^2) \\
&= \frac{q^2}{4m^2(2\pi f)^2}\frac{1}{\lambda}\frac{2\eta_0 J}{T} \\
&= A\frac{1}{f^2}\frac{1}{\lambda}\frac{1}{T} \\
&= A\frac{1}{f^2}\frac{f^2}{c} \\
&= A/c
\end{aligned}
\tag{4.33}
$$

where c is speed of light and

$$
A = \frac{q^2 2\eta_0 J}{4m^2(2\pi)^2}
\tag{4.34}
$$

Equation (4.33) says that the ponderomotive forces in the above parameters are independent of the wave frequencies.

In other words, there are no differences in ponderomotive forces among laser and microwave for the assumptions mentioned above.

Dimensionless amplitude parameter

It is of interest to investigate the dimensionless field amplitude parameter a_0 of Equation (4.30) in microwave case compared with in laser case. In microwave regime, power intensity $10^{22}W/cm^2$ is not achievable. However, the relativistic dimensionless normalized value of amplitude $a_0 \geq 1$ is achievable since a_0 is inverse proportional to frequency.

We rewrite Equation (4.30),

$$
E^2 = a_0^2\frac{m^2c^2\omega^2}{q^2}
\tag{4.35}
$$

The power intensity is given by,

$$
\begin{aligned}
I &= \frac{E^2}{2\eta_0} \\
&= \frac{1}{2\eta_0}\left(\frac{a_0 mc\omega}{q}\right)^2
\end{aligned}
\tag{4.36}
$$

where η_0 is vacuum impedance with value $120\pi\Omega$.

The power is given by [97]

$$P = I\rho_0^2\pi\exp(1)/2 \tag{4.37}$$

By putting Equation (4.35), (4.36) and (4.37) together, we get,

$$P = \frac{\rho_0^2\pi\exp(1)m^2c^2\omega^2}{4q^2\eta_0}a_0^2 \tag{4.38}$$

From Equation (4.38), we see that the power is proportional to the square of frequency, which means that much higher power is needed to get the same value of normalized parameter a_0 for laser than for microwave.

Since frequency is lower in general microwave case than in general laser case by six orders of magnitude, the power intensity needed for the same value of a_0 can be much lower in microwave case by the same orders of magnitude.

For example, for $a_0 = 1$, the necessary power intensity is $1.5 \times 10^9 W/cm^2$ for microwave of frequency 10 GHz, while $1.4 \times 10^{18} W/cm^2$ for laser of frequency 0.3 PHz. The electric field equivalent to $1.5 \times 10^9 W/cm^2$ is $1.07 \times 10^8 V/m$. The current achievement of High Power Microwave (HPM) is in the level of GW [98], [99]. The possibility of the relativistic level of a_0 with microwave will lead to much more versatile vacuum accelerator.

Scaling analysis

As shown in Fig. 4.7, the ratio of longitudinal electric field on z-axis to wavelength is independent of frequencies. The only difference between microwave regime and laser regime is the scale. In microwave case, the wave length is much larger than that of laser and the physical interaction length is much longer.

Quantity of accelerated particles

Given a homogenous moving particle density, the numbers of the accelerated particles are proportional to the volume of the interaction space. This volume depends on the cross section and the length of the longitudinal component with accelerating phase. Both are larger in microwave case than in laser case by approximately five orders of magnitude, which means that larger number of particles can be accelerated per unit time in microwave acceleration than in laser acceleration. This implies that the microwave accelerator can provide higher luminosity $\mathcal{L}$, which is crucial in collider physics.

$$\frac{dR}{dt} = \mathcal{L} \cdot \sigma_p \tag{4.39}$$

where dR/dt is the number of events per second and σ_p the cross section.

Collimation and stability

The collimation and the stability of the on-axis trajectory is one of the major concerns for the particle accelerator. When longitudinal field of tightly focused radially polarized laser

beam is used, radial component and longitudinal component are separated spatially and the radial component, which surrounds the longitudinal component like a ring, provides the ponderomotive force in the transverse direction causing the particles trapped near the z axis, and hence this transverse ponderomotive force helps in solving transverse scattering problem. The depth (the length in the z direction) of longitudinal component is approximately proportional to the wavelength and the longer the depth is, the stronger the collimation and the stability would be. Accordingly, the microwave accelerator will be superior to the laser accelerator in this context.

Versatility of manipulation

However, the intensity of radial component is approximately ten times smaller than the intensity of longitudinal component. Therefore, we cannot rely completely on the transverse ponderomotive force and we might need additional field to collimate the particle beam. In this case, the practical manipulation of the system can be much easier in microwave case than in laser case due to the scale of cross section. For example, alignment of the system with the centimeter level focal spot size will be much easier than with the micrometer level spot size.

4.3.4.3   Radiation

In linear acceleration, the power radiated is given by [100],

$$P = \frac{2}{3} \frac{e^2}{m^2 c^3} \left(\frac{dE}{dx} \right)^2 \tag{4.40}$$

which shows the dependence only on the external forces.

The ratio of power radiated to power supplied by the external sources is,

$$\frac{P}{dE/dt} = \frac{2}{3} \frac{e^2}{m^2 c^3} \frac{1}{v} \frac{dE}{dx} \rightarrow \frac{2}{3} \frac{(e^2/mc^2)}{mc^2} \frac{dE}{dx} \tag{4.41}$$

which shows that the radiation loss in an electron linear accelerator will be negligible unless the gain in energy is of the order 2×10^{14} MeV/m while typical energy gains are less than that [100]. There is no difference between microwave accelerator and laser accelerator in this respect.

4.4   Reaction range and relativistic dynamics

In considering relativistic regime of acceleration, it is necessary to make clear the reaction zone between particle and field, and also necessary to review the relativistic dynamics of particle.

The most ideal scheme of the vacuum acceleration is that the particle is pushed by the accelerating phase of the beam and gains the energy sufficient enough to get out of the interaction region before the deceleration phase begins. In this case, since the particle has no time to experience the oscillation caused by the beam waves, the consideration of relativistic dynamics is enough to treat the case.

1) The definition of the interaction region in focal area is somewhat ambiguous since the electric field intensity has the gradient form.

Hartemann et al.[91] assumed the beam waist at focus (w_0) of Gaussian beam to be the interaction area of transverse component of field and formulated the linearly polarized beam power needed for the particle to escape the area.

For the focused radially polarized beam, electric field in focal region is longitudinal and hence the interaction zone should be defined in the axial direction. In the non-paraxial limit, the spot size of the longitudinal field on XZ plane may be a reasonable candidate but not compulsory. The side slope of the magnitude curve on z axis is steep and any point on the sharp slope may provide the range of the interaction in context of acceleration.

We assume full width of half maximum (FWHM) of the intensity distribution curve on the z-axis as the dominant interaction region for convenience.

2) To describe the relativistic dynamics of particle in electromagnetic field, we start with the conventional Lorentz force equation,

$$\mathbf{F} = \frac{d\mathbf{p}}{dt} = q(\mathbf{E} + \mathbf{v} \times \mathbf{B}) \tag{4.42}$$

and momentum

$$\mathbf{p} = \gamma m \mathbf{v} \tag{4.43}$$

We define the symbols m, q and $\mathbf{v}$ as particle's rest mass, charge, and velocity, respectively, c is the light velocity in vacuum, $\beta = \mathbf{v}/\mathbf{c}$, and $\gamma = (1 - \beta^2)^{-1/2}$.

The time rate of the energy transfer from the field to the particle is the power transferred,

$$\mathbf{P} = \frac{d\mathcal{E}}{dt} = q\mathbf{E} \cdot \frac{d\mathbf{z}}{dt} = q\mathbf{E} \cdot \mathbf{v} \tag{4.44}$$

where

$$\mathcal{E} = \gamma m c^2 \tag{4.45}$$

Accordingly,

$$\frac{d\gamma}{dt} = \frac{q}{mc^2}\mathbf{E} \cdot \mathbf{v} \tag{4.46}$$

which implies the energy transfer.

Another important quantity for particle trajectory is the acceleration. We can derive it from Equation (4.42) by expressing its left-hand side in terms of $\mathbf{v}$ instead of $\mathbf{p}$ using Equation (4.43)

$$\frac{d\mathbf{r}}{dt} = \mathbf{v} \tag{4.47}$$

The acceleration is

$$\frac{d\mathbf{v}}{dt} = \frac{q}{\gamma mc}[\mathbf{E} + \mathbf{v} \times \mathbf{B} - \frac{\mathbf{v}}{c^2}(\mathbf{E} \cdot \mathbf{v})] \tag{4.48}$$

If there is no magnetic field ($\mathbf{B} = \mathbf{0}$) and the particle is injected at $r = 0$ in the direction of z, then,

$$\frac{dz}{dt} = v_z \tag{4.49}$$

$$\frac{dv_z}{dt} = \frac{q}{\gamma^3 m} E_z(r=0) \tag{4.50}$$

4.5   Sub-cycle acceleration

The key idea of the sub-cycle acceleration is as follows. If velocity of particle is relativistic, the length of slippage will occur very slowly and particle can propagate an appreciable distance longer than Rayleigh length in paraxial limit in accelerating phase of beam. If the magnitude of field is ultrahigh, then particle will keep gaining energy from beam.

Varin et al.[101] defined the on-axis longitudinal electric field as

$$E_z = Re[\tilde{E}_z \exp(j\omega t)$$
$$= \frac{E_0}{\sqrt{1 + \left(\frac{z-z_f}{z_0}\right)^2}} sin\left(\omega t - kz + arctan\left(\frac{z-z_f}{z_0}\right) - \phi_0\right) \tag{4.51}$$

where ϕ_0 is the field initial phase, and simulated Equations (4.49), (4.50) with various power intensity.

Their numerical simulations have revealed that, when the laser intensity is low ($10^{14}W/cm^2$ or lower) and electron initial energy is low, the electron energy gain is very low, while, with high power intensity $10^{22}W/cm^2$ or ultra-high initial energy, high energy gain is achieved over one-half cycle of interaction length.

Several other authors also have reported the results of simulations with various power densities of $a_0 > 1$ [102], [103], [104] .

For the case where $a_0^2 < 1$, the regime of particle dynamics is non-relativistic which belongs to the ponderomeotive acceleration model, while for $a_0^2 > 1$ particle dynamics is relativistic and sub-cycle acceleration occurs[82].

This idea has been experimentally demonstrated for the electrons which are initially at rest in gas in 2013[82] and for the electrons which are pre-accelerated in 2016[87] in the schemes as shown in Fig. 4.4.

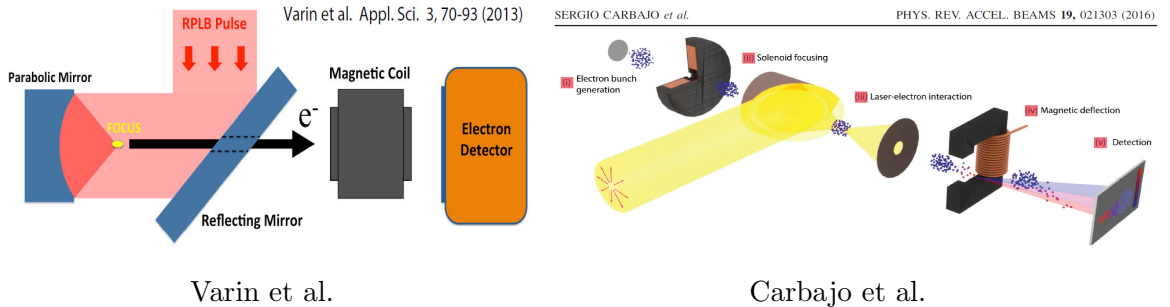Varin et al.   Carbajo et al.

Figure 4.4: schemes of sub-cycle acceleration experiments

However, both of them have just showed the proof of principle with the tiny result of energy gain 23 keV (with $a_0 = 1.7$, intensity $7.2 \times 10^{17} W/cm^2$) in [82] and 12 keV (with $a_0 = 5$, intensity $5.36 \times 10^{19} W/cm^2$) in [87].

4.6 Ultratight focusing acceleration

4.6.1 Definition of ultra-tight focusing

Ultratight focusing of radially polarized waves through parabolic mirror may provide a good circumstance for reducing the interaction region between particle and the longitudinal electric field since the length of the spot size along the z direction can be reduced by optimizing the range of incident beam integral angle to the focus as shown in what follows.

We define 'ultratight focusing' as the focusing with the highest integral angle which exceeds 90^0 and the lowest angle which reaches around 10^0 as shown in Fig. 4.5.
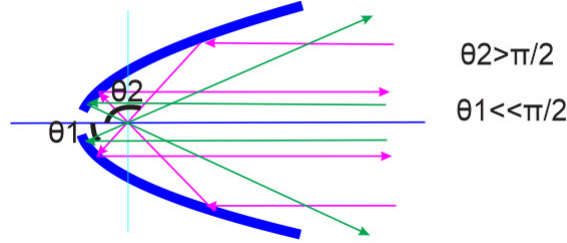
Figure 4.5: Ultra-tight focusing

4.6.2 Dependence of axial length on subtending angle range

By applying the Equation (2.33a) and (2.34a), the longitudinal field is,

$$E_z = -ikf \int_{\alpha_0}^{\alpha_1} I_0(\theta) \frac{2sin^2\theta}{1+cos\theta} J_0(kr_p \sin\theta \sin\theta_p) exp(-ikr_p \cos\theta \cos\theta_p) \, d\theta \qquad (4.52)$$

The longitudinal field along z-axis is given by

$$E_z = -ikf \int_{\alpha_0}^{\alpha_1} I_0(\theta) \frac{2sin^2\theta}{1+cos\theta} exp(-ikr_p \cos\theta) \, d\theta \qquad (4.53)$$

since $\theta_p = 0$ on z-axis.

By applying Equation (3.3) with constant $C = 1$ and gain function $\boldsymbol{G}_f = (3/2)\sin^2\theta'$ and assuming radiation angle from antenna to transmitting parabolic mirror θ' is the same as the illumination angle to focus from receiving parabolic mirror θ due to the structural symmetry, we get,

$$I_0(\theta) = \sqrt{(3/2)\sin^2\theta} \frac{\exp(-jk(r^{'}(1+\cos\theta)+rr))}{\mathbf{r}^{'}+rr}$$
$$= \sqrt{(3/2)\sin^2\theta} \frac{\exp(-jk((f/\cos^2(\theta))(1+\cos\theta)+rr))}{2f/(1+cos\theta)+rr} \tag{4.54}$$

where rr is distance between two parabolic mirrors and [67, p.897]

$$r^{'} = \frac{2f}{1+\cos\theta} = \frac{f}{\cos^2(\theta/2)} \tag{4.55}$$

Therefore, the longitudinal component along z-axis is given by,

$$E_z = -ikf \int_{\alpha_0}^{\alpha_1} \sqrt{(3/2)\sin^2\theta} \frac{\exp(-jk((f/cos^2(\theta))(1+\cos\theta)+rr))}{2f/(1+cos\theta)+rr} \frac{2sin^2\theta}{1+cos\theta} exp(-ikr_p\cos\theta)\,d\theta \tag{4.56}$$

By applying Equation (4.56), the axial lengths of spot size (FWHM) of longitudinal field intensity along z-axis according to different range of subtending angles are illustrated by numerical simulation in Fig 4.6.

(a)

(b)
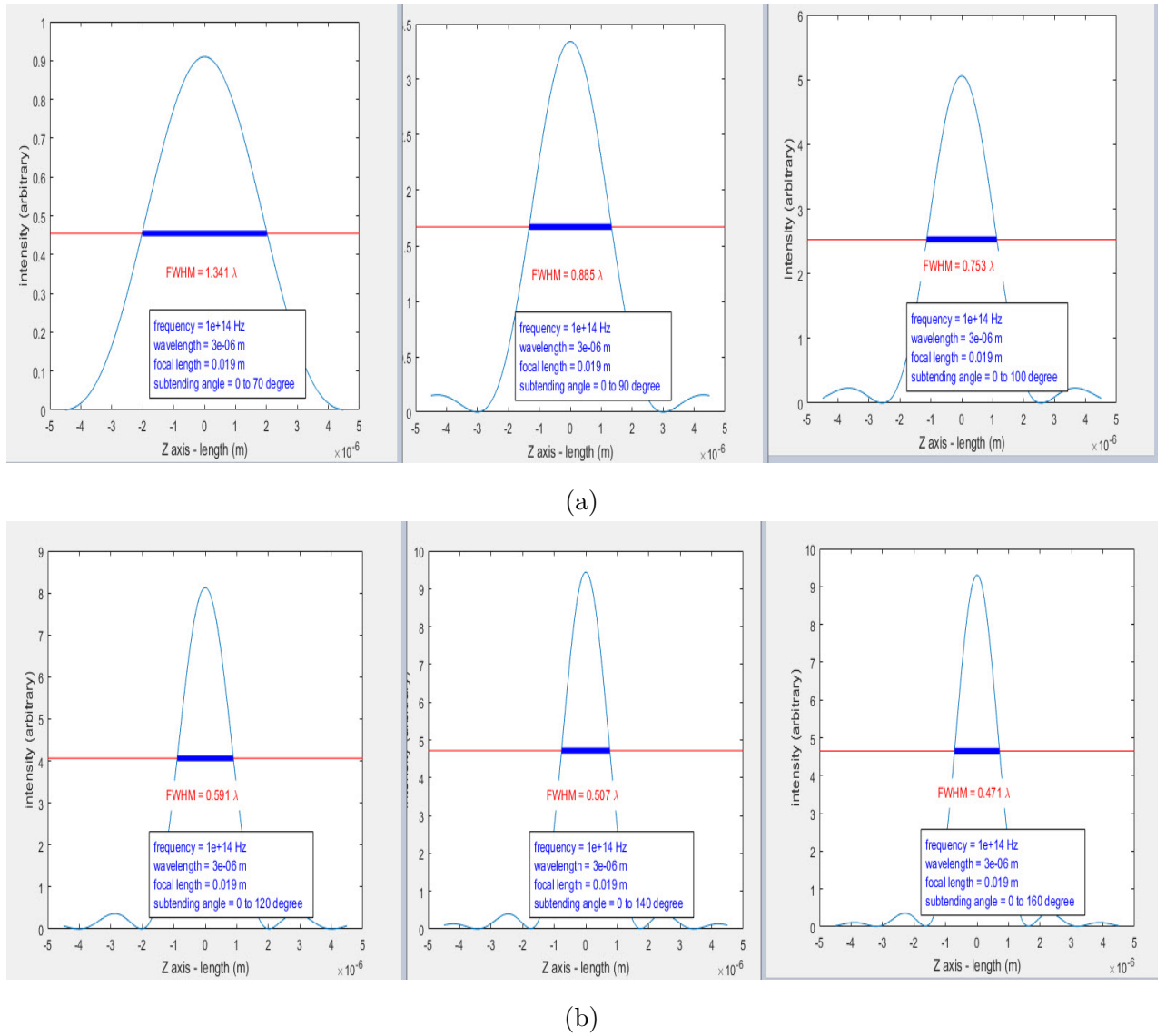
Figure 4.6: different lengths of spot size depending on range of integral angle

In Fig. 4.6, the range of integral angle varies from $10^0 - 70^0$ to $10^0 - 160^0$. The length of spot size in z direction varies from 1.341λ to 0.471λ. This ratio of length to wavelength is independent of the frequency as shown in Fig. 4.7
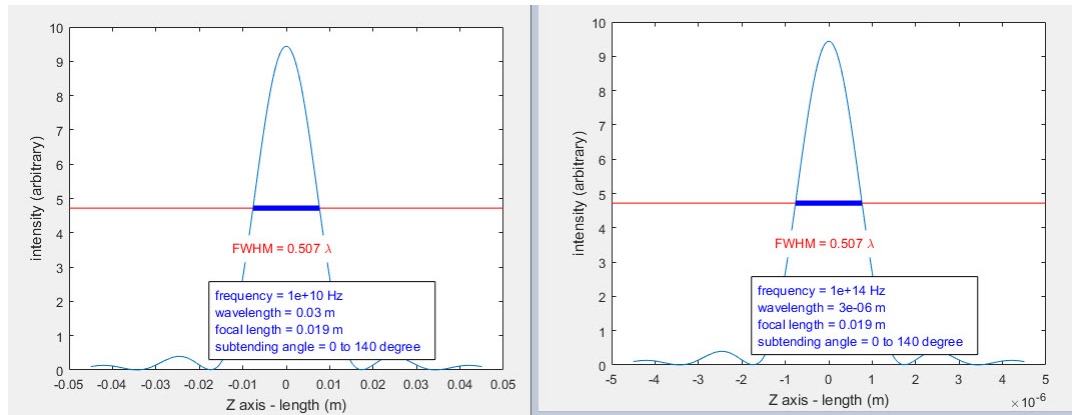
Figure 4.7: Lengths of different frequencies

If we let the solid angle (here in 2D since azimuthal symmetry is assumed) subtend the range from 1^0 to 180^0 , the ratio R of axial length to wavelength λ changes as shown in Fig. 4.8.
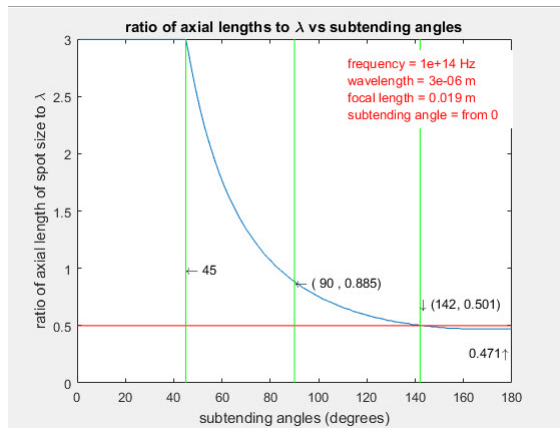
Figure 4.8: Ratio R vs subtending angle

The change of the Ratio R occurs from 45 degrees and forms a hyperbola-like curved line with maximum value 2.9770 at 45 degrees and minimum value 0.471 at 180 degrees. The half of λ appears at 142 degrees.

Below 45 degrees, focusing is so weak that the magnitude of longitudinal component is much smaller than that of radial component as shown in Fig. 4.9. and axial length exceeds the scope of graph (3λ).
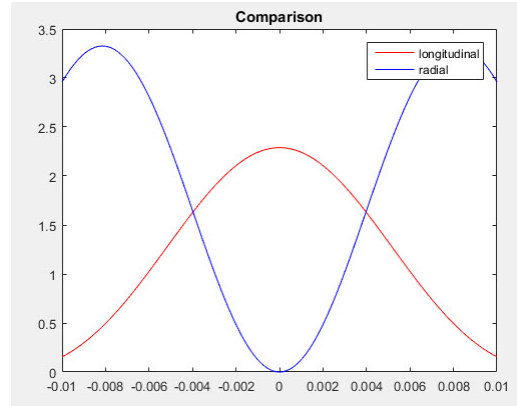
Figure 4.9: fields of weak focusing

This interesting subtending-angle-dependent-R phenomena are ascribed to the last exponential part of Equation (4.56), i.e., $exp(-ikr_p \cos\theta)$. The simulation only with this part (without other parts associated with the magnitude of field distribution) shows the same phenomena (Fig. 4.10).
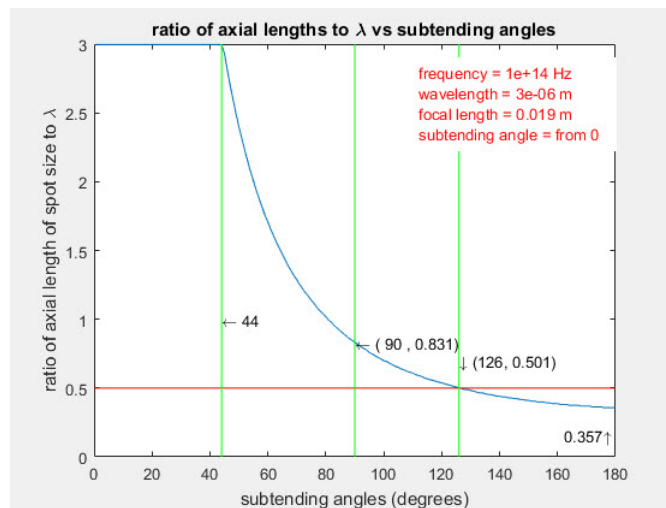
Figure 4.10: relation only with basic terms

Compared with Fig. 4.8, Fig. 4.10 shows the similar curve with slightly reduced values.

It is different from the spot size on the focal plane (XY plane).

For the spot size on the focal plane, which has no exponential part due to $\theta_p = \pi/2$ in Equation (2.33), there are only ignorable differences in diameters of spot sizes between different subtending angles (e.g., 0.46795λ for subtending angle range $0 - 80$ degrees, while 0.42255λ for $0 - 142$ degrees).

4.6.3 Uncertainty-principle-like relation

The product of ratio R of axial lengths to wavelength and subtending angles Ω are not a fixed constant rather a varying value approximately between minimum 70 and maximum 135 as shown in Fig. 4.11.
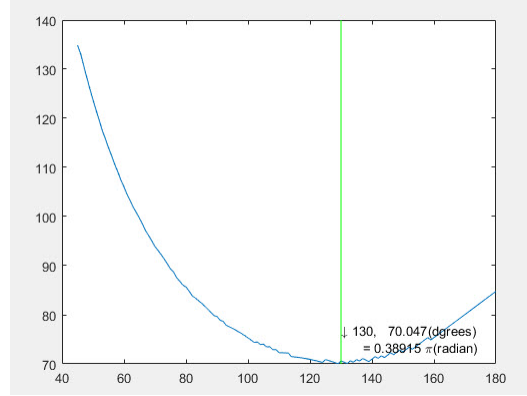
Figure 4.11: Uncertainty-like relation of product of ratio R and subtending angle Ω

The product of the ratio R and subtending angles Ω produced by basic (exponential) part is shown in Fig. 4.12.
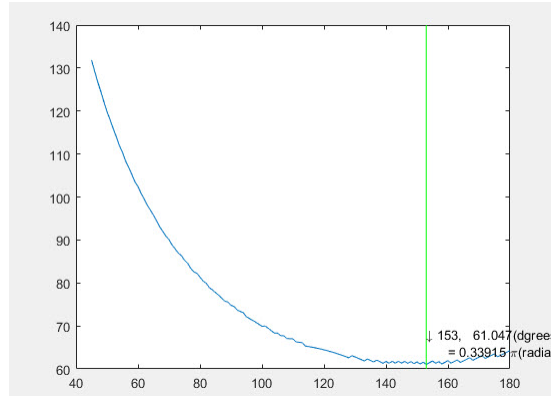
Figure 4.12: Uncertainty based on basic part

The values of the product may be expressed,

$$\triangle_R \triangle_\Omega \geq 70 \tag{4.57}$$

In radian scale approximately,

$$\triangle_R \triangle_\Omega \geq \frac{2}{5}\pi \tag{4.58}$$

This interesting phenomena based on $exp(-ikr_p \cos\theta)$ looks like the uncertainty characteristic of wave functions $\psi(x) = \exp(-ikx)$ such as the uncertainty principle of Fourier transform of Gaussian wavepacket

$$\sigma_x \sigma_k = \frac{1}{2} \tag{4.59}$$

However, R represents the full width of half maximum (FWHM) of the intensity of the longitudinal component calculated by Equation (4.56) and hence the relation between the ratio and the subtending angles in the sense of uncertainty principle is not straightforward and needs more rigorous analysis in the future work.

As for the direction of the longitudinal component, it may be explained as follows. When range of subtending angle is, for example, $10^0 - 142^0$ degrees, waves coming with angle $10^0 - 90^0$ create the longitudinal component propagating in the forward direction and waves coming with angle $90^0 - 142^0$ create the longitudinal component propagating in the backward direction. By superposing both longitudinal components, some portions are canceled which also leads to the reduction of the length of the spot size.
The length of the spot size of the longitudinal component along the propagation axis is the region of interaction.
If the length reduces to around the half of the wavelength where the integral range is $10^0 - 142^0$ as shown in Fig. 4.8, then one kick acceleration can occur as explained in the following subsections.

4.6.4 Acceleration through ultratight focusing

In ultratight focusing, the accelerating phase of the beam will dominate half the spot size for half the period of the wave first and then decelerating phase will take over for another half period. If the particle in accelerating phase escapes the region before decelerating phase comes, then the particle will keep the energy gain.

4.6.5 Threshold values

Consider that a particle with velocity v_0 positioned at the center of the axial spot size with axial length of half wavelength is pushed by the accelerating phase of the field and escapes the interaction region by moving over the half length of the spot size (a quarter wavelength) during the time interval of half period.
The final velocity is

$$v_f = v_0 + v_{ad} \tag{4.60}$$

where v_{ad} is the velocity added through acceleration. We make an approximation of the average velocity by

$$v_{av} = v_0 + (1/2)v_{ad} \tag{4.61}$$

The particle should get out of a quarter of wavelength (half the axial spot size) with average velocity within a half period.

$$\frac{1}{4}\lambda = v_{av}\frac{T}{2} = v_{av}\frac{1}{2f} \tag{4.62}$$

which means $v_{av} = c/2$. The minimum energy gain is

$$\mathcal{E}_{gain} = mc^2(\gamma_f - 1) - mc^2(\gamma_i - 1) = mc^2(\gamma_f - \gamma_i) \tag{4.63}$$

where $\gamma_i = 1/\sqrt{1 - (v_0/c)^2}$ and $\gamma_f = 1/\sqrt{1 - (v_{av}/c)^2} = 1/\sqrt{1 - ((v_0 + (1/2)v_{ad})/c)^2}$.

By equating this energy gain with energy transfer

$$\mathcal{E} = qEL \tag{4.64}$$

where L is interaction length, the electric field corresponding to this energy gain through the distance $(1/4)\lambda$ is

$$E = \frac{\mathcal{E}}{(1/4)q\lambda} \tag{4.65}$$

The crucial point here is the phase, not the magnitude and hence, in case of pulsed beam, the wavelength and the period are decided by the carrier wave, while magnitude is decided by the pulse.

1) If the initial velocity of the particle is $(1/4)c$, then from Equation (4.61), (4.62), the minimum average velocity is $v_{av} = c/2$ and, from Equation (4.63), minimum energy gain is

$$
\begin{aligned}
\mathcal{E}_{gain} &= mc^2(\gamma_f - \gamma_i) \\
&= mc^2(\frac{2}{\sqrt{3}} - \frac{4}{\sqrt{15}}) \\
&= 0.1219mc^2 \\
&= 9.9836 \times 10^{-15} \\
&\sim 1 \times 10^{-14}
\end{aligned}
\tag{4.66}
$$

This energy gain is equivalent to 60 KeV. From Equation (4.65), the necessary electric field for the wave of frequency 10GHz is 8.3 MV/m which is achievable. In this case, this is the threshold electric field.

2) However, if the particle is initially at rest ($v_0 = 0$), then the final velocity should be c since average of added velocity should be $c/2$ ($v_{ad}/2 = c/2$) and hence acceleration is not realizable. But, If the approximation of average velocity is different from the above assumption, the result would be also different.

3) If the initial velocity of the particle is equal to or greater than $c/2$, then since $v_{ad} > 0$, average velocity is

$$v_{av} = v_0 + (1/2)v_{ad} = c/2 + (1/2)v_{ad} > c/2 \tag{4.67}$$

which means average velocity is always greater than initial velocity

$$v_{av} > v_0 \tag{4.68}$$

and hence

$$\gamma_f > \gamma_i \tag{4.69}$$

Accordingly energy gain is always greater than zero

$$\mathcal{E}_{gain} = mc^2(\gamma_f - \gamma_i) > 0 \tag{4.70}$$

which means that there is no threshold magnitude of electric field and all the input energy will be transferred to the particle.

This ultratight focusing acceleration occurs for any subtending angles insofar as the needed average velocity of particle is greater than c/2.
The relation between energy gain and ratio (R) of axial length to wavelength is illustrated in Fig. 4.13.
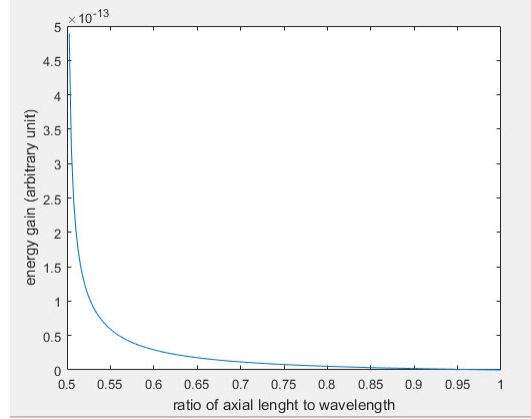
Figure 4.13: Relation between energy gain and R

4.6.6 Superluminal phase velocity and synchronization

It is well known that the phase velocity of the waves in the focal region is superluminal and hence synchronization between velocity of particle and phase velocity of the waves is crucial in particle acceleration through laser. However, in the ultratight focusing acceleration scheme, the slippage is considered intrinsic and the scheme is focused only on the temporal factor during which the particle gets out of the interaction region while it faces the accelerating phase of the waves.

4.6.7 Comparison

It is of interest to compare the energy gain through this ultratight focusing acceleration with that through some recently developed acceleration schemes.
Among them, plasma wakefield accelerator, dielectric laser accelerator and direct (vacuum) laser accelerator attract a lot of attention. The common goal is the achievement of extremely high accelerating gradient. Since they adopt fundamentally different schemes and ultratight focusing acceleration can be categorized into vacuum acceleration, the comparison will be done with other scheme of vacuum acceleration i.e., sub-cycle accelerator. In sub-cycle acceleration scheme, the particle gets energy of the level GeV from the beam if the particle is relativistic and the field intensity is ultrahigh.
For convenience, we divide the cases into two categories i.e., relativistic regime and nonrelativistic regime.

4.6.7.1   Relativistic regime

In relativistic regime, the velocity of the particle is close to c. Therefore, for the comparison, we consider the energy gain of ultratight focusing acceleration where the initial velocity of particle is greater than $c/2$, which includes the relativistic velocity.

The field intensity of input energy $\mathcal{E}_i$ with pulse duration time of a period T at focal spot size of which diameter is half a wavelength is given by,

$$I = \frac{\mathcal{E}_i}{T\pi(\lambda/4)^2} = \frac{E^2}{2\eta_0} \tag{4.71}$$

and the electric field is,

$$E = \sqrt{2\eta_0 \frac{\mathcal{E}_i f}{\pi(\lambda/4)^2}} \tag{4.72}$$

The energy gain of the particle moving through electric field at focal region for distance $\lambda/4$ is

$$
\begin{aligned}
\mathcal{E}_g &= qE\ell \\
&= qE\frac{1}{4}\lambda \\
&= q\sqrt{2\eta_0 \frac{\mathcal{E}_i f}{\pi(\lambda/4)^2}}\frac{1}{4}\lambda \\
&\simeq 15.5q\sqrt{\mathcal{E}_i f}
\end{aligned} \tag{4.73}
$$

which means that energy gain is dependent on input energy and wave frequency. Fig. 4.14 shows the relation of energy gain vs input energy and frequency.
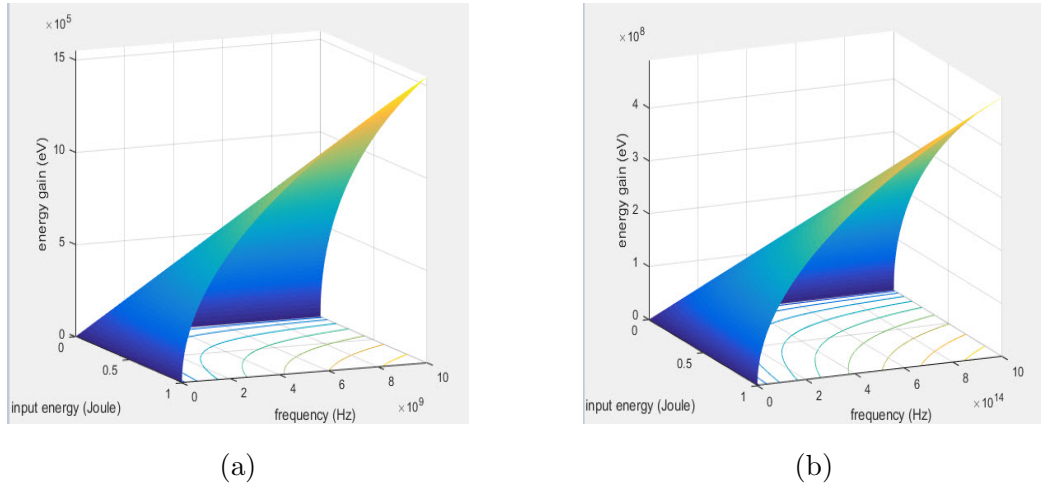

Figure 4.14: energy gain vs input energy and frequency

In Fig. 4.14(a), maximum frequency of the accelerating wave is 10GHz and maximum energy gain is 1.5MeV. In Fig. 4.14(b), maximum frequency is 1PHz and maximum energy gain is 0.49GeV. Maximum input energy is 1J for both cases.

In sub-cycle acceleration scheme using relativistic electron and ultrahigh intensities, it is illustrated[29] that for carrier wavelength $\lambda = 0.8\mu m$ (frequency $f = 0.375PHz$), pulse duration time $T = 2.67fs$, beam waist at focus $\rho = 10\mu m$ and intensity $I = 10^{22}W/cm^2$, energy gain is GeV level for optimized carrier phase. We assume the input laser energy here is 0.8J ($\mathcal{E} = 10^4 IT\pi\rho^2$).

If the same input energy and frequency are used in ultratight focusing acceleration, the energy gain will be $0.027GeV$ ($15.5\sqrt{\mathcal{E}_i f}$), which shows that the energy gain is lower than that of sub-cycle acceleration by 2 or higher orders of magnitude.

However, in sub-cycle acceleration, there is only small energy gain with weak field intensity below threshold, while, in ultratight focusing acceleration, any considerably high field intensity gives rise to greater energy gain.

For example, for input energy $\mathcal{E}_i = 1mJ$ and wavelength $\lambda = 1.8\mu m$, energy gain in sub-cycle acceleration scheme is around $23keV$ [82], while energy gain in ultratight focusing acceleration system is $63keV$ ($15.5\sqrt{10^{-3}(c/(1.8 \times 10^{-6}))}$).

4.6.7.2 Non-relativistic regime

In sub-cycle acceleration scheme, the velocity of the particle should be relativistic and non-relativistic particle can get the energy gain only through ponderomotive force. However, in ultratight focusing acceleration regime, the particle can get energy gain if the initial velocity is non-zero and field is high enough to create the average velocity greater than c/2.

For example, for the case where initial velocity is 0.39c, wavelength 800nm (frequency 0.375PHz), pulse repetition rate 3kHz, average power 2.4W, peak power 90GW, and beam waist $1.2\mu m$, in sub-cycle regime, the experimental report shows the energy gain is 12KeV [87], and the electric field is assumed to be 3.9×10^{12} V/m.

$$E = \sqrt{2\eta \times 90 \times 10^9/(\pi \times (1.2 \times 10^{-6})^2)}$$
$$= 3.8730 \times 10^{12} \tag{4.74}$$

In ultratight focusing acceleration, with the same initial velocity and frequency, minimum energy gain is,

$$\mathcal{E} = mc^2(\gamma_f - \gamma_i)$$
$$= mc^2\left(\frac{1}{\sqrt{1 - ((c/2)/c)^2}} - \frac{1}{\sqrt{1 - (0.39c/c)^2}}\right)$$
$$= mc^2\left(\frac{2}{\sqrt{3}} - 1.086\right) \tag{4.75}$$
$$= 5.6270 \times 10^{-15}$$

which is equivalent to 35keV. Minimum electric field needed is $1.76 \times 10^{11}V/m$

$$E = \frac{\mathcal{E}}{q\lambda/4}$$
$$= 1.76 \times 10^{11} \tag{4.76}$$

4.6.7.3 Summary

The characteristics of ultratight focusing acceleration scheme compared with sub-cycle acceleration scheme are as follows.

In sub-cycle acceleration scheme, relativistic particle and ultrahigh field intensity of laser are always necessary. However, in ultratight focusing acceleration scheme,

- if initial velocity of particle is non-zero, then input energy greater than threshold value, that exceeds the value needed to create average velocity which is equal to or greater than $c/2$, is transferred to the particle

- if initial velocity is equal to or greater than $c/2$, then all the input energy is transferred to the particle

- not only laser but also microwave can create appreciable acceleration since only the ratios are critical in this scheme i.e., the ratio of z-axial spot size to wavelength as interaction region and half the period as interaction time duration regardless of frequencies.

- there are no relativistic limitations

- only in the theoretical extreme case, ultratight focusing scheme is inferior to sub-cycle scheme

4.6.8 Geometric structure

This extra large range of integral angle can be provided only by the deep parabolic reflector which has a focal point deep inside the aperture. Here, we have to be careful not to have breakdown. The diagram of parabolic mirror for subtending angle 140 degrees is shown in Fig. 4.15.
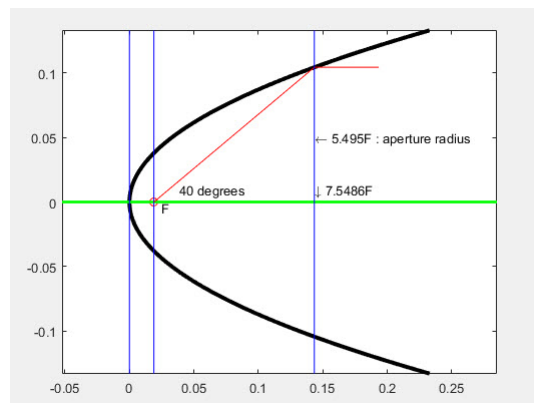
Figure 4.15: Diagram of parabolic mirror for subtending angle 140 degrees

4.7 Conclusion

The differences between direct microwave acceleration and direct laser acceleration resides in the differences of their scale and power intensity.

In the nonrelativistic ponderomotive acceleration scheme, the difference of magnitude of power intensity may be canceled by the difference of frequencies and hence there is no fundamental differences between microwave and laser regimes. However, the longer interaction range and the longer period of the microwave may provide easier manipulation of physical structure. Additionally, the larger scale of the area of longitudinal component may provide the greater number of accelerated particles than in laser case, which can be exploited for enhancement of number of events in collision physics.
The big disadvantage of the ponderomotive acceleration is its low energy transfer. Therefore, the nonrelativistic ponderomotive acceleration is not useful except for any special case where the physical size matters.

In relativistic acceleration of sub-cycle mode, the threshold power intensity corresponding to the normalized parameter $a_0 > 1$ which is $10^{20} W/cm^2$ [29] can not be achieved with microwaves.

However, in microwave regime, the relativistic normalized parameter a_0 which is greater than unity can be achieved with much lower power than in laser case and this lower power of microwave is achievable.
The most interesting feature of parabolic mirror arises when illuminating beam is ultra-tightly focused. When parabolic reflector is illuminated by radially polarized beam with the ultratight-focusing angle (i.e., when the highest integral angle exceeds $\pi/2$), the axial length of focal spot size can reduce to half a wavelength and one-kick acceleration with much lower power intensity is expected. The threshold quantity is minimum average velocity of the particle which is equal to or greater than c/2. If initial velocity of particle is non-zero, then there is energy gain with input energy greater than threshold. If initial velocity is greater than c/2, then any input energy will be transferred to the energy gain.

Chapter 5

Quasi Bessel beam

5.1 Introduction

The structure used in this work can be employed to generate the radially polarized quasi Bessel beam. The original Bessel beam includes the axis symmetric propagation-independent Bessel function and hence is diffraction-free and self-reproducing. The non-diffraction property comes from this propagation-independent character of Bessel function and the self-healing effect is understood through the symmetric character of the beam or through the Babinet's principle[105].
However, the ideal Bessel beam requires infinite energy and hence is physically not realizable. The approximate beam of Bessel is only realizable with certain kinds of circularly symmetric apertures which truncate the beam for finite widths. This apertures cause the diffraction of the beam which is, however, much smaller than in the ordinary case. This diffraction resistant beam is termed as 'quasi Bessel beam', 'localized beam' or 'Bessel-Gauss beam'. We will describe the possible interesting applications of the parabolic open cavity structure to create the quasi Bessel beam after short introduction of Bessel beam and quasi Bessel beam.

5.2 Bessel beam

5.2.1 Origin

As mentioned above, a Bessel beam is a field whose amplitude is described by a Bessel function of the first kind [106]. Accordingly, the Bessel beam can be produced by the cylindrically symmetric field.

Bessel beam (practically quasi Bessel beam) has received an increasing interest due to its non-diffracting (practically nearly diffracting) character. Particularly, ultrashort-pulsed Bessel beam is often referred to as "needle beams" [107]. Quasi Bessel beams can be useful in various applications due to its nondiffracting character. Some of these applications are optical tweezers [108], optical microscopy [109], [110], [111], high-resolution optical coherence tomography [112] and laser micromachining [113], [114].

The non-diffracting property of the zeroth order Bessel beam as a solution of the Helmholtz equation was first realized by Durnin in 1987 [115].

The scalar wave equation is

$$(\nabla^2 - \frac{1}{c^2}\frac{\partial^2}{\partial t^2})E(\mathbf{r}, \mathbf{t}) = \mathbf{0} \tag{5.1}$$

Its spatial part is the Helmholtz equation

$$(\nabla^2 + k^2)E(\mathbf{r}) = \mathbf{0} \tag{5.2}$$

In cylindrical coordinates (ρ, ϕ, z), the Helmloltz equation becomes

$$(\frac{\partial^2}{\partial\rho^2} + \frac{1}{\rho}\frac{\partial}{\partial\rho} + \frac{1}{\rho^2}\frac{\partial^2}{\partial\phi^2} + \frac{\partial^2}{\partial z^2} + k^2)E(\rho, z) \tag{5.3}$$

We assume scalar fields propagating into the source-free region $z \geq 0$. One of the exact solution is plane wave solution which is transverse-independent,

$$E(\rho, z) = E_0 exp(-ik_0 z) \tag{5.4}$$

where $\rho = \sqrt{x^2 + y^2}$, E_0 is constant and k_0 constant wave vector. Another solution is produced by decomposing the wave vector into directional components,

$$
\begin{aligned}
E(\rho, z) &= exp(-i\beta z)\int_0^{2\pi} A(\phi)exp(i\alpha\rho)d\phi \\
&= exp(-i\beta z)\int_0^{2\pi} A(\phi)exp[i\alpha(x\cos\phi + y\sin\phi)]d\phi
\end{aligned}
\tag{5.5}
$$

where $\alpha = k_\rho = \sqrt{k^2 - \beta^2}$, $\beta = k_z$, $k^2 = \alpha^2 + \beta^2$.

Since $x = \rho\cos\vartheta$ and $y = \rho\sin\vartheta$ where $\vartheta = \pi/2 - \phi$, and hence $x\cos\phi + y\sin\phi = \rho(\cos\vartheta\cos\phi + \sin\vartheta\sin\phi) = \rho\cos(\phi - \vartheta)$,

by using the identity with $n = 0$,

$$\int_0^{2\pi} \cos n\phi \, exp(ic\cos(\phi - \vartheta))d\phi = 2\pi i^n J_n(c)\cos n\vartheta \tag{5.6}$$

where $J_n(c)$ is the n-th order Bessel function of the first kind, and using the axial symmetry for $A(\phi)$,

Equation (5.5) becomes

$$
\begin{aligned}
E(\rho, z) &= A_0 exp(-i\beta z)\int_0^{2\pi} exp[i\alpha\rho\cos(\phi - \vartheta)]\frac{d\phi}{2\pi} \\
&= A_0 exp(-i\beta z)J_0(\alpha\rho)
\end{aligned}
\tag{5.7}
$$

where $k^2 = \alpha^2 + \beta^2 = (\omega/c)^2$, $\alpha = k_\rho$, $\beta = k_z$

Including the temporal part, the complete solution is

$$E(\rho, z, t) = A_0 exp(-i\beta z - \omega t)J_0(\alpha\rho) \tag{5.8}$$

This is a Bessel beam solution.

5.2.2 Non-diffracting property

When β is real, the time averaged intensity distribution is the same for $z = 0$ and $z > 0$,

$$\begin{aligned}
I(\rho, z > 0) &= 1/2|E(\rho, z)|^2 \\
&= I(\rho, z = 0)
\end{aligned} \tag{5.9}$$

which implies that the fields are non-diffracting.

From Equation (5.4), (5.9), we can see that the intensities of plane wave and the Bessel beam are constant while propagating, since, when absolute squared, the exponential phase part including t and z disappears and the only contribution comes from the squared Bessel part J_0^2. Those equations only tell the field intensity profile of transverse components. We understand these waves require infinite energy to keep the intensity unchanged while traveling.

5.2.3 Self-healing property

The reconstructing ability of a non-diffracting beam when disturbed by an obstacle is called 'self-healing' or 'self-reconstructing' property. This phenomenon is explained with Barbinet's principle [105] which says that the sum of the wave transmitted through a screen plus the wave transmitted through the complementary screen is the same as if no screen were present. This property of Bessel beam finds the application in high resolution large depth tomography (Section 5.6.2)

5.3 Quasi Bessel beam

When we look into the properties of the Bessel function of ideal Bessel beam, it is clear that the Bessel function provides the transverse intensity distribution of the field which has the structure of infinite number of rings. The intensity attenuates starting from the maxima at the central core on the propagating axis. However, the power is equally distributed across the whole transverse structure[116], [117], which implies that the ideal Bessel beams , as already mentioned above, require infinite power just like plane waves and hence cannot be realizable.

For the actual realization of the Bessel beam, we need to create such a beam over a finite area truncated by a finite aperture. Durnin used the Rayleigh-Sommerfeld Green's function to find the Bessel beam with a finite area which is well known in diffraction theory under the assumption that the wavelength is small compared with the size of the aperture and the propagation angles are not too steep[115].

Several ways to create the quasi Bessel beam have been proposed and realized. The most commonly practiced tool is an axicon lens as shown in Fig. 5.1, which was first proposed by Herman and Wiggins [118].
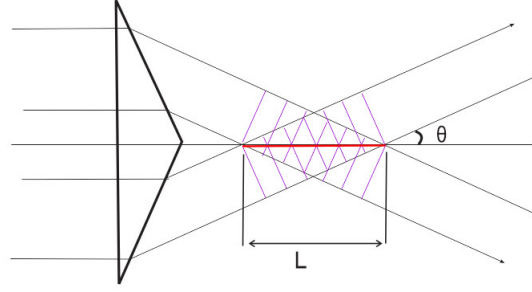
Figure 5.1: Diagram of axicon generating quasi Bessel beam

The quasi Bessel beam created by axicon lens is only an approximation to the Bessel beam over a limited propagation range L in Fig. 5.1.

The mathematical analysis of the quasi Bessel beam generated by an axicon is usually derived from the Fresnel diffraction integral which gives only a good approximation in the area close to the beam axis.

The incident beam can have several types. Gori et al. suggested to use Gaussian envelope to truncate the infinite transverse expansion of the Bessel beam and called it as Bessel-Gauss beam [119].

For the propagating plane waves, the scalar paraxial Helmholtz equation is commonly used

$$(\nabla_\perp^2 + 2jk\frac{\partial}{\partial z})\psi = 0 \tag{5.10}$$

One of the solutions is Gaussian beam,

$$\psi(\rho, z) = \psi_0 exp(-\rho^2/w_0^2) \tag{5.11}$$

It is reasonable to use the Gauss beam to truncate the propagating Bessel beam (Bessel-Gauss beam) which is also a solution of equation (5.10),

Let us assume the circularly symmetric disturbance of a monochromatic wave across the plane at $z = 0$,

$$\psi(\rho, 0) = A_0 exp(-\rho^2/w_0^2)J_0(\alpha\rho) \tag{5.12}$$

where A_0 is initial amplitude, ρ radial distance on the plane, w_0 beam waist, J_0 zero order Bessel function of the first kind and α radial component of wave vector. The exponential part is the Gaussian term and the other part is the Bessel function part. The Equation (5.12) shows only the transverse field profile and gives no information how this profile changes at a propagation of a certain distance.

The other type of the incident beam can be Laguerre-Gaussian beam. Since Laguerre-Gaussian beam has the orbital angular momentum which is conserved, the created beam is high order Bessel-like beam, which has hollow center [120],[121].

The radial polarization of the incident beam is naturally compatible with azimuthal symmetry of the Bessel beam.

The electric field derived from transverse component of wave vector is longitudinal which can be exploited for the particle acceleration [122],[123]. The transverse component of the Bessel-like beam created by the axicon has been investigated by [124].

The fundamental character of the quasi Bessel beam is based on the causticality of the beams in a broader sense.

5.4 Superluminality

The phase velocity of the quasi Bessel beam is superluminal due to the geometric relation between wavevector propagation and the propagation of the wave plane on the axis as in the case of beam focus. The phase velocity can be expressed as $c/\cos\alpha$. The signal velocity looks like also superluminal, violating the special relativity [125]. However, the signal velocity is subluminal [126], [127] as $v_s \sim c\cos\alpha/(1+\sin\alpha)$ [128]. The superluminal phase velocity affects the acceleration design due to the phase matching problem between beams and the particle.

5.5 Causticality - general anlysis

In optics, the caustic is a curve or surface to which each of the light rays is tangent. The term "caustic" originates from the diminutive form of the Greek word for "burning iron"[129].

Recently, it has been suggested to generalize the concept of the caustic to include broader form of crossing of two or more rays at each point in space with non-diffracting property [130]. Non-diffracting beams such as Airy beam or Bessel-like beam belong to the caustic. Bessel-like beams can be interpreted as the limiting case of a caustical beam with a narrow angular spectrum, radial symmetry and infinite curvature [130].

If we generalize the concept of "caustic" still more, any kind of focusing can be categorized into the caustic.

In other words, optical focus of electromagnetic waves, Bessel beam and Airy beam may all belong to the same category i.e., focus. Focus appears where the waves are collected into and cross at a point. The focusing is limited at a point for a point focus, extended along a line for line focus, extended along a curve for a Airy beam. The quasi Bessel beam can also be considered as a line focus because an axicon concentrates the radially polarized beam in a finite length of distance which may be called line focus [118]. As for line focus. quasi Bessel beam may be referred to as a temporal line focus while focus of cylindrical wave as a spatial line focus. The cone of Cherenkov radiation may be another example of temporal line focus. X-waves [131] are special superpositions of Bessel beams.

Mathieu beams[132] and parabolic (Weber) beams[133] are other type of Bessel beams with different transverse structures and hence expressed in different coordinates i.e., Mathieu beam in elliptical coordinates and Weber beam in parabolic coordinates.

Temporal line caustic beams have the non-diffractive and self-healing properties. Additionally, temporal curved line caustic beams have acceleration property.

(a) Bessel beam

(b) Airy beam

(c) Cherenkov radiation

(d) point focus

(e) line focus of off-focus illumination
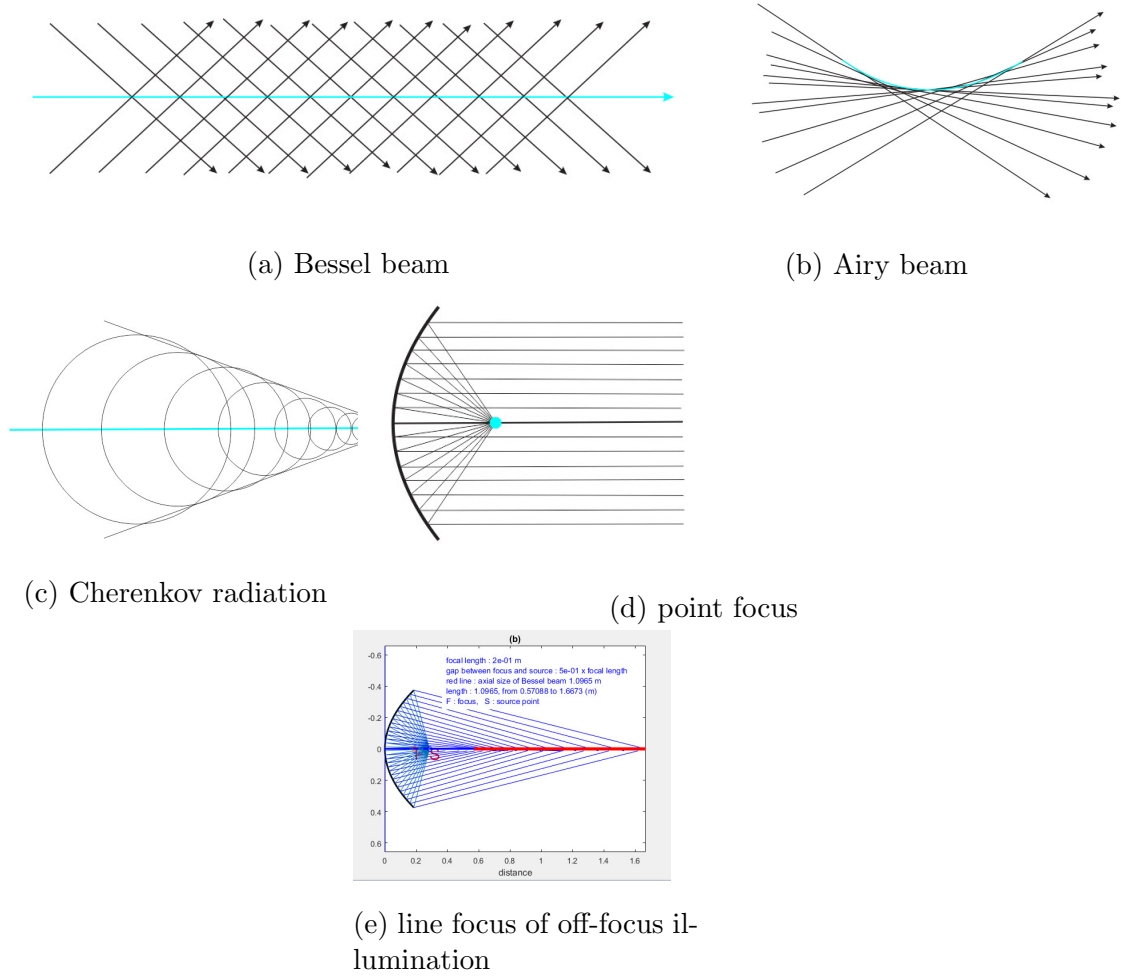
Figure 5.2: types of caustic phenomena

Recently hybrids between non-accelerating (Bessel beam) and accelerating (Airy beam) optical waves which have arbitrary trajectories in free space and share diffraction-resisting and self-healing properties are proposed [134].

Some authors consider the non-diffracting beams as the superpositions of multiples of plane waves, all having the same axial wavevector and put them mathematically into a Whittaker integral [135, section 3 by M. Mazilu and K. Dholakia]

$$u(x,y,z) = exp(-ik_z z) \int_0^{2\pi} d\phi g(\phi) exp(-k_t(x\cos(\phi) + y\sin(\phi))) \qquad (5.13)$$

where $u(x,y,z)$ is plane wave solution of the scalar Helmholtz equation, k_z axial wavevector component, k_t the transversal wavevector, ϕ the angle of the plane wave around the propagation axis z and the complex function $g(\phi)$ the phases and amplitude of the different plane waves.

Complex function $g(\phi)$ represents the vaious kind of non-diffracting beams. For the zeroth order Bessel beam, $g(\phi) = 1$, for higher order Bessel beam, $g(\phi) = exp(i\updownarrow\phi = \cos(\updownarrow\phi) + i\sin(\updownarrow\phi)$, for higher order Mathieu beam, $g(\phi) = C(\updownarrow, q, \phi) + iS(\updownarrow, q, \phi)$,

Classically, in the focus, electromagnetic waves just pass by without any interaction between them. All the phenomena of focus appear through the interaction with material positioned at the focus.

All the caustics are the results of the ways of illumination. They reflect all the characteristics of the source waves.

5.6   Applications

The applicability of quasi Bessel beam is ever increasing. Some have been just mentioned item-wise in section 5.2.1 . A detailed discussion of the applications is beyond the scope of this work but may be found elsewhere [135, section 3] . We will just mention the main applications briefly to the extent that one can see why the quasi-Bessel beam attracts interests.

5.6.1   Microscopy with self-reconstructing beams

The self-healing property of Bessel beam, which provides the recovery of its initial intensity profile after being obscured by a single obstacle, has been exploited in optical microscopy to get a simultaneous increase of image quality and penetration depth in dense media [109].

5.6.2   High resolution large depth tomography

The length of Bessel beam created by an axicon provides a large depth range without losing high lateral resolution in tomography[112].

5.6.3   Micro-manipulation

A technique for optical manipulation (alignment, building stacks) of micron-sized particles, including biological samples, using a zeroth-order Bessel light beam has been demonstrated [108].

5.6.4   Micro-processing

The Bessel beam possesses both a micron-sized focal spot and a deep focal depth and is suitable for laser micro-fabrication. A small crossing angle Bessel beam can drill a deep hole with a small threshold fluence. A through-hole with a diameter smaller than $10\mu m$ can be made on a stainless steel sheet $20\mu m$ thick by using a Bessel beam with a large crossing angle[114].

5.6.5   Particle acceleration

The acceleration based on Bessel beam was introduced by [123] through using the inverse Cherenkov effect. The Cherenkov effect denotes that a particle traveling through a medium of refractive index n will emit a cone of light if its velocity is greater than c/n, c being speed of light. The inverse Cherenkov effect is its converse, namely, a cone of radially polarized laser beam directed on a particle by an axial prism such as an axicon can accelerate the particle. Here, the cone of radially polarized beam creates the quasi Bessel beam on the axis. The principle of inverse Cerenkov accelerator was demonstrated over a few keV. The

disadvantage of this accelerator is that particles collide with the medium gases resulting in material breakdown [87]. Recently a different model of the Bessel accelerator is proposed [136]. A Bessel beam is truncated by a set of annular slits, which makes several regions of strong and weak fields alternatively in its travelling path. Particles get strong acceleration while passing the strong field region and get weak deceleration while passing the weak field region, resulting strong net acceleration.

5.6.6 Long range communication

Free-space optics for data transmission has the potential to produce a very high capacity, secure, and robust communication method [137],[138]. Gaussian beams suffer from diffraction and atmospheric turbulence effects. A non-diffracting self-healing Bessel beam could potentially mitigate these problems [139].

5.7 Quasi Bessel beam with parabolic mirror

5.7.1 Configuration

Three possible different configurations for generation of quasi Bessel beam using radially polarized beams are shown in Fig. 5.3.

The spherical waves radiated by the monopole antenna are transformed into collimated and radially polarized plane waves by the reflection of the mirror 1. These radially polarized plane waves may create the quasi Bessel beam through reflection by another mirrors such as an axicon mirror or two (primary and secondary) parabolic mirrors.

Referring to Fig.5.3, in (a), the secondary mirror is put at the confocal position with the primary mirror, which creates only a plane wave beam, in (b), an axicon reflector is used instead of the primary parabolic mirror, which creates a quasi Bessel beam, and in (c), the secondary mirror is positioned such that there is a small gap between the focuses of primary and secondary mirrors, which creates the quasi Bessel beam explained below.
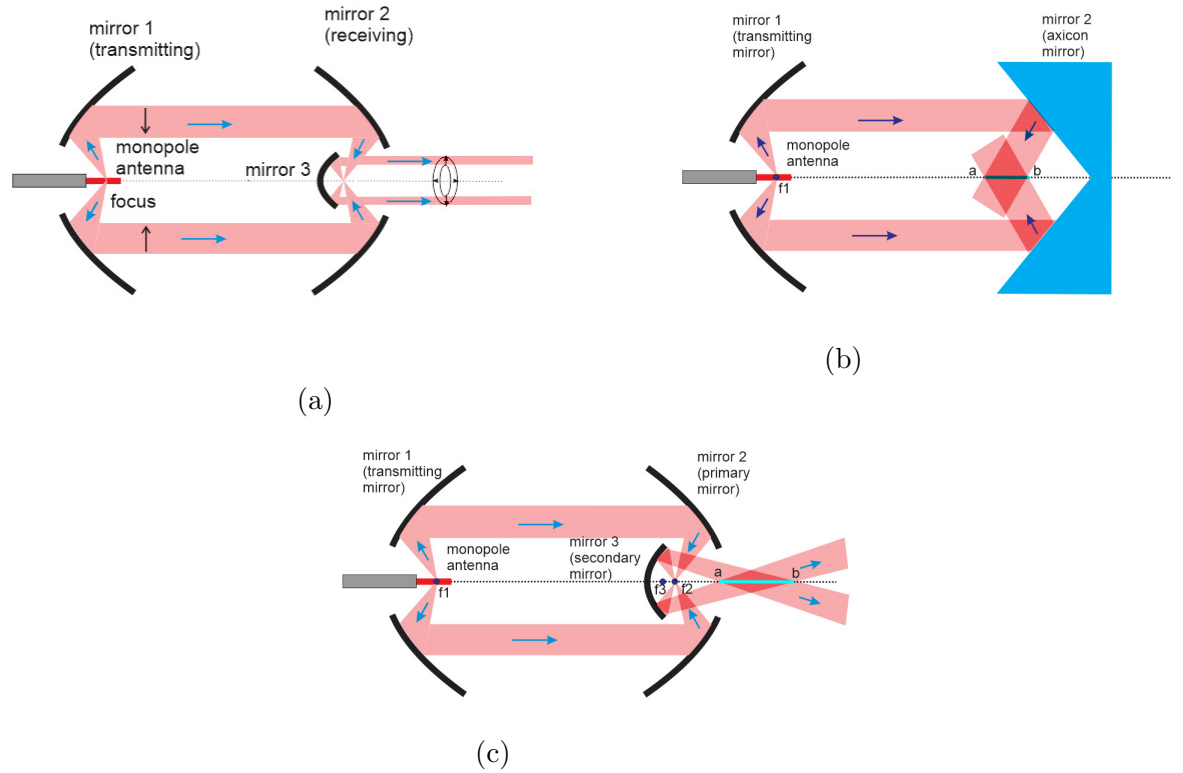
Figure 5.3: Schematics of Bessel beam

In Fig. 5.3(a), the waves reflected from the mirror 3 (secondary mirror) propagate through the center hole of mirror 2 (primary mirror) as a beam while spreading by diffraction. The fields free center line of the radially polarized beam will disappear due to the diffraction, but the interference and the superposition between diffracting waves on the axial line would be very tiny. In (b), the quasi Bessel beam is created by axicon mirror and this kind of quasi Bessel beam has been investigated in great details by several authors [140], [141]

The configuration of (c) produces an interesting feature to create quasi Bessel beam. The quasi Bessel beam is generated by the illumination of point source of waves at the on-axis position near focus of a parabolic mirror (secondary mirror). The focusing with near-focus source of reflector antenna is an axial defocusing problem in aberration issue [142] and was studied with respect to the field magnitude at the focus [143] using aperture theory and method of moment[144], and quasi Bessel beam with the similar configuration has been recently investigated with an arbitrary point source using aperture distribution and Fresnel diffraction integral[145].

The source point in the present work is the focal point of primary parabolic mirror.

In this case, the focusing of the primary mirror is not necessarily highly tight. It can be optimized for the given purpose.

The secondary mirror provides position-dependent conic angle which displays an interesting feature of this configuration. Generation of quasi Bessel beam using gradually varying conic angle has been recently studied with axicon lens [146], [147].

In Fig. 5.3(c), The change of conic angle according to the position is not linear due to the geometry of the parabolic mirror resulting the existence of a point (turning point) on the surface of secondary mirror where the reflected beam creates a maximum conic angle which affects the size of the central lobe of the beam.

5.7.2   Incident waves

The illuminating waves coming through the source point in this work has several special characteristics. First, it is spherical waves, not plane waves, since they are waves which dispersed from the focus of the primary mirror. Second, the waves are radially polarized by the mechanism of the radiation of monopole of the mirror 1. Third, the waves are created by the radiation of monopole and thus the gain from the directivity of the radiation pattern is transferred to the illuminating waves. It has a doughnut shape (like first order Bessel beam) and electric fields are directed in the radial direction. As for the frequency range, the waves used in the configuration here belong to microwaves. The microwave Bessel beam has already been studied by [148], [149], [150], [151] and [150]. . The characteristics mentioned above should be taken into account in the further consideration.

We investigate model (c) in detail beginning from the analysis with the geometric consideration.

5.7.3   Geometric analysis

The schematic of the system with parabolic mirror and geometric points to be considered are shown in Fig. 5.4. From the optical geometry, we get,

$$a = c\tan(\theta_1) = (c+s)\tan(\theta_2) = (c+s+g)\tan(\theta_3) = (c+s+g+d)\tan(\theta_4) \qquad (5.14)$$

$$\theta_1 = \varphi_1 + \theta_2 \qquad (5.15)$$

$$\theta_2 = \varphi_2 + \theta_3 \qquad (5.16)$$

$$\theta_3 = \varphi_2 + \theta_4 \qquad (5.17)$$

$$\theta_4 = \theta_3 - \varphi_2 = \theta_3 - (\theta_2 - \theta_3) = 2\theta_3 - \theta_2 \qquad (5.18)$$
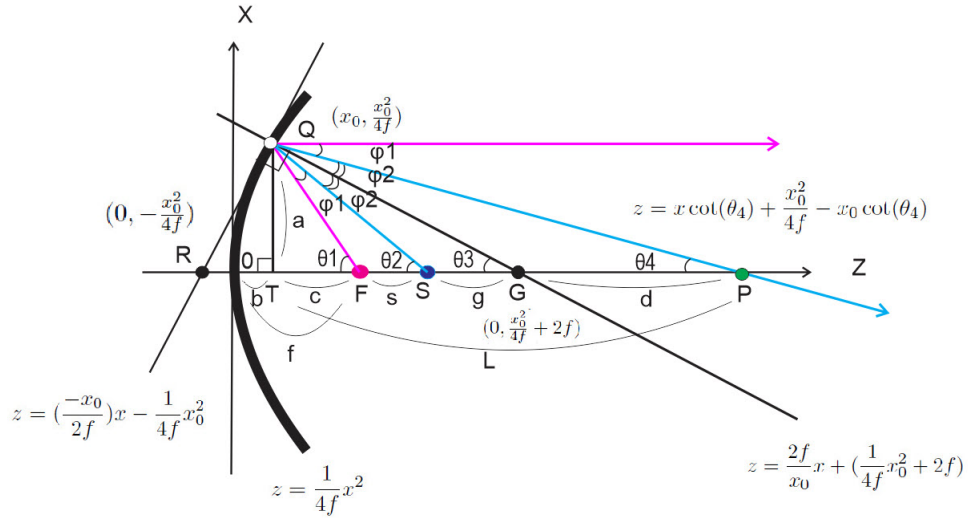
Figure 5.4: Schematics of spherical off focus illumination

Equation of parabola is

$$z = \frac{1}{4f}x^2 \tag{5.19}$$

From the coordinates of the point Q in the Fig. (5.4), $b = f - c = z_0 = \frac{x_0^2}{4f} = \frac{a^2}{4f}$, Therefore,

$$\theta_1 = \arctan\left(\frac{a}{c}\right) = \arctan\left(\frac{a}{f - \frac{a^2}{4f}}\right) \tag{5.20}$$

$$\theta_2 = \arctan\left(\frac{a}{c + s}\right) = \arctan\left(\frac{a}{f - \frac{a^2}{4f} + s}\right) \tag{5.21}$$

$$\theta_3 = \arctan\left(\frac{a}{c + s + g}\right) = \arctan\left(\frac{a}{f - \frac{a^2}{4f} + s + g}\right) \tag{5.22}$$

$$\theta_4 = 2\theta_3 - \theta_2 = 2\arctan\left(\frac{a}{f - \frac{a^2}{4f} + s + g}\right) - \arctan\left(\frac{a}{f - \frac{a^2}{4f} + s}\right) \tag{5.23}$$

$$L = \frac{a}{\tan(\theta_4)} = \frac{a}{2\arctan(\frac{a}{f - \frac{a^2}{4f} + s + g}) - \arctan(\frac{a}{f - \frac{a^2}{4f} + s})} \tag{5.24}$$

The equation of the tangential line passing a point (x_0, z_0) is

$$z = \left(\frac{-x_0}{2f}\right)x - \frac{1}{4f}x_0^2 \tag{5.25}$$

and the equation of the line perpendicular to the tangential line (Equation (5.25)) at the point (x_0, z_0) is

$$z = \frac{2f}{x_0}x + (\frac{1}{4f}x_0^2 + 2f)$$ (5.26)

The equation of the line of reflected wave is

$$z = x\cot(\theta_4) + \frac{x_0^2}{4f} - x_0\cot(\theta_4)$$ (5.27)

This perpendicular line crosses z axis at G i.e., $(0, \frac{1}{4f}x_0^2 + 2f)$. Since z coordinate of this point is $\frac{a^2}{4f} + 2f = f + s + g$, hence g is $g = \frac{a^2}{4f} + f - s$. Putting this value of g into Equation (5.22), (5.23), we obtain,

$$\theta_3 = \arctan\left(\frac{a}{2f}\right)$$ (5.28)

$$\theta_4 = 2\arctan\left(\frac{a}{2f}\right) - \arctan\left(\frac{a}{f - \frac{a^2}{4f} + s}\right)$$ (5.29)

and the distance L is

$$L = \frac{a}{\tan(\theta_4)} = \frac{a}{2\arctan\left(\frac{a}{2f}\right) - \arctan\left(\frac{a}{f - \frac{a^2}{4f} + s}\right)}$$ (5.30)

We can express a, θ_4 and L in θ_2 as follows;
From Equation (5.14),

$$a = (f - \frac{a^2}{4f} + s)\tan(\theta_2)$$ (5.31)

or in quadratic expression,

$$\frac{\tan(\theta_2)}{4f}a^2 + a - (f + s)\tan(\theta_2) = 0$$ (5.32)

The practical solution, which is expressed through θ_2 is

$$a = \frac{2f(-1 + \sqrt{1 + (1 + \frac{s}{f})\tan^2(\theta_2)}}{\tan(\theta_2)}$$ (5.33)

By substituting Equation (5.33) into (5.29), (5.30), we get,

$$\theta_4 = 2\arctan\left(\frac{-1 + \sqrt{1 + (1 + \frac{s}{f})\tan^2\theta_2}}{\tan\theta_2} - \theta_2\right)$$ (5.34)

$$L = \left[\frac{\frac{2f(-1 + \sqrt{1 + (1 + \frac{s}{f})\tan^2(\theta_2)})}{\tan(\theta_2)}}{\tan\left(2\arctan\left(\frac{-1 + \sqrt{1 + (1 + \frac{s}{f})\tan^2(\theta_2)}}{\tan(\theta_2)}\right) - \theta_2\right)}\right]$$ (5.35)

The relations of the conic angle θ_4, the radius of diffraction aperture a and the propagation distance L from T to G with the incident angle θ_2 for focal lengths of primary and secondary mirrors $fp = 19mm$, $fs = 0.5 \times fp$ respectively and the spatial gap between focuses $s = 0.1 \times fs$ are illustrated in Fig. 5.5.
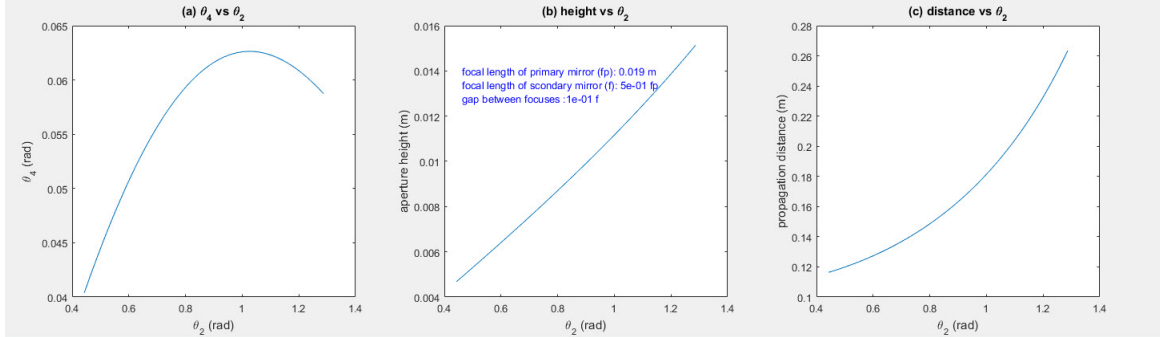

Figure 5.5: relations of cone angle (θ_4), aperture height and propagation distance vs incident beam angle (θ_2)

5.7.4   Propagation

5.7.4.1   Meaning of propagation of quasi Bessel beam

Ideal Bessel beam propagates with fixed transverse intensity profile without change in magnitude. Regarding the quasi Bessel beam, since it is only the phenomena of superposition of the spherical waves with a certain conic angle between the wave vectors k, it is just created at each point of superposition and does not propagate. However, the expression 'propagation' is commonly used in the literature. In this case, it is understood that the quasi Bessel beam is continuously created by the propagating waves. The distance of propagation is nothing but the spatial range along the axis in which the quasi Bessel beam is created. The interesting thing here is that the incident beams which lead to the quasi Bessel beams are propagating carrying the energy and thus do also the quasi Bessel beam for the distance of creation. This might be equivalent to the propagation of quasi Bessel beam itself. The magnitude of the quasi Bessel beam depends on that of each spherical wave (source wave) which creates the quasi Bessel beam. Since the spherical waves disperse and decrease in strength as it propagates, so does the quasi Bessel beam. The property of nearly non-diffraction of quasi Bessel beam only means that the size of the center lobe is constant insofar as cone angle does not change.

5.7.4.2   Position-dependent cone angle

When quasi Bessel beam is generated by an axicon, the conic angle is fixed at a certain value corresponding to the angle of axicon.

However, the conic angles of quasi Bessel beam created by the parabolic mirror in this work vary with the positions in the propagation range due to the geometry of the parabolic mirror. The conic angle at a certain position also varies depending on the size of the spatial gap between focuses of primary and secondary mirrors.

Since conic angle affects the range of the quasi Bessel beam which extends from the mirror and also the transverse intensity profile, the location, the length and the size of the core lobe (spot size) of the quasi Bessel beam can be optimized for the given purpose by adjusting the conic angle through change of the spatial gap between two focuses.

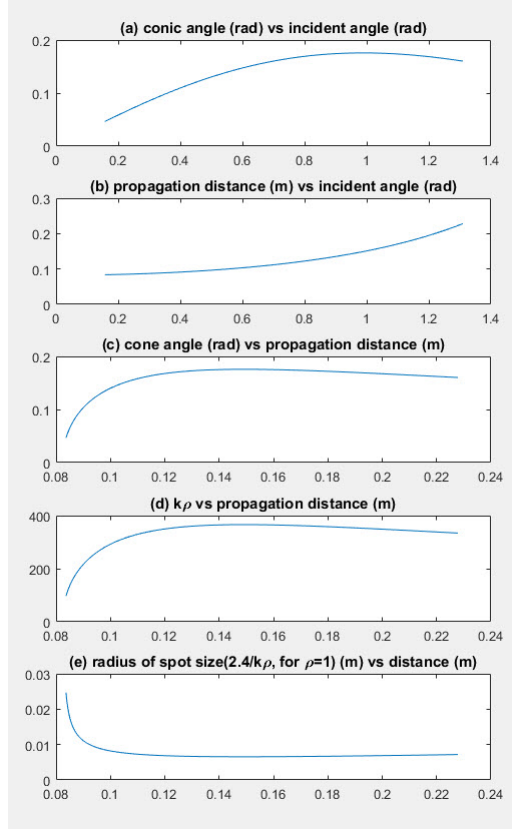This special feature of parabolic mirror is illustrated in Fig. 5.6.

Figure 5.6: Position-dependent conic angle and associated parameters

Fig.5.6 is the simulation for the system with focal length $f = 0.019m$, the size of gap between focus and wave point source $s = 0.3f$.

Fig.5.6(a) shows the relation between conic angle vs angle of the incident waves. The conic angle increases in the beginning as incident angle increases, but it is not linear. there is a maximum and thus a turning point.

(b) illustrates relation between propagation distance and associated incident angle.

(c) shows relation between conic angle and associated propagation distance. The conic angle first increases and then slowly decreases after arriving maximum.

(d) shows relation between transverse component of wave vector k determined by the conic angle $k_\rho = k \sin \theta$ and the propagation distance. k_ρ first increases but later decreases .

(e) illustrates the relation between radius of spot size (first lobe of Bessel function) calculated by $\Delta\rho \sim 2.4/(k_\rho \times \rho)$ for $\rho = 1$ and the propagation distance. The radius of the spot size is maximum at the point where quasi Bessel beam begins and reduces rapidly until it gets the almost stable-looking size.
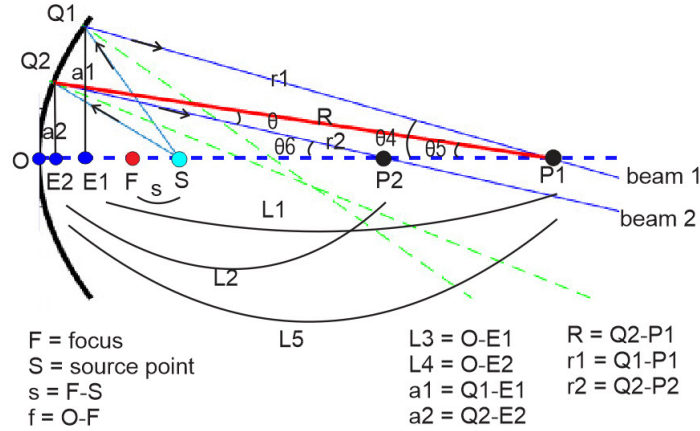
Figure 5.7: diagram of changing cone angle

Fig. 5.7 is the self explanatory diagram illustrating geometric optics of the system.
The turning point occurs from purely geometric reason.

We are interested in the field at $P1$ where the main reflected beam (beam 1) crosses
the z axis. The secondary beam (beam 2) actually passes the point $P2$ on the axis. But,
according to the Huygens wavelet theory, each reflecting point on the surface of the mirror
can be assumed to be secondary wave source. The beam 2 also affects $P1$ with the amplitude
of $\cos(\theta)$ of field magnitude. From the geometry of the system as shown in this figure, we
get,

$$\theta_5 = \arctan(a2/L5) \tag{5.36}$$

$$L5 = L1 + (L3 - L4) \tag{5.37}$$

$$\theta = \theta_6 - \theta_5 \tag{5.38}$$

$$r1 = a1 \csc(\theta_4) \tag{5.39}$$

$$R = a2 \csc(\theta_5) \tag{5.40}$$

Total field amplitude at $P1$ can be calculated by the Huygens-Fresnel principle integrat-
ing over the height of the reflection aperture of the mirror from the z axis [152, p.52].

$$A(\rho, z) = \frac{1}{i\lambda} \int_{a0}^{a1} \rho A(\rho, 0) \frac{exp(ikR)}{R} \cos\theta d\rho \tag{5.41}$$

where, in cylindrical coordinates, ρ is radial distance from axis on the plane passing the
reflection point and perpendicular to z-axis, R distance from reflection point on the surface
of mirror to observation point, θ the angle between the ray path and the direction to the
observation point at the reflection point on the surface of mirror. The fraction $\frac{1}{i\lambda}$ comes
from the fact that the wave motion from the aperture of the mirror to the observation
point takes place by virtue of the time-rate-of-change of the field $(d \exp i(kx - \omega t)/dt)$ at
reflection point. The directivity pattern $\cos\theta$ is the obliquity factor. The Huygens-Fresnel
principle expresses just the superposition integral of diverging spherical waves originating

from secondary sources on the surface of the mirror at the observation point located at the distance R.

$A(\rho, 0)$ is the field amplitudes of secondary sources located at each on the mirror surface.

5.7.4.3   Incompatibility of aperture distribution method

The two commonly used method for reflectors are the aperture distribution and the current distribution methods[67] . The aperture method is the technique where the field reflected by the surface of the paraboloid is first found over an aperture plane which is normal to the optical axis mostly at the focus (focal plane) and the field distribution on the aperture plane is assumed as an equivalent source of the radiation.
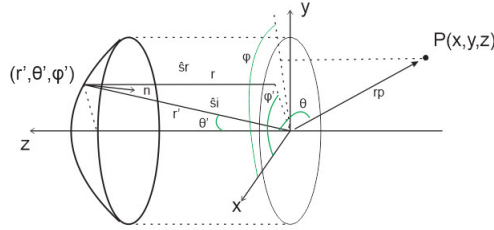

Figure 5.8: aperture

The current distribution method is the technique where the physical optics approximation of the current density induced by incident field is formulated over the surface of the reflector which is then integrated over the whole surface.

The aperture method has the advantage in that the integration is much easier than in the current method. According to the aperture distribution method, the electric field at the aperture plane ($\mathbf{E_{ap}}$) passing through the focal point is given by [67, p.903]

$$\mathbf{E}_{ap} = \hat{\mathbf{e}}_r C_1 \sqrt{G_f(\theta', \phi')} \frac{\exp(-jkr'(1 + \cos\theta'))}{r'} = \hat{\mathbf{a}}_x E_{xa} + \hat{\mathbf{a}}_y E_{ya} \qquad (5.42)$$

where E_{xa} and E_{ya} represent the x- and y-components of the reflected field over the aperture. Referring to Fig. 5.8, θ' is the angle between optical axis (z axis) and ray illuminating to the mirror surface at the focus, r' the distance of the illuminating ray, ϕ' azimuthal angle of the reflecting point, $\hat{\mathbf{e}}_r$ a unit vector depicting the polarization of the reflected field at the reflection point on the surface, $\hat{\mathbf{a}}_x$, $\hat{\mathbf{a}}_y$ unit vector of x and y component of $\hat{\mathbf{e}}_r$ on the aperture plane respectively, $G_f(\theta', \phi')$ a gain function of the fields radiated from the point source placed at the focal point of the reflector given by radiation intensity $U(\theta', \phi')$ equation from total radiation power P_t,

$$U(\theta', \phi') = \frac{P_t}{4\pi} G_f(\theta', \phi') \qquad (5.43)$$

and C_1 the constant given by

$$C_1 = (\frac{\mu}{\varepsilon})^{1/4} (\frac{P_t}{2\pi})^{1/2} \qquad (5.44)$$

In the numerator of the fraction, total distance from the source point to the aperture is well represented $(r' + r = R'(1 + \cos\theta'))$ while in denominator, since the field from the

reflector to the aperture plane is assumed a plane wave, only the the distance from the source to the reflection point r' is considered.

However, when the source is positioned not at the focus, rather at off-focus, the reflected field is a spherical wave, not a plane wave. Accordingly, we have to consider the whole distance from the source to the aperture also in the denominator.

5.7.4.4   Incompatibility of Fresnel approximation

In case of the Bessel-Gaussian beam generated by the axicon, the amplitude is within the Gaussian envelope and the created beam starts from the axicon aperture with the fixed cone angle, and we can express it as

$$A(\rho, 0) = exp(-\rho^2/w_0^2)J_0(k_\rho \rho) \qquad (5.45)$$

where w_0 is Gaussian beam waist, J_0 the zero order Bessel function of the first kind, and k_ρ the transverse component of wave vector

$$k_\rho = k \sin(\theta) \qquad (5.46)$$

In this case, the whole spatial range of the quasi Bessel beam is equivalent to the propagation of the quasi Bessel beam created at the origin. Accordingly, for the analysis of the propagation of quasi Bessel beam, it is common to use the Fresnel diffraction integral which is the result of Fresnel approximation on the distance part based on the paraxial character of the beam instead of using the exact formula (5.41).
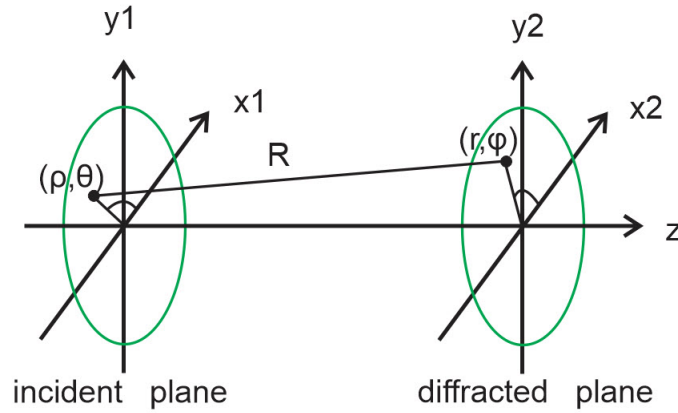
Figure 5.9: incident and diffracted planes

Referring to Fig. 5.9, in Fresnel approximation, first, we replace obliquity factor $\cos\theta$ in Equation (5.41) with z/R. By assuming $R \sim z$ in paraxial limit, we neglect the obliquity factor and replace R in the denominator with z. For the numerator, we can not do the same thing because k of light is too large. Therefore, we make an approximation only by taking terms to quadratic one in binomial expansion of distance R between a pair points on the

incident and diffracted planes in Cartesian coordinates $(x_1, y_1, 0)$ and (x_2, y_2, z), and their cylindrical coordinates, ρ, θ and r, φ respectively and we get [153],

$$A(x_2, y_2, z) = \frac{1}{i\lambda z} \int_{-\infty}^{\infty} \int_{-\infty}^{\infty} A(x_1, y_1, 0) exp(ikR) dx_1 dy_1 \qquad (5.47)$$

where

$$\begin{aligned} R =& [(x_2 - x_1)^2 + (y_2 - y_1)^2 + z^2]^{1/2} \\ =& z + \frac{r^2 + \rho^2}{2z} - \frac{2r\rho \cos(\theta - \varphi)}{2z} \end{aligned} \qquad (5.48)$$

By taking into account that incident amplitude $A(x_1, y_1, 0)$ is circularly symmetric, we get in cylindrical coordinates,

$$A(r, z) = exp\left(ikz + \frac{ikr^2}{2z}\right) \left(\frac{k}{iz}\right) \int_0^{\infty} \rho A(\rho, 0) J_0 \left(\frac{k\rho r}{z}\right) exp\left(\frac{ik\rho^2}{2z}\right) d\rho \qquad (5.49)$$

where J_0 is the zero order Bessel function of the first kind.

However, there are some reasons that the Fresnel approximation is not appropriate to this on-axis-off-focus structure of parabolic mirror.

First, the reflected beam spreads greatly unless the point source of waves locate very near the focus. Second, the surface of the mirror has curvature and the obliquity angle θ at each point varies according to the curvature of the mirror surface which has nothing to do with position on z-axis. Consequently, $\cos \theta$ can not be simply replaced with z/R and expansion of R does not yield correct value. Another reason is that the conic angle made by the reflected waves is not constant. It is z-position-dependent such that the amplitude of Bessel beam has to be calculated at each point with different conic angle. Bessel beam with varying conic angle has been studied recently [147], [146]. But, they all concern the beams generated by axicons.

Furthermore, for the summation of the magnitude of each beams at the point $P1$, we have to take into consideration;

1) The incident waves travelling from the source point are the waves which spread after focusing of the primary parabolic mirror. The magnitude spectrum on the reflecting surface of the secondary mirror carries the same field distribution gain generated by the monopole antenna.

2)The magnitude contribution of each reflected wave to the point $P1$ in Fig. 5.7 depends on the obliquity factor $(\cos \theta)$of each point on the surface of the secondary mirror, which relies on the parabolic curvature on that point as mentioned above.

These all special situations lead us to the conclusion that the Fresnel diffraction integral is not appropriate to this parabolic mirror case.

5.7.4.5   Application of Huygens-Fresnel principle without approximation

Therefore, we have to solve this problem by applying the equation of Huygens-Fresnel principle exactly, without relying on any method of approximation, through putting Equations from (5.36) to (5.40) into Equation (5.41), which means we have to calculate numerically.

The radial component of k vector is,

$$k_\rho = k \sin(\theta_4) \tag{5.50}$$

The numerical simulation is shown in Fig. 5.10. as a succession of quasi Bessel beam patterns at increasing distance of gap from the focus.

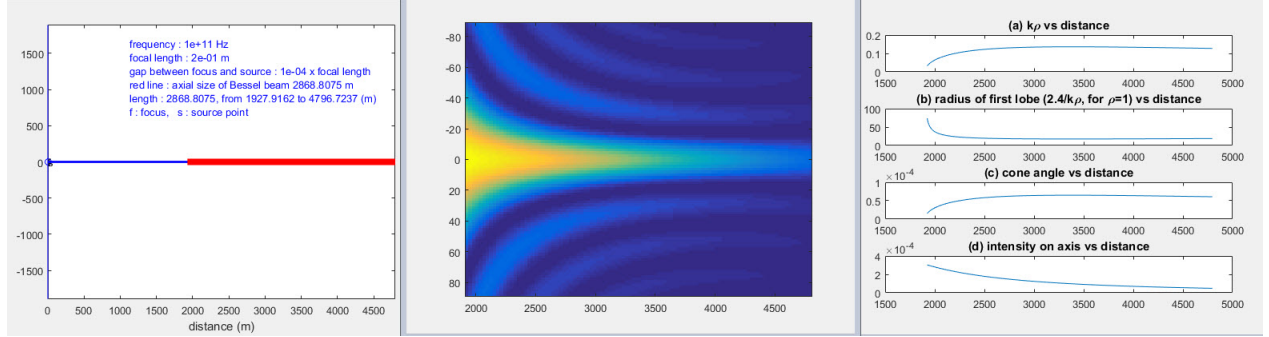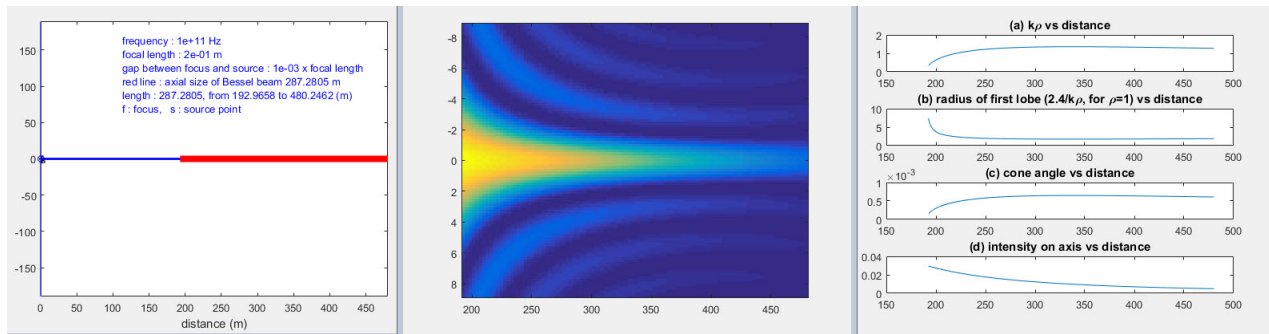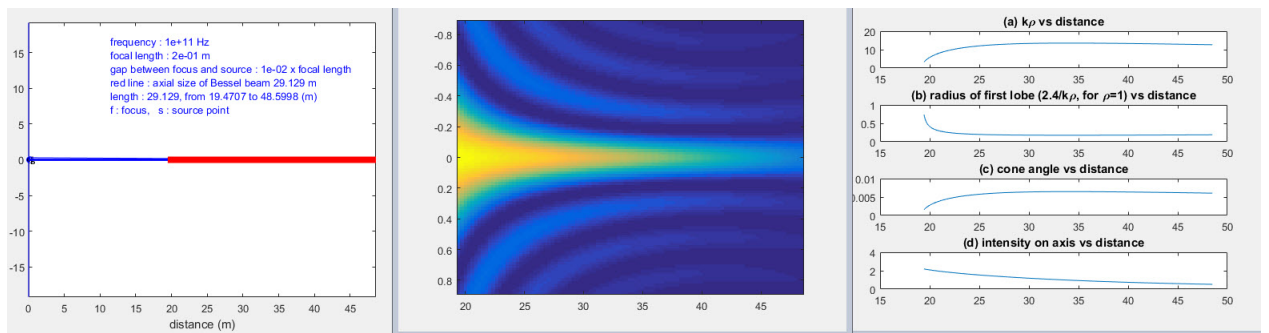Figure 5.10: (1) frequency=100 GHz, focal length (fl)=0.19 m, gap=0.0001 × fl

(2) frequency=100 GHz, focal length (fl)=0.19 m, gap=0.001 × fl

(3) frequency=100 GHz, focal length (fl)=0.19 m, gap=0.01 × fl
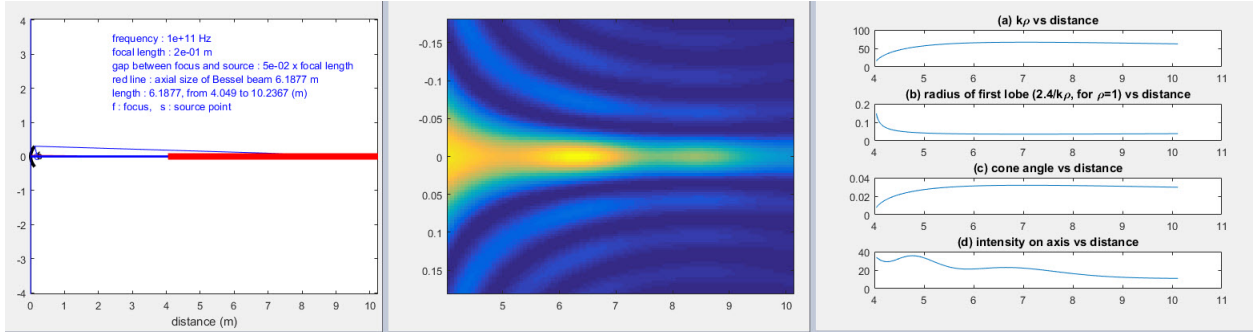
(4) frequency=100 GHz, focal length (fl)=0.19 m, gap=0.05 × fl
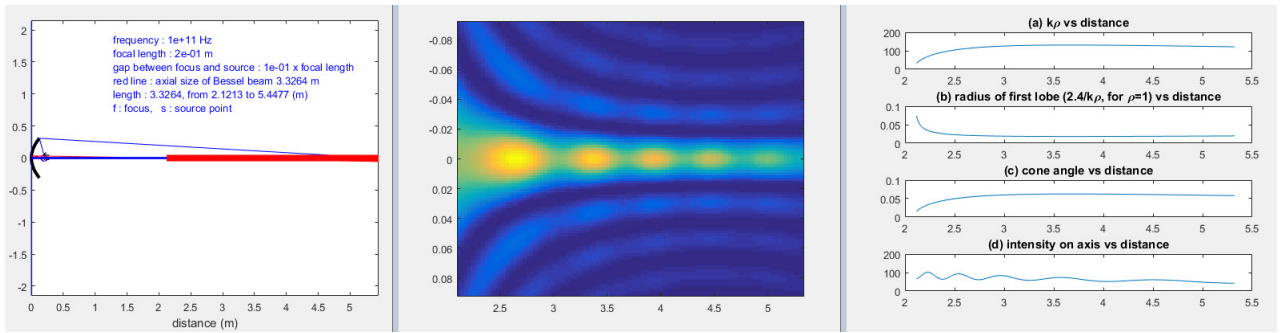
(5) frequency=100 GHz, focal length (fl)=0.19 m, gap=0.1 × fl
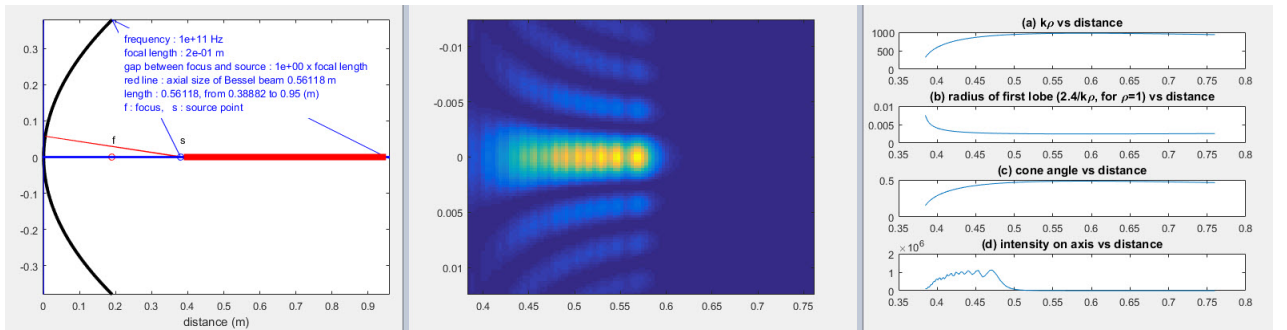
(6) frequency=100 GHz, focal length (fl)=0.19 m, gap=1 × fl
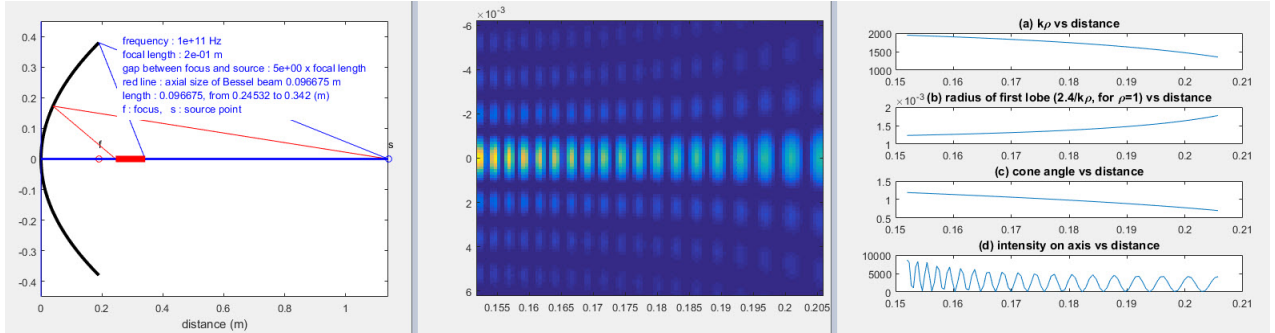
(7) frequency=100 GHz, focal length (fl)=0.19 m, gap=5 × fl
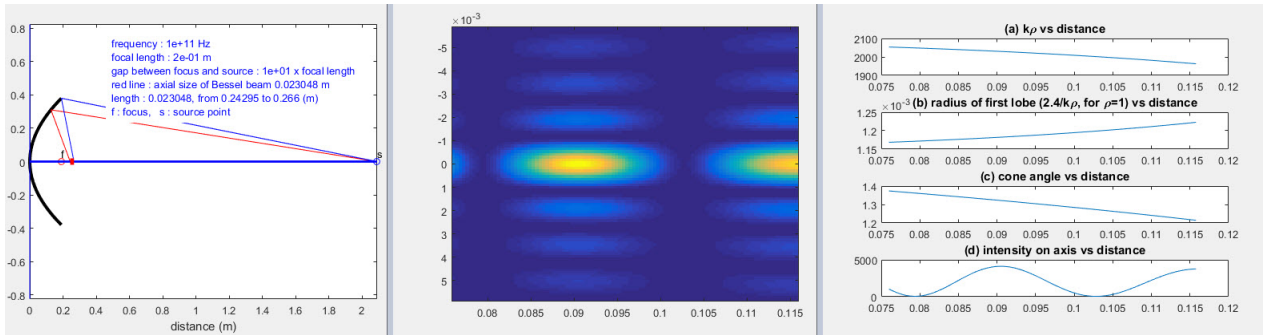
(8) frequency=100 GHz, focal length (fl)=0.19 m, gap=10 × fl
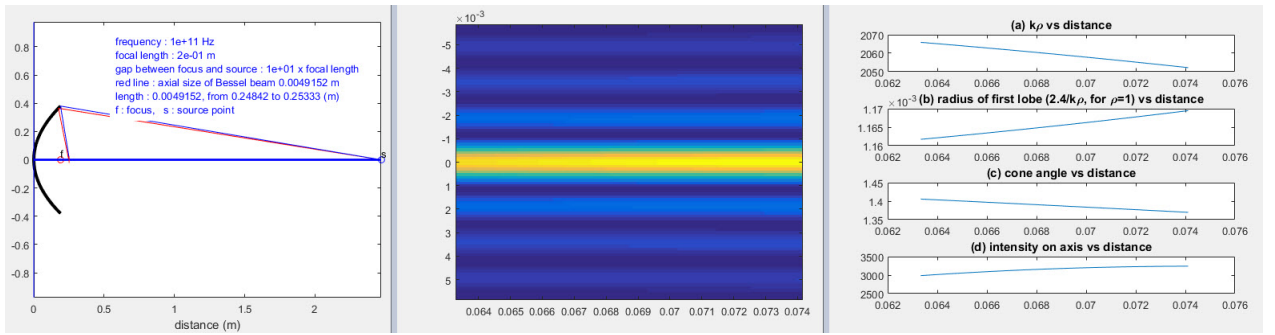
(9) frequency=100 GHz, focal length (fl)=0.19 m, gap=12 × fl

The first figures of each pair are geometric diagrams showing the locations and the lengths of the quasi Bessel beams associated with the positions of the source points. The second figures of each pair are surf simulations of the quasi Bessel beams. The third parts of each pair show the relations between k_ρ, radius of spot size (first lobe), conic angle and intensity on the z-axis vs propagation distance.

The gap between the focus and the source increases from $0.0001fl$ to $12fl$ where fl is focal length. For shorter gap, the quasi Bessel beam is created at the longer distance from the mirror with a longer beam length, while, for longer gap, everything is in the opposite.

The spot size starts with comparatively bigger width for the shorter gap and reduces as the beam propagates. The intensity on the axis is greater at the nearer position.

It is of interest to note that, for the quasi Bessel beam created near the mirror due to the long gap, the broad width of the lobe at the starting position reduces and the position of maximum intensity on the axis moves to the middle of the propagation.

This interesting phenomena is due to the non-linear variation of the conic angle.

As already mentioned, it is interesting to note that the change of cone angle according to the linearly increasing incident angle is not linear and has a turning point. This phenomenon is purely due to the geometry of the parabolic mirror. The exact position where this phenomena happen is illustrated in Fig. 5.11 which shows turning point. This point depends on the length of the gap between focuses.
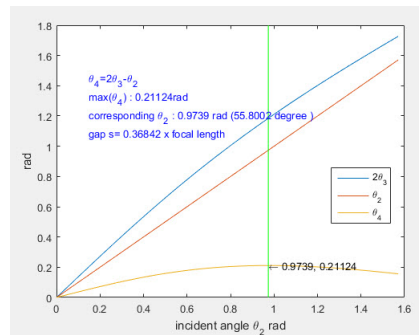
Figure 5.11: Maximum conic angle

This might be exploited for some given purposes. By applying the laser instead of microwaves, the more precise and comparatively long distance of the beam can be exploited for the particle acceleration.

5.7.4.6   Multiple point sources - line transmission antenna

So far we have seen quasi Bessel beam illuminated by one point source. If the illuminating source is a combination of multiple point sources on the z-axis, there should be a superposition of the quasi Bessel beams created by each point sources. A line antenna is assumed as a collection of a large number of infinitesimal dipoles, namely, Hertzian dipoles. The fields radiated from a line antenna is the superposition of fields from a large number of infinitesimal Hertzian dipoles in the line antenna. For convenience, we consider a simple structure which consists of a parabolic reflector and a line of point sources. The position of the quasi Bessel beams and the total field intensities are calculated by the superposition which is shown in Fig. 5.12.

focal length : 2e-02 m
gap between focus and source : 1e-01 x focal length
green line : axial size of Bessel beam created by nearest point of line antenna 0.18747 m
red line : axial size of Bessel beam created by farthest point of line antenna 0.18747 m
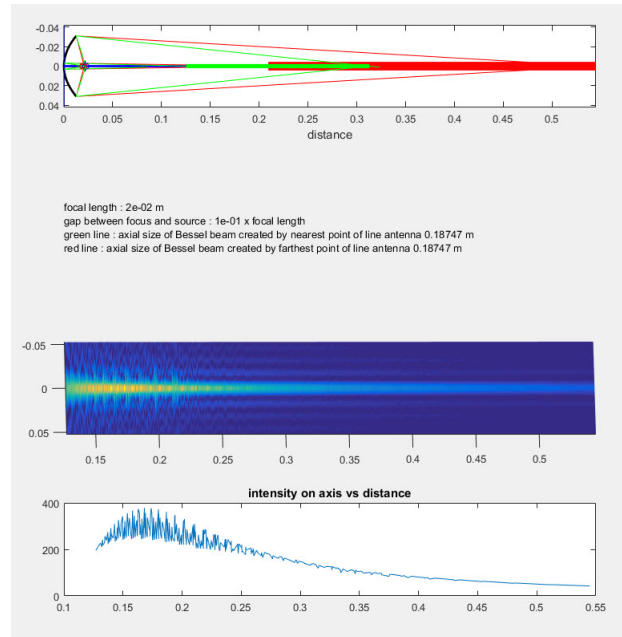
Figure 5.12: Multiple points source - antenna

5.8 Conclusion

Two-parabolic-mirror system in this work finds an application of generating quasi Bessel beam of varying cone angles with off-focus illumination. The crucial point of quasi Bessel beam with varying cone angle is that it can concentrate the field intensity on the finite axial length at arbitrary position through optimizing the gap distance of source from focus. It may provide versatility in various Bessel beam applications.

Bibliography

[1] S.Quabis, R.Dorn, M. Eberler, O.Glockl, and G.Leuchs, "Focusing light to a tighter spot," *Opt. Commun.*, vol. 179, p. 1, 2000.

[2] D. Cline, L. Shao, X. Ding, Y. Ho, Q. Kong, and P. Wang, "First observation of acceleration of electrons by a laser in a vacuum," *Journal of Modern Physics*, vol. 4, p. 1, 2013.

[3] Y.I.Salamin, "Acceleration in vacuum of bare nuclei by tightly focused radially polarized laser light," *Opt. Lett.*, vol. 32, p. 3462, December 2007.

[4] M.A.Lieb and A.J.Meixner, "A high numerical aperture parabolic mirror as imaging device for confocal microscopy," *Optics Express*, vol. 8, pp. 458–474, March 2001.

[5] Y. Zhang, "Theoretical study of near-field optical storage with a solid immersion lens," *J. Opt. Soc. Am.*, vol. A 23, pp. 2132–2136, 2006.

[6] V.G.Niziev and A.V.Nesterov, "Influence of beam polarization on laser cutting efficiency," *J. Phys. D Appl. Phys.*, vol. 32, pp. 1455–1461, 1999.

[7] Q. Zhan, "Trapping metallic rayleigh particles with radial polarization," *Opt. Express*, vol. 12, no. 33773382, 2004.

[8] J.L.Gomez-Tornero, F. Quesada-Pereira, A. Alvarez-Melcon, G. Goussetis, A. R. Weily, and Y. Guo, "Frequency steerable two dimensional focusing using rectilinear leaky-wave lenses," *IEEE Trans. Antennas Propag.*, vol. 59, no. 2, p. 407, 2011.

[9] M. Ettorre, M. Casaletti, G. Valerio, R. Sauleau, L. L. Coq, S. C. Pavone, and M. Albani, "On the near-field shaping and focusing capability of a radial line slot array," *IEEE Trans. Antennas Propag.*, vol. 62, no. 4, p. 1991, 2014.

[10] J. L. Gomez-Tornero, A. J. Martinez-Ros, N. Llombart, D. Blanco, and E. Rajo-Iglesias, "Near-field focusing with holographic two- dimensional tapered leaky-wave slot antennas," *Proc. EuCAP*, p. 234, Mar. 2012.

[11] D. Blanco, J. Gomez-Tornero, E. Rajo-Iglesias, and N. Llombart, "Radially polarized annular-slot leaky-wave antenna for three-dimensional near-field microwave focusing," *IEEE Trans. Antennas Propag. Lett.*, vol. 13, p. 583, 2014.

[12] M. Bachynski and G. Bekefi, "Study of optical diffraction images at microwave frequencies," *J. Opt. Soc. Am*, vol. 47, p. 428, May 1957.

[13] G. Farnell, "Calculated intensity and phase distribution in the image space of a microwave lens," *Can. J. Phys.*, vol. 35, p. 777, 1957.

[14] G. Farnell, "Measured phase distribution in the image space of a microwave lens," *Can. J. Phsy.*, vol. 36, p. 935, 1958.

[15] G. Farnell, "On the axial phase anomaly for microwave lenses," *J. Opt. Soc. Am*, vol. 48, p. 643, September 1958.

[16] A.I.Carswell, "Measurements of the longitudinal component of the electromagnetic field at the focus of a coherent beam," *Phys. Rev. Lett.*, vol. 15, pp. 647–649, Oct. 1965.

[17] E.J.Bochove, G.T.Morrre, and M.O.Scully, "Acceleration of particles by an asymmetric hermite-gaussian laser beam," *Physical Review A*, vol. 46, p. 6640, 1992.

[18] R.Dorn, S.Quabis, and G. Leuchs, "Sharper focus for a radially polarized light beam," *Phys. Rev. Lett.*, vol. 91, p. 233901, 2003.

[19] N.Davidson and N.Bokor, "High-numerical-aperture focusing of radially polarized doughnut beams with a parabolic mirror and a flat diffractive lens," *Opt. Lett.*, vol. 29, p. 1318, 2004.

[20] J. Stadler, C. Stanciu, C. Stupperich, and A. J. Meixner, "Tighter focusing with a parabolic mirror," *Opt. Lett.*, vol. 33, p. 681, 2008.

[21] S.Winnerl, R.Hubrich, M.Mittendorff, H.Schneider, and M.Helm, "Universal phase relation between longitudinal and transvers fields observed in focused terahertz beams," *New Journal of Physics*, vol. 14, pp. 1–12, Oct. 2012.

[22] B. Richards and E. Wolf, "Electromagnetic diffraction in optical systems. ii. structure of the image field in an aplanatic system," *Proc. Roy. Soc. A*, vol. 253, pp. 358–379, 1959.

[23] K.S.Youngworth and T.G.Brown, "Focusing of high numerical aperture cylindrical-vector beams," *Optics Express*, vol. 7, p. 77, July 2000.

[24] Y. Kozawa and S. Sato, "Sharper focal spot formed by higher-order radially polarized laser beams," *J. Opt. Soc. Am. A*, vol. 24, no. 6, p. 1793, 2007.

[25] M. Lax, W.H.Louidell, and B.McKnight, "From maxwell to paraxial wave optics," *Phys. Rev. A*, vol. 11, no. 4, p. 1365, 1975.

[26] L. Davis, "Theory of electromagnetic beams," *Phys.Rev. A*, vol. 19, no. 3, p. 1177, 1979.

[27] G. P. Agrawal and D. N. Pattanayak, "Gaussian beam propagation beyond the paraxial approximation," *J. Opt. Soc. Am.*, vol. 69, no. 4, p. 575, 1979.

[28] Y. Salamin, "Fields of a radially polarized gaussian laser beam beyond the paraxial approximation," *Opt. Lett.*, vol. 31, no. 17, p. 2619, 2006.

[29] C. Varin, M. Piche, and M. Porras, "Acceleration of electrons from rest to gev energies by ultrashort transverse magnetic laser pulses in free space," *Phys. Rev. E*, vol. 71, p. 026603, 2005.

[30] G.A.Deschamps, "Gaussian beam as a bundle of complex rays," *Electronics Lett.*, vol. 7, no. 23, p. 685, 1971.

[31] M. Couture and P.-A. Belanger, "From gaussian beam to complex-source-point spherical wave," *Phys. Rev. A*, vol. 24, no. 1, p. 355, 1981.

[32] A. April, "Nonparaxial tm and te beams in free space," *OIPt.Lett.*, vol. 33, no. 14, p. 1563, 2008.

[33] A. Sommerfeld, *Optics(Lectures on Theoretical Physics, Vol IV*. ACADEMIC PRESS New York San Francisco London, 1964.

[34] J.J.Stamnes, *Waves in Focal Regions*. Adam Hilger, Bristol and Boston, 1986.

[35] M.Born and E.Wolf, *Principles of optics*. Cambridge University Press, 7 ed., 1999.

[36] P.Debye, "Das verhalten von lichtwellen in der nahe eines brennpunktes oder einer brennlinie," *Ann. Phys. Lpz.*, vol. 30, pp. 755–776, 1909.

[37] M.Born and E.Wolf, *Principlaes of Optics*. London: Pergamon Press., 1959.

[38] E. Wolf, "Electromagnetic diffraction in optical systems. i. an integral representation of the image field," *Proc. Roy. Soc A*, vol. 253, pp. 49–357, 1959.

[39] M. Leutenegger, R. Rao, R. Leitgeb, and T. Lasser, "Fast focus field calculations," *Opt. Express*, vol. 14, no. 23, p. 11277, 2006.

[40] A. April, "Nonparaxial tm and te beams in free space," *Opt. Lett.*, vol. 33, no. 14, p. 1563, 2008.

[41] V. Galindo-Israel and R. Mittra, "A new series representation for the radiation integral with application to reflector antennas," *IEEE Trans. Antennas Propag.*, vol. AP-25, no. 5, p. 631, 1977.

[42] H. Ling, S. Lee, P. Lam, and W. Rusch, "Focal shifts in parabolic reflectors," *IEEE Trans. Antennas Propag.*, vol. AP-33, no. 7, p. 744, 1985.

[43] P. Varga and P. Torok, "Focusing of electromagnetic waves by paraboloid mirrors. i. theory," *J. Opt. Soc. Am. A*, vol. 17, no. 11, p. 2081, 2000.

[44] P. Varga and P. Torok, "Focusing of electromagnetic waves by paraboloid mirrors. ii. numerical results," *J. Opt. Soc. Am. A*, vol. 17, no. 11, p. 2090, 2000.

[45] C. Sheppard, A. Choudhury, and J. Gannaway, "Electromagnetic field near the focus of wide-angular lens and mirror systems," *IEE J. Microw. Opt. Acoust.*, vol. 1, no. 4, p. 129, 1977.

[46] C. J. R. Sheppard, "Electromagnetic field in the focal region of wide-angular annular lens and mirror systems," *IEE J. Microw. Opt. Acoust.*, vol. 2, no. 5, p. 163, 1978.

[47] R. Barakat, "Diffracted electromagnetic fields in the neighborhood of the focus of a paraboloidal mirror having a central obscuration," *Appl. Opt.*, vol. 26, no. 18, p. 3790, 1987.

[48] Z. Nie, G. Shi, X. Zhang, Y. Wang, and Y. Song, "Generation of super-resolution longitudinally polarized beam with ultra-long depth of focus using radially polarized hollow gaussian beam," *Opt. Commun.*, vol. 331, pp. 87–93, 2014.

[49] H.Dahez, A.April, and M.Pich, "Needles of longitudinally polarized light: guidelines for minimum spot size and tunable axial extent," *Optical Express*, vol. 20, p. 14891, July 2012.

[50] M. E. O. G. S. Quabis, R. Dorn and G. Leuchs, "The focus of light- theoretical calculation and experimental tomographic reconstruction," *Appl. Phys. B*, vol. 72, p. 109, 2001.

[51] L. Novotny, M. Beversluis, K. S. Youngworth, and T. G. Brown, "Longitudinal field modes probed by single molecules," *Phys. Rev. Lett.*, vol. 86, no. 23, p. 5251, 2001.

[52] G. Miyaji, N. Miyanaga, K. Tsubakimoto, K. Sueda, and K. Ohbayashi, "Intense longitudinal electric fields generated from transverse electromagnetic waves," *Appl. Phys. Lett.*, vol. 84, no. 19, p. 3855, 2004.

[53] B. Jia, X. Gan, and M. Gu, "Direct measurement of a radially polarized focused evanescent field facilitated by a single lcd," *Opt. Express*, vol. 13, no. 18, p. 6821, 2005.

[54] T. Wilson, F. Massoumian, and R. Juskaitis, "Generation and focusing of radially polarized electric fields," *SPIE Opt. Eng.*, vol. 42, p. 3088, 2003.

[55] G. K. Rurimo, M. Schardt, S. Quabis, S. Malzer, C. Dotzler, A. Winkler, G. Leuchs, G. H. Dhler, D. Driscoll, M. Hanson, A. C. Gossard, and S. F. Pereira, "Using a quantum well heterostructure to study the longitudinal and transverse electric field components of a strongly focused laser beam," *J. Appl. Phys.*, vol. 100, p. 032112, 2006.

[56] B. Hao and J. Leger, "Experimental measurement of longitudinal component in the vicinity of focused radially polarized beam," *Opt. Express*, vol. 15, no. 6, p. 3550, 2007.

[57] C. Debus, M. Lieb, A. Drechsler, and A. Meixner, "Probing highly confined optical fields in the focal region of a high na parabolic mirror with subwavelength spatial resolution," *Journal of Microscopy*, vol. 210, p. 203, 2003.

[58] D. Deng and Q. Guo, "Analytical vectorial structure of radially polarized light beams," *Opt. Lett.*, vol. 32, no. 18, p. 2711, 2007.

[59] V. Niziev and A. Nesterov, "Longitudinal fields in cylindrical and spherical modes," *J. Opt. A: Pure Appl. Opt.*, vol. 10, p. 085005, 2008.

[60] K. Kitamura, K. Sakai, and S. Noda, "Finite-difference time-domain (fdtd) analysis on the interaction between a metal block and a radially polarized focused beam," *Opt. Express*, vol. 19, no. 15, p. 13750, 2011.

[61] M. Gaffar and B. Boruah, "Poynting vector profile of a tightly focused radially polarized beam in the presence of primary aberrations," *J. Opt. Soc. Am. A*, vol. 32, no. 4, p. 660, 2015.

[62] Y. Zhang, B. Ding, and T. Suyama, "Trapping two types of particles using a double-ring-shaped radially polarized beam," *Phys. Rev. A*, vol. 81, p. 023831, 2010.

[63] Z.Nie, G.Shi., D.Li, and X.Zhang, "Tight focusing of a radially polarized laguerrebesselgaussian beam and its application to manipulation of two types of particles," *Phys. Lett. A*, vol. 379, pp. 857–863, 2015.

[64] G. Miyaji, N. Miyanaga, K. Tsubakimoto, K. Sueda, and K. Ohbayashi, "Intense longitudinal electric fields generated from transverse electromagnetic waves," *Appl. Phys. Lett.*, vol. 84, no. 19, p. 3855, 2004.

[65] M.M.Weiner, *Monopole Antennas*. Marcel Dekker, Inc, 2003.

[66] Z.ivkovi, D.Seni, C.Bodendorf, J. Skrzypczynski, and A.aroli, "Radiation pattern and impedance of a quarter wavelength monopole antenna above a finite ground plane," *In proc. of 20-th International Conference on Software, Telecommunications and Computer Networks (SoftCOM)*, 2012.

[67] C. Balanis, *Antenna Theory*. A John Wiley and Sons, Inc., 3rd ed., 2005.

[68] K. Shimoda, "Proposal for an electron accelerator using an optical maser," *Appl. Phys.*, vol. 1, no. 1, p. 33, 1962.

[69] M.O.Scully, "A simple laser linac," *Appl. Phys. B*, vol. 51, pp. 238–241, 1990.

[70] A. Grudiev, S. Calatroni, and W. Wuensch, "New local field quantity describing the high gradient limit of accelerating structures," *Phys. Rev. ST Accel. Beams*, vol. 12, p. 102001, 2009.

[71] R.J.England, "Review of laser-driven photonic structure-based particle acceleration," *IEEE J. Sel. Top. Quantum Electron.*, vol. 22, no. 2, p. 4401007, 2016.

[72] A. Seryi, *Unifying Physics of Accelerators, Lasers and Plasma*. CRC Press, Tayor and Francis Group, 2016.

[73] S.-W. B. ande P. Rousseau, T. A. Planchon, V. Chvykov, G. Kalintchenko, A. Maksimchuk, G. A. Mourou, and V. Yanovsky, "Generation and characterization of the highest laser intensities," *OPt. Lett.*, vol. 29, no. 24, p. 2837, 2004.

[74] V. Yanovsky, V. Chvykov, G. Kalinchenko, P. Rousseau, T. Planchon, T. Matsuoka, A. Maksimchuk, J. Nees, G. Cheriaux, G. Mourou, and K. Krushelnick, "Ultra-high intensity -300-tw laser at 0.1 hz repetition rate.," *Opt. Express*, vol. 16, no. 3, p. 2109, 2008.

[75] L. Wong and F. Krtner, "Direct acceleration of an electron in infinite vacuum by a pulsed radially-polarized laser beam," *Opt. Express*, vol. 18, no. 24, p. 25035, 2010.

[76] Y. Salamin, "Electron acceleration from rest in vacuum by an axicon gaussian laser beam," *Phys. Rev. A*, vol. 73, p. 043402, 2006.

[77] E. Esarey, P. Sprangle, and J. Krall, "Laser acceleration of electrons in vacuum," *Phys. Rev. E*, vol. 52, no. 5, p. 5443, 1995.

[78] J. Lawson, "Lasers and accelerators," *IEEE Transactions on Nuclear Science*, vol. NS-26, no. 3, p. 4217, 1979.

[79] P. Woodward, "A method of calculating the field over a plane aperture required to porduce a given polar diagram," *J. Inst. Electr. Eng.*, vol. 93, p. 1554, 1947.

[80] A. Chao, "Lawson-woodward theorem and laser acceleration." Lecture notes on topics in accelerator physics, 2002.

[81] R. Palmer, "An introduction to acceleration mechanisms," *(High Energy Electron Linear Colliders) Frontiers of Particle Beams, edited by M.Month and S. Turner, the series Lecture Notes in Physics (Springer-Verlag, Berlin)*, vol. 296, pp. 607–635, 1988.

[82] C. Varin, S. Payeur, V. Marceau, S. Fourmaux, and A. A. et. al., "Direct electron acceleration with radially polarized laser beams," *Appl. Sci.*, vol. 3, p. 70, 2013.

[83] W. D. Kimura, G. H. Kim, R. D. Romea, L. C. Steinhauer, I. V. Pogorelsky, K. P. Kusche, R. C. Fernow, X. Wang, and Y. Liu, "Laser acceleration of relativistic electrons using the inverse cherenkov effect," *Phys. Rev. Lett.*, vol. 74, no. 4, p. 546, 1995.

[84] W. D. Kimura, M. Babzien, I. Ben-Zvi, D. B. Cline, R. B. Fiorito, J. R. Fontana, J. C. Gallardo, S. C. Gottschalk, P. He, K. P. K. and Y. Liu, R. H. Pantell, I. V. Pogorelsky, D. C. Quimby, K. E. Robinson, D. W. Rule, J. Sandweiss, J. Skaritka, A. van Steenbergen, and V. Yakimenko, "Design and model simulations of inverse cerenkov acceleration using inverse free electron laser prebunching," *Particle Accelerator Conference, 1997. Proceedings of the 1997 (Volume:1)*, vol. 1, p. 675, 1997.

[85] T. Tajima and J. M. Dawson, "Laser electron accelerator," *Phys. Rev. Lett.*, vol. 43, no. 4, p. 267, 1979.

[86] E. Esarey, C. B. Schroeder, and W. P. Leemans, "Physics of laser-driven plasma-based electron accelerators," *Rev. Mod. Phys.*, vol. 81, p. 1229, 2009.

[87] S. Carbajo, E. Nanni, L. Wong, G. Moriena, P. D. Keathley, G. Laurent, R. D. Miller, and F. Krtner, "Direct longitudinal laser acceleration of electrons in free space," *Physical Review Accelerators and Beams*, vol. 19, p. 021303, 2016.

[88] D. Nicholson, *Introduction to Plasma Theory.* John Wiley and Sons, 1983.

[89] L. Landau and E. Lifshitz, *Mechanics.* Butterworth-Heinenann, third ed., 1976.

[90] E. Esarey, P. Sprangle, J. Krall, and A. Ting, "Overview of plasma-based accelerator concepts," *IEEE Transactions on plasma science*, vol. 24, no. 2, p. 252, 1996.

[91] F. Hartemann, S. Fochs, G. L. Sage, N. L. Jr., J. Woodworth, M. Perry, Y. Chen, and A. Kerman, "Nonlinear ponderomotive scattering of relativistic electrons by an intense laser field at focus," *Phys. Rev. E*, vol. 51, p. 4833, 1995.

[92] T. Kibble, "Mutual refraction of electrons and photons*," *Phys. Rev.*, vol. 150, no. 4, p. 1060, 1966.

[93] D. Bauer, P. Mulser, and W.-H. Steeb, "Relativistic ponderomotive force, uphill acceleration, and transition to chaos," *Phys. Rev. Lett.*, vol. 75, no. 25, p. 4622, 1995.

[94] B. Quesnel and P. Mora, "Theory and simulation of the interaction of ultraintense laser pulses with electrons in vacuum," *Phys. Rev. E*, vol. 58, no. 3, p. 3719, 1998.

[95] E. A. Startsev and C. J. McKinstrie, "Multiple scale derivation of the relativistic ponderomotive force," *Phys. Rev. E*, vol. 6, no. 7527, 55.

[96] P. Mora and T. A. Jr., "Kinetic modeling of intense, short laser pulses propagating in tenuous plasmas," *Phys. Plasmas*, vol. 4, p. 217, 1997.

[97] C. Varin and M. Piche, "Relativistic attosecond electron pulses from a free-space laser-acceleration scheme," *Phys. Rev. E*, vol. 74, p. 045602(R), 2006.

[98] E. Schamiloglu, "High power microwave sources and applications," *IEEE MTT-S Int. Microwave Symp. Dig. 2*, p. 1001, 2004.

[99] X. Yan, X. Zhang, Y. Li, F. Dang, and J. Zhang, "Power combination of a self-coherent high power microwave source," *Physics of Plasma*, vol. 22, p. 093303, 2015.

[100] J. Jackson, *Classical Electrodynamics*. John Wiley and Sons, Inc, third ed., 1999.

[101] C. Varin and M. Piche, "Acceleration of ultra-relativistic electrons using high-intensity tm01 laser beams," *Appl. Phys. B*, vol. 74, p. S83, 2002.

[102] D. N. Gupta, N. Kant, D. E. Kim, and H. Suk, "Electron acceleration to gev energy by a radially polarized laser," *Phys. Lett. A*, vol. 368, p. 402, 2007.

[103] Q. Kong, S. Miyazaki, S. Kawata, K. Miyauchi, K. Nakajima, S. Masuda, N. Miyanaga, and Y. K. Ho, "Electron bunch acceleration and trapping by the ponderomotive force of an intense short-pulse laser," *Physics of Plasmas*, vol. 10, no. 12, p. 4605, 2003.

[104] Q. Kong, S. Miyazaki, S. Kawata, K. Miyauchi, K. Sakai, Y. K. Ho, K. Nakajima, N. Miyanaga, J. Limpouch, and A. A. Andreev, "Electron bunch trapping and compression by an intense focused pulse laser," *Phys. Rev. E*, vol. 69, p. 056502, 2004.

[105] Z. Bouchal, J. Wagner, and M. Chlup, "Self-reconstruction of a distorted nondiffracting beam," *Opt. Comm.*, vol. 151, pp. 207–211, 1998.

[106] D. MCGLOIN* and K. DHOLAKIA, "Bessel beams: diffraction in a new light," *Contemporary Physics*, vol. 46, no. 1, p. 15, 2005.

[107] M. Bock, S. Das, and R. Grunwald, "Programmable ultrashort-pulsed flying images," *Opt. Express*, vol. 17, no. 9, p. 7465, 2009.

[108] J. Arlt, V. Garces-Chavez, W. Sibbett, and K. Dholakia, "Optical micromanipulation using a bessel light beam," *Opt. Commun.*, vol. 197, p. 239, 2001.

[109] F. Fahrbach, P. Simon, and A. Rohrbach, "Microscopy with self-reconstructing beams," *Nature Photonics*, vol. 4, p. 780, 2010.

[110] F. Fahrbach and A. Rohrbach, "A line scanned light-sheet microscope with phase shaped self-reconstructing beams," *Opt. Express*, vol. 18, p. 24229, 2010.

[111] T. A. Planchon, L. Gao, D. Milkie, M. W. Davidson, J. A. Galbraith, C. Galbraith, and E. Betzig, "Rapid three-dimensional isotropic imaging of living cells using bessel beam plane illumination," *Nature Methods*, vol. 8, no. 5, p. 417, 2011.

[112] Z. Ding, H. Ren, Y. Zhao, J. S. Nelson, and Z. Chen, "High-resolution optical coherence tomography over a large depth range with an axicon lens," *Opt. Lett.*, vol. 27, no. 4, p. 243, 2002.

[113] P. Polesana, D. Faccio, P. D. Trapani, A. Dubietis, A. Piskarskas, A. Couairon, and M. A. Porras, "High localization, focal depth and contrast by means of nonlinear bessel beams," *Opt. Express*, vol. 13, no. 16, p. 6160, 2005.

[114] Y. Matzuoka and Y. Kizuka, "The characteristics of laser micro drilling using a bessel beam," *Appl. Phys. A*, vol. 84, p. 423, 2006.

[115] J.Durnin, "Exact solutions for nondiffracting beams. i. the scalar theory," *J. Opt. Soc. Am. A*, vol. 4, p. 651, April 1987.

[116] J. Durnin, J. J.J.Miceli, and J.H.Eberly, "Comparison of bessel and gaussian beams," *Opt. Lett.*, vol. 23, p. 79, Feb. 1988.

[117] Y. Lin, W. Seka, J. Eberly, H. Huang, and D. Brown, "Experimental investigation of bessel beam characteristics," *Appl. Opt.*, vol. 31, no. 15, p. 2708, 1992.

[118] R. M. Herman and T. A. Wiggins, "Production and uses of diffractionless beams," *J. Opt. Soc. Am. A*, vol. 8, no. 6, p. 932, 1991.

[119] F. Gori, G. Guattari, , and C. Padovani, "Besselgauss beams,," *Opt. Comm.*, vol. 64, pp. 491–495, 1987.

[120] J. Arlt and K. Dholakia, "Generation of high-order bessel beams by use of an axicon," *Opt. Commun.*, vol. 177, p. 297, 2000.

[121] J. ARLT, R. KUHN, and K. DHOLAKIA, "Spatial transformation of laguerre-gaussian laser modes," *J. Mod. Opt.*, vol. 48, no. 5, p. 783, 2001.

[122] R. Romea and W. Kimura, "Modeling of inverse cerenkov laser acceleration with axicon laser-beam focusing," *Phys. Rev. D*, vol. 42, no. 5, p. 1807, 1990.

[123] J. Fontana and R. Pantell, "A high-energy, laser accelerator for electrons using the inverse cherenkov effect," *J. Appl. Phys.*, vol. 54, no. 8, p. 4285, 1983.

[124] S. Tidwell, D. Ford, and W. Kimura, "Transporting and focusing radially polarized laser beams," *Opt. Eng.*, vol. 31, no. 7, p. 1527, 1992.

[125] D. Mugnai, "Bessel beams and signal propagation," *Phys. Lett. A*, vol. 278, p. 6, 2000.

[126] T. Sauter and F. Paschke, "Can bessel beams carry superluminal signals ?," *Phys. Lett. A*, vol. 285, p. 1, 2001.

[127] E. C. de Oliveira, W. R. Jr., D. Thober, and A. X. Jr., "Thoughtful comments on bessel beams and signal propagation," *phys. Lett. A*, vol. 284, p. 296, 2001.

[128] K. T. McDonald, "Bessel beams," 2000.

[129] O. Stravroudis, *The Optics of Rays, Wavefronts, and Caustics*. Academics Press, 1972.

[130] R. Grunwald and M. Bock, "Propagation and wavefront ambiguity of linear nondiffracting beams," *Proc. of SPIE*, vol. 8999, pp. 89990G–1, 2014.

[131] J. Y. Lu and J. F. Greenleaf, "Nondiffracting x waves-exact solutions to free-space scalar wave equation and their finite aperture realizations," *IEEE Trans. Ultrasonics, Ferroelectrics, Frequency Control*, vol. 39, no. 1, p. 19, 1992.

[132] J. Gutierrez-Vega, M. Iturbe-Castillo, G. Ramirez, E. Tepichin, R. Rodriguez-Dagnino, S. Chavez-Cerda, and G. New, "Experimental demonstration of optical mathieu beams," *Opt. Commun.*, vol. 195, p. 35, 2001.

[133] M. A. Bandres and J. C. Gutirrez-Vega, "Parabolic nondiffracting optical wave fields," *Opt. Lett.*, vol. 29, no. 1, p. 44, 2004.

[134] I. Chremmos, Z. Chen, D. Christodoulides, and N. Efremidis, "Bessel-like optical beams with arbitrary trajectories," *Opt. Lett.*, vol. 37, no. 23, p. 5003, 2012.

[135] H. Hernandez-Figueroa, E. Recami, and M. Zamboni-Rached, eds., *Non-Diffracting Waves*. Wiley-VCH Verlag GmbH and Co. KGaA, 2014.

[136] D. Li and K. Imasaki, "Proposal of laser-driven acceleration with bessel beam," *Proceedings of the 2004 FEL Conference,*, p. 614, 2004.

[137] X. Zhu and J. M. Kahn, "Free-space optical communication through atmospheric turbulence channels," *IEEE Trans. Commun.*, vol. 50, no. 8, p. 1293, 2002.

[138] J. C. Juarez, A. Dwivedi, A. R. H. Jr., S. D. Jones, V. Weerackody, and R. A. Nichols, "Free-space optical communications for next-generation military networks," *IEEE Commun. Mag.*, vol. 44, p. 46, 2006.

[139] P. Birch, I. Ituen, R. Young, and C. Chatwin, "Long-distance bessel beam propagation through kolmogorov turbulence," *J. Opt. Soc. Am. A*, vol. 32, no. 11, p. 2066, 2015.

[140] J. Fortin, G. Rousseau, N. McCarthy, and M. Piche, "Generation of quasi-bessel beams and femtosecond optical x-waves with conical mirrors," *Proc. SPIE*, vol. 4833, p. 876, 2003.

[141] B. Braverman, K. B. Kuntz, M. Lobino, E. M. Pessina, and A. Lvovsky, "Measurement of superluminal phase and group velocities of bessel beams in free space," 2008.

[142] J. W. M. Baars, *The Paraboloidal eflector Antenna in Radio Astronomy and Communication.* Springer Science+Business Media, LLC, 2007.

[143] D. R. Cheng and S. T. Moseley *IRE Transactions-Antennas and propagation*, p. 214, 1955.

[144] L. Shafai, A. Kishk, and A. Sebak, "Near field focusing of apertures and reflector antennas," *Proc. IEEE Conf. on Communications, Power and Computing WESCANEX97, Winnipeg, MB, May 2223, 1997*, p. 246, 1997.

[145] M. Zamboni-Rached, M. C. de Assis, and L. A. Ambrosio, "Diffraction resistant scalar beams generated by a parabolic reflector and a source of spherical waves," *Appl.Opt.*, vol. 54, p. 5949, 2015.

[146] V. Vaicaitis and S. Paulikas, "Formation of bessel beams with continuously variable cone angle," *Opt Quant Electron*, vol. 35, p. 1065, 2003.

[147] V. Belyi, A. Forbes, N. Kazak, N. Khilo, and P. Ropot, "Bessellike beams with zdependent cone angles," *Opt. Express*, vol. 18, no. 3, p. 1966, 2010.

[148] P.Lematre-Auger, S. Abielmona, and C. Caloz, "Circular antenna array for microwave bessel beam generation," *in Proc. XXXth URSI Gen. Assembly Sci. Symp.*, p. pp. 14., Aug. 2011.

[149] P.Lemaitre-Auger, S.Abielmona, and C.Caloz, "Generation of bessel beams by two-dimensional antenna arrays using sub-sampled distributions," *IEEE TRANSACTIONS ON ANTENNAS AND PROPAGATION*, vol. 61, p. 1838, April 2013.

[150] M.A.Salem, A.H.Kamel, and E. Niver, "Microwave bessel beams generation using guided modes," *IEEE TRANSACTIONS ON ANTENNAS AND PROPAGATION, VOL. 59, NO. 6, JUNE 2011*, vol. 59, p. 2241, June 2011.

[151] Manzhura, Oksana, E. Niver, and M. Salem, "Practical realization of a microwave bessel beam launcher , 2011.," *General Assembly and Scientific Symposium, IEEE*, vol. XXXth URSI., pp. 1–2, 2011.

[152] J.W.Goodman, *Introduction to Fourier Optics.* THE McGRAW-HILL COMPANIES, INC., second ed., 1996.

[153] Z. Jiang, Q. Lu, and Z. Liu, "Propagation of apertured bessel beams," *Appl. Opt.*, vol. 34, no. 31, p. 7183, 1995.